Topological aspects of systems with broken time-reversal symmetry

Srinivas Raghu

A Dissertation

Presented to the Faculty

of Princeton University

in Candidacy for the Degree

of Doctor of Philosophy

Recommended for Acceptance

by the Department of

Physics

September, 2006

Abstract

This thesis deals with two topics involving topological "vortex-like" defects arising due to the breaking of time-reversal symmetry. A recurring theme shall be the interplay between the bulk properties and the physics at the boundaries of such systems.

In the first part of the thesis, we construct direct analogs of quantum Hall effect edge modes in photonic systems with broken time-reversal symmetry. we will show how "photonic crystals" built out of time-reversal breaking Faraday effect media can exhibit "chiral" edge modes in which light propagates unidirectionally along boundaries across which the Faraday axis reverses. The crucial feature underlying this idea is that the photon bands of interest have non-zero Chern numbers (topological integers, which in the case at hand, represent the winding number of the Berry gauge connection of the bands). Using both numerical diagonalization and simple analytical models, we show how to construct photon bands with non-zero Chern invariants, and we use them to realize the precise classical counterpart of the electronic edge modes of the quantum Hall effect. To study these modes numerically, we have designed and implemented novel real-space treatments of the source-free Maxwell normal mode problem on a discrete network.

In the second part of the thesis, we focus on extreme type II superconductors in externally applied magnetic fields. Motivated by experiments of Ong and collaborators on the Nernst effect in the cuprate superconductors, we consider a model of a superconductor which permits fluctuations only in the phase of the order parameter. In the presence of the magnetic field, a net vorticity is induced in the system, and we consider the various static and thermoelectric signatures of these superconducting vortices. Using numerical

simulations, analytical calculations, and arguments from duality, we study thermoelectric transport and boundary diamagnetic currents. We conclude that such simple models of superconductors with fluctuations only of the phase degrees of freedom share qualitative similarities with the experiments of Wang et. al. [69]. Interpretations of these experiments as well as predictions are made here based on these idealized models.

Acknowledgements

It is a pleasure to acknowledge my advisor Duncan Haldane. I consider myself to be incredibly privileged to have worked closely with him during the past five years. From Duncan, I have not just learned a great deal of physics - knowledge that courses, and textbooks simply cannot provide - but more importantly, I have learned how to *do* physics, and to appreciate the serious level of dedication that is required in order to be successful at this enterprise. Despite Duncan's brilliant accomplishments in our field, he has been extremely patient with me and has been a dedicated mentor and advisor. Almost everything written in the pages to follow can be traced back to a conversation that I have had with him. His enthusiasm for doing physics, and his unique perspective on the subject has made graduate school an unparalleled experience.

I am indebted to David Huse for sharing with me his insights on topics relating to the final chapter of this thesis. Also, his close reading of this thesis has greatly enhanced its clarity.

I should thank Shivaji Sondhi for providing me with crucial guidance and honest feedback especially during the early part of my graduate studies.

I must thank Phuan Ong for his support through the PCCM program, and for his encouragement and interest in the work leading to the final chapter of this thesis. This chapter has been motivated entirely by the wonderful experiments done in Ong's group over the past few years.

I thank my younger mentors - Ashvin Vishwanath, Gil Refael, Daniel Podolsky, and Emil Prodan - for enlightening discussions, and for interesting collaborations.

I also thank Phil Anderson for expressing interest in my work, for inspiring discussions, and for his helpful comments on the thesis. It has been an honor.

I am indebted to the Kavli Institute for Theoretical Physics, U.C. Santa Barbara, for providing support for a semester, and for organizing extremely stimulating workshops on "Exotic order and criticality in quantum matter", and on "Quantum gases". It was here that much of the work described in this thesis was developed.

I thank some of my graduate student friends, who have contributed to my social and academic life at Princeton. I mention some of them here: Sasha Baytin, Shoibal Chakravarty, Chang Chan, Aleksey Chuvikov, Pedro Goldbaum, Karol Gregor, Shree Khare, Mike Leung, Alexey Makarov, Abhra Mitra, Subroto Mukerjee, Kumar Raman, and Emil Yuzbashian.

I thank my sister Madhavi for her guidance, and for her encouragement, at a time when completing graduate studies seemed to be an unlikely, if not impossible task. I also thank Sekhar for his advice, involvement, and support.

I thank Hema, simply for her friendship, support, and inspiration.

The contributions made by my parents cannot adequately be captured in words. By making difficult and significant sacrifices, they have provided my sister and me with fantastic opportunities in this country. Their guidance comes largely from the example they have set in their own lives. It is to them that I wish to dedicate this thesis.

Contents

Chapter 1

Introduction

1.1 Some general remarks

In this chapter, we mention the essential physical ideas explored in this thesis without getting into the formal details.

This thesis considers two seemingly disparate topics in condensed matter physics. The first topic deals with Bloch states of photons (arising from the periodicity of the underlying media), whereas the second deals with vortices in strongly type II superconductors in the extreme anisotropic (quasi-two-dimensional) limit. No two topics could be more different.

However, a feature common to both topics is that time-reversal symmetry will be broken in both cases. The most common way to break time reversal symmetry in an experiment is to apply a magnetic field. However, time-reversal symmetry can also be broken intrinsically, as in a ferromagnet, or as in an unconventional superconductor with a "p+ip" pairing amplitude.

In the first topic of this thesis, we will be considering magneto-optic materials, that usually display time -reversal breaking intrinsically (although the statements we make there are not dependent on whether time-reversal is broken intrinsically or via an applied magnetic field). In the second topic of this thesis, we will consider some properties of a type II superconductor in applied magnetic fields.

What kinds of interesting physics can we expect in systems such as those briefly described above, when time-reversal symmetry is broken? We know from elementary quantum mechanics that the time-reversal operator is anti-unitary, which means that we can always express it as a product of a (basis-dependent) unitary operator and the complex conjugation operator. Thus, when time-reversal symmetry is broken, the wave function is generically a complex function with both an amplitude and a spatially-varying phase, and could permit non-analytic, "vortex-like" defects.

To see how this could come about, (we neglect internal spin degrees of freedom here and consider only complex scalar wavefunctions), we will need to know the phase differences of this complex function between two nearby points. Single-valuedness of this complex function will place constraints on the winding number of this phase field.

In the case of Bloch states in the Brillouin zone, we will look at phase differences of the wave functions between two nearby points in $\boldsymbol{k}$-space; this way, we are naturally led to the notion of a Berry connection and curvature - which we discuss in the next chapter. In the 2D superconductor, we shall study the gauge-invariant phase differences of the superconducting order parameter at two nearby points, which is proportional to the local value of the supercurrent in the system (local phase differences of Bloch states in the Brillouin zone carry no analogous physical meaning). For the photon bands, we will be interested in the winding number of the Berry phase around the Brillouin zone boundary. Single-valuedness of the wave functions constrains the winding number to be an integer. If this integer is non-zero, there must be a gauge singularity of the wave function somewhere in the Brillouin zone.

Let us contrast this with the case of a two dimensional superconductor. If the phase of the superconducting order parameter winds by an integer multiple of 2π (again single-valuedness of the order parameter in this simple case places the integer constraint) around a closed contour in real-space, then it follows that the contour encloses a singularity of the order parameter.

In both cases, these singularities are topological, and behave as point charges (which are

topological defects of the electric field) in two dimensions (vortices). In the case of Bloch bands, these topological gauge singularities in $\boldsymbol{k}$-space have well-known consequences in the quantum Hall effect of electronic systems [59].

It is important to stress here that unlike vortices in superconductors, the topological singularities associated with the Berry gauge connection are not physical quantities, in the sense that their positions depend on the choice of gauge: a local gauge transformation will move the locations of these singularities in $\boldsymbol{k}$-space. Thus, we want to make it clear that the analogy between vortices (topological defects of the phase of the superconducting wave function) and the gauge singularities of Bloch bands is not a perfect one. There is nothing physical to be associated with the point-like "core" of a gauge singularity.

The goal of the first part of the thesis is to see how much of the well-known physics of the quantum Hall effect can be transcribed to photonic systems, where the degrees of freedom are neutral bosons. Here, the vortex-like defects in the Brillouin zone are static objects; our goal is to see how they affect the real-space dynamics of the system.

The goal of the second part of this thesis will be to study the problem of thermoelectric transport and diamagnetism in the context of simple vortex models in two dimensions. Here, however, we will primarily be interested in the dynamics of vortices themselves. Although the vortices exist even in the absence of a magnetic field, the net vorticity vanishes identically in this case. The quantities of interest in this thesis, transverse thermoelectric transport and diamagnetism, vanish in this situation.

1.2 Overview of the thesis

In chapter 2, we discuss Berry phases, Berry curvature, and Chern invariants, and point out various connections between these objects and the quantum Hall effect. We also discuss a model of a quantum Hall effect that does not require a net magnetic flux density, but rather only time-reversal breaking. We explicitly construct this model, discuss its topological structure, and point out the way the model's parameters can be tuned to realize the "Chiral" edge modes of the quantum Hall effect. These ideas will be the cornerstone of the essential

material of chapter 3.

In chapter 3, we consider analogs of quantum Hall effect edge modes in photonic systems. Formal aspects of our formulation of the problem are presented in full detail, and are supplemented with technical details, including especially the consideration of Berry curvature in the case of frequency dependence of the constitutive relations of the system. We next consider explicit models of systems with the interesting topological properties briefly described here. We construct explicit realizations of unidirectional edge modes of light in this system. These modes are the precise equivalents of the quantum Hall effect edge modes in electronic systems. We present both numerical computations and analytical calculations using simple models to confirm the concept.

In chapter 4, we discuss the numerical algorithms we have designed and implemented to compute the photon band spectra. Our approach is different than the standard approach, and has greater scope of applicability.

In chapter 5, we switch gears to the second topic of this thesis. We proceed along two channels in this chapter. First, we consider a model of superconducting phase fluctuations only (XY model) in an external field. We use TDGL ("model A") dynamics and compute α_{xy}, the transverse thermoelectric coefficient as well as the magnetization at various temperatures and fields. This numerical work is supplemented by analytical high temperature expansions for these quantities. Next, we consider the dual coulomb-gas model in which the vortices (not the phases) are the primary degrees of freedom. Using Monte Carlo simulations, we study the diamagnetism in this model and discuss work currently in progress towards computing α_{xy}. An appendix shows explicitly the relationship between the 2D XY model in a magnetic field and a 2D Coulomb gas with a static background charge density.

Chapter 2

Berry Curvature, Chern invariants, and a "zero-field" quantized Hall effect in graphene

2.1 Introduction

This chapter is a review of the basic ideas of Berry curvature, Chern numbers, and quantum Hall effect edge modes which will further be explored in subsequent chapters of this thesis. Those readers already familiar with these concepts may skip ahead to the next chapter.

Recently, there has been a growing interest in the broad class of phenomena whose dynamics are heavily influenced by the underlying topology of the Hilbert space of states under consideration. Examples include the spin Hall effect in systems with spin-orbit coupling, the anomalous Hall effect in Ferromagnetic insulators, and quantum Hall systems. In all of the systems mentioned above, the idea of the geometric phase plays a crucial role in determining the physics. When first introduced, the geometric phase was described within the context of adiabatic evoution in quantum mechanical systems. Soon afterwards, however, Simon [53] recast the geometric phase in the more abstract, and general, language of holonomy while simultaneously showing how it arose quite naturally in the context of the

quantum Hall effect.

In this chapter, we quickly review the ideas of the geometric phase and some of their physical consequences which will be explored in later chapters of this thesis.

2.2 Abelian Berry phases and the Chern invariant

A discussion of the Berry phase is usually initiated by considering a Hermitian eigensystem which depends parametrically on a vector $g^\mu, \mu = 1, \cdots, N$:

$$H(\boldsymbol{g})|u_n(\boldsymbol{g})\rangle = E_n(\boldsymbol{g})|u_n(\boldsymbol{g})\rangle \tag{2.1}$$

We assume that $\boldsymbol{g}$ acts as an ordinary vector without any underlying quantum dynamics (a canonical example is the problem of Jahn-Teller distortions in molecular physics, in which $\boldsymbol{g}$ is the set of nuclear coordinates, which are treated within a Born-Oppenheimer approximation, are the classical parameters of the Hamiltonian, the electronic orbitals are solved in the space of all nuclear separations, and the quantum dynamics of the nuclear are altogether neglected). For all values of the parameter $\boldsymbol{g}$ the states $|u_m(\boldsymbol{g})\rangle$ span the same Hilbert space. We solve the eigenvalue problem above for each value of $\boldsymbol{g}$, and assume that the states are ordered in some systematic fashion at each point in the parameter space.

Focus for the moment on a state $|u_n(\boldsymbol{g})\rangle$ which remains non-degenerate for all values of $\boldsymbol{g}$. The states of the eigenvalue problem are only defined upto an arbitrary $\boldsymbol{g}$-dependent unimodular phase factor: a local phase variation

$$|u_n(\boldsymbol{g})\rangle \to e^{i\chi(\boldsymbol{g})}|u_n(\boldsymbol{g})\rangle \tag{2.2}$$

does not affect physical variables such as the spectrum, density matrix, and the matrix elements of all Hermitian operators in the Hilbert space. The phase ambiguity above is quite similar to the $U(1)$ gauge invariance of ordinary electrodynamics.

Since the Hilbert space remains fixed for all $\boldsymbol{g}$, it is natural to compare the states $|u_n(\boldsymbol{g})\rangle$ for different values of the parameter $\boldsymbol{g}$. The overlap of two states can generically be written as a complex number with an amplitude and a phase:

$$\langle u_n(\boldsymbol{g}_1)|u_n(\boldsymbol{g}_2)\rangle = |\langle u_n(\boldsymbol{g}_1)|u_n(\boldsymbol{g}_2)\rangle|e^{iA_n(12)} \tag{2.3}$$

where $A_n(12)$ is a quantity that depends on the spectral index n, as well as the (gauge-dependent) values of the parameters $\boldsymbol{g}_1$ and $\boldsymbol{g}_2$. The overlap provides us with a notion of parallel transport on the $\boldsymbol{g}$ - manifold, i.e. a means to compare states living on two nearby points in parameter space.

This becomes clearer when we consider a series of overlaps along path in parameter space

$$\prod_{m=1}^{M-1} \langle u_n(\boldsymbol{g}_m)|u_n(\boldsymbol{g}_{m+1})\rangle = \mathcal{Z}_n \exp\left(i \sum_{m=1}^{M-1} A(m, m+1)\right), \tag{2.4}$$

where

$$\mathcal{Z}_n = \prod_{m=1}^{M-1} |\langle u_n(\boldsymbol{g}_m)|u_n(\boldsymbol{g}_{m+1})\rangle|. \tag{2.5}$$

The total phase picked up along this path depends on the choice of gauge used to define each of the states. Notice that in the expression above, local gauge transformations will cancel pairwise for all states along the path except for the initial and final points along the trajectory. However, the overlap for the entire path is path-dependent - the value of $\mathcal{Z}_n$ clearly depends on the choice of path. At a glance, it therefore appears that such a phase factor cannot possibly have any observable physical consequences, since observables must always be described by gauge-invariant objects. New physics is unearthed, however, when one considers *closed* contours in the space of parameters. In this case, if the states are normalized for each value of $\boldsymbol{g}$, then $\mathcal{Z}_n = 1$, and the final state must be equivalent to the initial state upto an overall gauge-invariant phase factor.

To determine a closed-form expression for this phase difference, we take the continuum limit of the above expressions. Starting from the overlap of two infinitessimally close states in parameter space,

$$\frac{\langle u_n(\boldsymbol{g})|u_n(\boldsymbol{g}+\delta\boldsymbol{g})\rangle}{|\langle u_n(\boldsymbol{g})|u_n(\boldsymbol{g}+\delta\boldsymbol{g})\rangle|} \equiv \exp\left(i\mathcal{A}_n(\boldsymbol{g})\cdot\delta\boldsymbol{g}\right), \tag{2.6}$$

we can work out an expression for $\mathcal{A}_n$ by expanding both sides of the equation above to leading order in $\delta\boldsymbol{g}$. The result is

$$\mathcal{A}_n^a(\boldsymbol{g}) = \frac{\langle u_n(\boldsymbol{g})|\nabla_g^a u_n(\boldsymbol{g})\rangle - \langle \nabla^a u_n(\boldsymbol{g})|u_n(\boldsymbol{g})\rangle}{2i\langle u_n(\boldsymbol{g})|u_n(\boldsymbol{g})\rangle}. \tag{2.7}$$

When the states are normalized to unity, the expression above reduces to the familiar form $\mathcal{A}_n^a(\boldsymbol{g}) = -i\langle u_n(\boldsymbol{g})|\nabla_g^a u_n(\boldsymbol{g})\rangle$ The vector field $\mathcal{A}^a(\boldsymbol{g})$ defined by taking the continuum limit above is known as the *Berry Connection*.

The *Berry phase* picked up by a state $|u_n\rangle$ upon travelling on a closed path in $\boldsymbol{g}$ - space is defined (modulo 2π) as

$$\exp\left(i\gamma_n(C)\right) = \exp\left(i \oint_C dg_a \cdot \mathcal{A}^a(\boldsymbol{g})\right) \tag{2.8}$$

When a local gauge transformation, Eq. (2.2), is applied to the state, the Berry connection transforms as

$$\mathcal{A}_n^a(\boldsymbol{g}) \to \mathcal{A}_n^a(\boldsymbol{g}) + \nabla_g^a \chi_n(\boldsymbol{g}), \tag{2.9}$$

in analogy with the $U(1)$ vector potential of electrodynamics. Extending this analogy further, the *curl* of the Berry Connection must be the gauge-invariant analog of the magnetic flux density, and can be written as a second-rank anti-symmetric tensor:

$$\mathcal{F}_n^{ab}(\boldsymbol{g}) = \nabla_g^a \mathcal{A}^b(\boldsymbol{g}) - \nabla_g^b \mathcal{A}^a(\boldsymbol{g}). \tag{2.10}$$

This quantity is known as the *Berry Curvature*. It is easily seen then, that the Berry phase picked up by a wave-function along some closed trajectory in parameter space can be expressed as surface integral of the Berry curvature via Stokes' theorem:

$$\exp\left(i\gamma_n(C)\right) = \exp\left(i \iint_{S_C} dg_a \wedge dg_b \mathcal{F}^{ab}(\boldsymbol{g})\right) \tag{2.11}$$

We interpret Eq. (2.11) as a generalized Aharanov-Bohm effect [1] in which the Berry phase of a wave function is given in terms of the "Berry flux" enclosed by the contour C in parameter space.

2.2.1 Broken time-reversal symmetry and the Chern invariants

Let us now restrict ourselves to the case in which the parameter space is two-dimensional. An example, and one which will be the focus of subsequent chapters of this thesis, is the set of two-dimensional Bloch states of single particle Hamiltonians:

$$|\psi_n(\boldsymbol{k}, \boldsymbol{r})\rangle = \exp\left(i\boldsymbol{k} \cdot \boldsymbol{r}\right) |u_n(\boldsymbol{k}, \boldsymbol{r})\rangle \tag{2.12}$$

In this case, $\boldsymbol{g}$ is represented by the two components of the Bloch vector in the 2D Brillouin zone, and the Hilbert space consists of the periodic parts of the Bloch wave functions. We work in a fixed Hilbert space by considering only $|u_n\rangle$, the periodic parts of the Bloch states, which are the solutions of the following:

$$H(\boldsymbol{k})|u_n(\boldsymbol{kr})\rangle = E_n(\boldsymbol{k})|u_n(\boldsymbol{kr})\rangle \tag{2.13}$$

where $H(\boldsymbol{k}) = \exp(-i\boldsymbol{k}\cdot\boldsymbol{r})\, H \exp(i\boldsymbol{k}\cdot\boldsymbol{r})$. The Berry connection and curvature are readily transcribed for this problem from the more general derivation above. One finds that the Berry connection for the set of normalized states is simply $\mathcal{A}_n^a = -i\langle u_n(\boldsymbol{k},\boldsymbol{r})|\nabla_k^a u_n(\boldsymbol{k},\boldsymbol{r})\rangle$, and the Berry curvature, a pseudoscalar in two dimensions, is found by taking the curl of the connection, to be

$$\mathcal{F}^{xy} = -i\langle\nabla_k^x u_n(\boldsymbol{k},\boldsymbol{r})|\nabla_k^y u_n(\boldsymbol{k},\boldsymbol{r})\rangle - c.c \tag{2.14}$$

The integral of the Berry curvature over the entire 2D Brillouin zone has a special significance. By Stokes' theorem, it is also given by the quantity $\exp(i\oint_C \mathcal{A}^a(\boldsymbol{k})dk_a)$, where the contour C is taken to be the boundary of the Brillouin zone. Although the definition of the Brillouin zone is to a certain extent arbitrary, the phase factor is unambiguous: it represents the Berry phase picked up by the Bloch wave function upon traversing the contour, and is the $\boldsymbol{k}$-space analog of the Bohm-Aharonov phase. Single-valuedness of the requires this phase to be an integral multiple of 2π. Thus, we arrive at the result that the integral of the Berry curvature satisfies

$$\iint_{BZ} \mathcal{F}^{xy}(\boldsymbol{k},\boldsymbol{r})dk_x dk_y = 2\pi\mathcal{C}_n^{(1)}, \tag{2.15}$$

where $\mathcal{C}_n^{(1)}$ is an integer known as the Chern number, or the member of the first Chern class [43].

The Chern number is a topological index generally defined as the integral of the Berry curvature over a closed 2D manifold. In this case, it simply represents the winding number of the Berry phase of a state picked up around the Brillouin zone. Alternatively, it is a count of the number of "Berry flux quanta" threading the plane of the 2D Brillouin zone.

Chern numbers have well-known consequences in the quantum Hall effect. The zero temperature Kubo formula for the Hall conductance

$$\sigma^{xy} = \frac{1}{L^2} \int dt \langle [J^x(t), J^y(0)] \rangle \tag{2.16}$$

turns out to be related to the Chern invariant as follows: in the integer quantum Hall effect, when the Fermi level lies in a gap, the total Hall conductance of the system is given by

$$\sigma_{xy} = \frac{e^2}{h} \sum_{i \in occ} \mathcal{C}_i^{(1)}, \tag{2.17}$$

where the sum is carried over all occupied bands.

More generally, the Chern number is a well-defined property of many-body ground state wave functions of systems with a gap to excitations. One considers the ground state wavefunction $|\Psi(\boldsymbol{r}; \boldsymbol{\phi})\rangle$ on a torus (size $L_x \times L_y$) with twisted boundary conditions [45]:

$$|\Psi(\boldsymbol{r} + L_x \hat{x}; \boldsymbol{\phi})\rangle = \exp(i\phi_x) |\Psi(\boldsymbol{r}; \boldsymbol{\phi})\rangle. \tag{2.18}$$

In this case, the Berry connection can be defined simply as

$$A^j = -i \langle \Psi(\boldsymbol{r}, \boldsymbol{\phi}) | \frac{\partial}{\partial \phi_j} | \Psi(\boldsymbol{r}, \boldsymbol{\phi}) \rangle \tag{2.19}$$

The application of this formalism to Bloch states represents the special case in which the twisted boundary conditions are implemented via the Bloch vector.

2.3 Zero field quantum Hall effect in graphene

To clarify some of these ideas, we present a simple model of Bloch states with broken time-reversal symmetry having bands with non-zero Chern invariants and gapless edge modes. The model considered here is that of two dimensional graphite ("graphene") a system that has received considerable attention recently mostly due to its robust quantum Hall effect. The model described below is relevant to this thesis since it represents a method of obtaining quantum Hall effects on systems using Bloch states only, and can therefore be transcribed to non-electronic systems (we will do this in the next chapter).

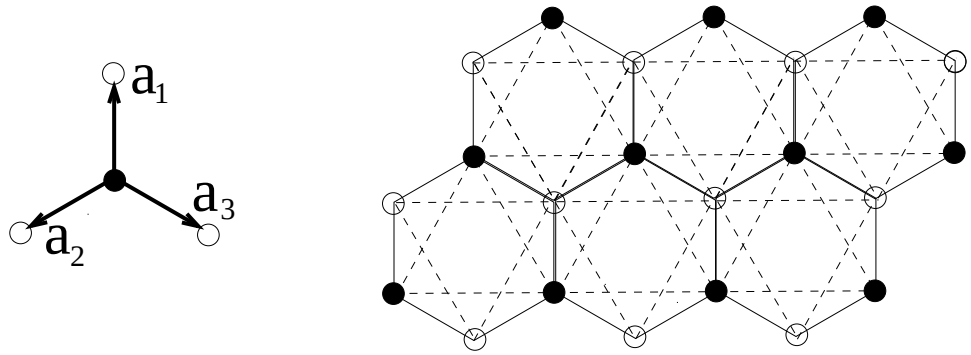

Figure 2.1: Tight binding electrons on a honeycomb network with broken time-reversal symmetry. Open and dark circles mark the A and B sublattices respectively. First neighbor hoppings connect sites with those belonging to the opposite sublattice, and $\boldsymbol{a}_1, \boldsymbol{a}_2, \boldsymbol{a}_3$ represent displacements from a B site to each of its nearest neighbors on an A site. Second neighbor hopping occurs along the dotted lines. There is zero net magnetic flux through each elementary plaquette (drawn with solid lines), but each closed path of second neighbor hoppings encloses non-zero magnetic flux.

The system consits of spinless fermions at half-filling on a honeycomb lattice with the following Hamiltonian:

$$\mathcal{H} = -t_1 \sum_{\langle ij \rangle} \left(c_i^\dagger c_j + h.c \right) - t_2 \sum_{\langle\langle ij \rangle\rangle} \left(c_i^\dagger e^{i\phi_{ij}} c_j + h.c \right) + \sum_{\sigma=a,b} U_\sigma c_\sigma^\dagger c_\sigma \tag{2.20}$$

The first term represents nearest neighbor hopping of electrons from the A sites to the B sites and *vice versa*, the second term describes second neighbor hoppings that connect sites on the same sublattice, and the third term is an inversion symmetry breaking perturbation representing a relative difference of onsite energies on each of the two sublattice orbitals. This is achieved, for example, by replacing the Carbon atoms of graphene by two species of atoms, as in the case of Boron-Nitride, which is often used to form Carbon nanotube structures. Time-reversal symmetry is broken in this model when the second neighbor hoppings are minimally-coupled to a staggered magnetic flux pattern that produces a *zero net flux per unit cell*.

Start with the clean graphene system without broken inversion or time-reversal symmetry. Work in the two-component basis of Bloch states associated with each of the sublattices (we assume a single orbital per site). In this representation, the Hamiltonian is given by

$$\mathcal{H} = \sum_k h_1(\boldsymbol{k}) \tag{2.21}$$

$$h_1(\boldsymbol{k}) = \begin{pmatrix} 0 & -t_1 \sum_{i=1}^{3} \exp\left(i\boldsymbol{k}\cdot\boldsymbol{a}_i\right) \\ -t_1 \sum_{i=1}^{3} \exp\left(-i\boldsymbol{k}\cdot\boldsymbol{a}_i\right) & 0 \end{pmatrix} \tag{2.22}$$

At half-filling, the system is a semimetal; the bandstructure contains gapless points at each corner of the hexagonal Brillouin zone. By varying the two components of the Bloch vector in the Brillouin zone (the two parameters in the context of the previous section), we obtain degeneracies when

$$\sum_{i=1}^{3} \exp\left(i\boldsymbol{k}_0\cdot\boldsymbol{a}_i\right) = 0 \tag{2.23}$$

The energy dispersion in the vicinity of the zone corners (the Fermi points at half filling) is linear, and the low energy effective Hamiltonian is given by a massless two dimensional Dirac equation obtained by expanding the Hamiltonian in Eq. (3.8) to leading order at the Fermi points:

$$\mathcal{H} = v \sum_{\alpha} \left(\delta k_1^{\alpha} \boldsymbol{\sigma}^2 - \delta k_2^{\alpha} \boldsymbol{\sigma}^1\right), \tag{2.24}$$

where $v = 3t_1|\boldsymbol{a}_i|/2\hbar$, and $\delta\boldsymbol{k}^{\alpha} = \boldsymbol{k} - \boldsymbol{k}_0^{\alpha}$ and ($\alpha = \pm 1$), marks the location of the two distinct zone corners (the other four are related to these by reciprocal lattice translations). For this reason, the zone corners, where the two bands touch, are known as *Dirac points*.

Next, we consider the effect of time-reversal and inversion symmetry breaking perturbations. The sublattice orbital energies U_σ are generically of the form $U_\sigma = \bar{m}v^2 + \sigma m_I v^2$ ($\sigma = \pm 1$), where $\bar{m}$ and m_I are arbitrary real constants. We ignore the overall constant term and inversion symmetry breaking term is readily diagonalized in the basis above as

$$h_2(\boldsymbol{k}) = m_I v^2 \boldsymbol{\sigma}^3. \tag{2.25}$$

When time-reversal symmetry is broken, the system obtains a chirality; the real-space phase pattern (see Fig. 2.3) is such that closed trajectories of second neighbor hoppings (dotted triangles in Fig. 2.3) on the "A" sublattice pick up equal and opposite Bohm-Aharonov phases to those on the "B" sublattice. Defining the displacement vectors $\boldsymbol{b}_1, \boldsymbol{b}_2, \boldsymbol{b}_3$,

$\boldsymbol{b}_1 = \boldsymbol{a}_2 - \boldsymbol{a}_3$, etc, along the next neighbor bonds, the time-reversal breaking term is written in the above basis as

$$h_3(\boldsymbol{k}) = \begin{pmatrix} -2t_2 \sum_i \exp\left(i\boldsymbol{k}\cdot\boldsymbol{b}_i + i\phi\right) + h.c. & 0 \\ 0 & -2t_2 \sum_i \exp\left(i\boldsymbol{k}\cdot\boldsymbol{b}_i - i\phi\right) + h.c \end{pmatrix}, \quad (2.26)$$

where

$$\phi = 2\pi \left(2\Phi_\alpha + \Phi_\beta\right)/\Phi_0, \quad (2.27)$$

Φ_α and Φ_β are the magnetic fluxes through the regions marked α and β, respectively in Fig. **??**, and Φ_0 is the flux quantum.

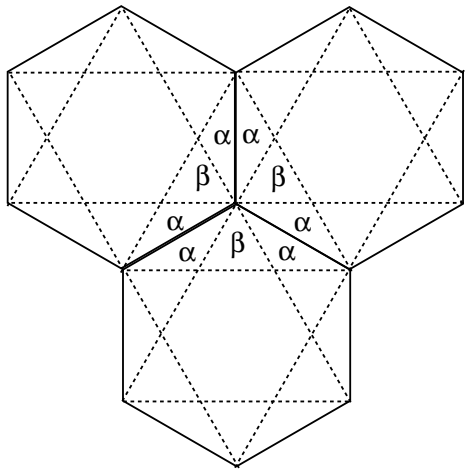

Figure 2.2: Staggered flux pattern used to break time-reversal symmetry in Haldane's model.

By making use of some simple trigonometric identities, the three terms considered separately above are written compactly as follows:

$$H(\boldsymbol{k}) = h_1(\boldsymbol{k}) + h_2(\boldsymbol{k}) + h_3(\boldsymbol{k}) \quad (2.28)$$

$$h_1(\boldsymbol{k}) = t_1 \left(\sum_i \cos\left(\boldsymbol{k}\cdot\boldsymbol{a}_i\right) \boldsymbol{\sigma}^1 + \sin\left(\boldsymbol{k}\cdot\boldsymbol{a}_i\right) \boldsymbol{\sigma}^2 \right) \quad (2.29)$$

$$h_2(\boldsymbol{k}) = m_I v^2 \boldsymbol{\sigma}^3 \quad (2.30)$$

$$h_3(\boldsymbol{k}) = 2t_2 \cos\phi \left(\sum_i \cos\left(\boldsymbol{k}\cdot\boldsymbol{b}_i\right) \right) \mathbf{1} - 2t_2 \sin\phi \left(\sum_i \sin\left(\boldsymbol{k}\cdot\boldsymbol{b}_i\right) \right) \boldsymbol{\sigma}^3 \tag{2.31}$$

The low energy effective Hamiltonian of this model obtained by expanding to lowest order about the two distinct zone corners is

$$\mathcal{H} = v \sum_\alpha [\left(\delta k_1^\alpha \boldsymbol{\sigma}^2 - \delta k_2^\alpha \boldsymbol{\sigma}^1 \right) + \left(m_I - m_T^\alpha\right) v^2 \boldsymbol{\sigma}^3], \tag{2.32}$$

where $m_T^\alpha = 3\sqrt{3}t_2\alpha\sin\phi$ ($\alpha = \pm 1$) is the second neighbor hopping term to lowest order near the Dirac points. Thus, the inversion and time-reversal symmetry breaking perturbations to the clean graphene system generate "mass terms" in the low energy effective Dirac Hamiltonian. At the lowest energies, there is negligible mixing between the two distinct zone corners, and the Hamiltonian is the sum of two Dirac equations, one for each distinct zone corner.

The zero temperature phase diagram of this system in the m_I, m_T plane is shown in Fig. 2.3. When $m_I = m_T = 0$, we recover the massless Dirac Hamiltonian $h_1(\boldsymbol{k})$, and the bandstructure is the "massless" spectrum $E_\pm^\alpha = \pm v|\delta\boldsymbol{k}^\alpha|$. Switching on either of the mass terms opens up a gap at the zone corners, and the energy dispersion is the solution of the massive 2D Dirac equation:

$$E_\pm^\alpha = \pm \left(v^2 |\delta\boldsymbol{k}^\alpha|^2 + \left(m_I - m_T^\alpha\right)^2 v^4 \right)^{1/2} \tag{2.33}$$

The now non-degenerate bands ($\pm$) have well defined Berry curvature fields in $\boldsymbol{k}$-space:

$$\mathcal{F}_{\alpha\pm}^{xy} = \pm \frac{v\left(m_T + \alpha m_I\right)}{\left(|\delta\boldsymbol{k}^\alpha|^2 + \left(\alpha m_I + m_T\right)^2 v^2 \right)^{3/2}}, \tag{2.34}$$

where $m_T = \alpha m_T^\alpha = 3\sqrt{3}t_2\sin\phi$. When $m_I = m_T = 0$, the Berry curvature is ill-defined due to the degeneracy at the Dirac points, and the Berry curvature equation above assumes the form of a Dirac monopole magnetic flux in $\boldsymbol{k}$-space. When inversion symmetry is broken while time-reversal symmetry is preserved ($m_T = 0$), the Berry curvature field is an odd function is the Brillouin zone:

$$\mathcal{F}_\pm^{xy}(-\boldsymbol{k}) = -\mathcal{F}_\pm^{xy}(\boldsymbol{k}), \tag{2.35}$$

and the integral of the Berry curvature for each band over the entire 2D Brillouin zone vanishes identically - i.e. their Chern invariants are zero.

Next, consider the case when time-reversal symmetry is broken while inversion symmetry is preserved. The Berry curvature field in Eq. (2.34) is now an *even* function in $\boldsymbol{k}$-space; as in the case above, its magnitude rapidly decays away from the zone corners. The contribution from each of the distinct Dirac points to the integrated Berry curvature is $\pi sgn(m_T)$ and each Band has a non-zero Chern number

$$\mathcal{C}_{\pm}^{(1)} = \pm sgn(m_T). \tag{2.36}$$

When both inversion and time-reversal symmetries are broken, the relative strengths of the two mass terms determines whether the two bands have non-zero Chern invariants. There are also special critical lines along which $m_I = \pm m_T$, where the gap at only one of the two distinct zone corners vanishes. Thus, the critical lines separating the quantum Hall regime from the ordinary semiconducting regime are lines along which the system becomes a semi-metal again.

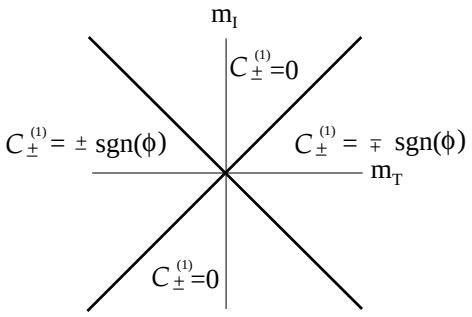

Figure 2.3: Zero temperature phase diagram in the $m_I - m_T$ plane. Graphene without any broken symmetries is found at the origin of the plane, where it retains its massless Dirac spectrum and its semimetallic state. Breaking inversion symmetry alone opens up a gap at the zone corners and produces a conventional semiconductor. Breaking time-reversal symmetry alone (without any net magnetic flux) produces a "zero-field" integer quantum Hall system. The solid lines represent critical lines, separating the quantum Hall system from the semiconductor, and along these lines, the gap vanishes at one of the two distinct zone corners.

While all this can be seen trivially using the expression for the Berry curvature (Eq. 2.34) of the low energy effective Hamiltonian linearized about the zone corners, this result

also holds true for the full Hamiltonian in Eq, (2.28). If time-reversal symmetry is present, the periodic part of the Bloch states at $\boldsymbol{k}$ and $-\boldsymbol{k}$ are related by complex conjugation

$$u_n(-\boldsymbol{k}, \boldsymbol{r}) = u_n^*(\boldsymbol{k}, \boldsymbol{r}), \tag{2.37}$$

whereas if inversion symmetry is present,

$$u_n(-\boldsymbol{k}, \boldsymbol{r}) = u_n(\boldsymbol{k}, \boldsymbol{r}). \tag{2.38}$$

It follows then from the definition of the Berry curvature of Bloch band systems, that for any periodic Hamiltonian, if time-reversal symmetry is present, $\mathcal{F}_n^{ab}(-\boldsymbol{k}) = -\mathcal{F}_n^{ab}(\boldsymbol{k})$, whereas if inversion symmetry is present, $\mathcal{F}_n^{ab}(-\boldsymbol{k}) = \mathcal{F}_n^{ab}(\boldsymbol{k})$, and if both symmetries are present, the Berry curvature vanishes identically.

Having looked at this system in some detail, we can now demonstrate the presence of chiral edge modes along domain walls across which the Chern character of the Bloch bands change.

2.4 Edge modes along domain walls of graphene

In Ref. [19], it was shown that the model above has chiral edge states. By looking at the effect of a *uniform* magnetic flux density in the model described above, one works out the Landau levels (they are relativistic levels due to the Dirac points) in the system. Edge modes can then be shown from the spectral flow of states when the magnetic field changes sign, and from the Streda formula [55], which relates the Hall conductance to the thermodynamic derivative of the electron density with respect to applied field, at fixed Chemical potential. From this relation, one sees [19] that the system accomodates edge states when the Fermi level lies in the gap opened at the zone corners by breaking time-reversal symmetry.

We shall take a slightly different route here - one which will be employed in the next chapter when we consider the photonic analog. Instead of using a uniform applied field, we will tune the system's own parameters such that the Chern number of the two bands of interest change when we we cross a critical point in parameter space.

We only need to look at the low energy Dirac Hamiltonian for the demonstration. For simplicity, we set the inversion symmmetry breaking Dirac mass term m_I to zero, and imagine slowly tuning the time-reversal breaking mass term m_T as a function of position.

Since each Dirac point contributes an equal amount of Berry flux (namely π), to the integrated Berry curvature, we neglect cross-talk between each zone corner (we do this by varying $m_T(\boldsymbol{r})$ on a scale much larger than a lattice constant), and treat each one in isolation. With the position-dependence of the mass gap, we must replace the momenta by $\delta k_a \to -i\hbar\nabla_a$.

The Hamiltonian we consider here is then

$$\mathcal{H} = -i\hbar v \left(\partial_1 \boldsymbol{\sigma}^2 - \partial_2 \boldsymbol{\sigma}^1\right) - m_T(\boldsymbol{r}) v^2 \boldsymbol{\sigma}^3 \tag{2.39}$$

Since the Chern number is a topological "charge" that cannot vary continuously with m_T (in fact, it only depends on its sign), a smooth spatial variation in the Dirac mass term will not change the Chern number of the bands.

However, we tune m_T across it's critical value $m_T = 0$ and see what happens. When the mass term changes sign in some region, the local Bandstructure will be governed again by the *massless* Dirac equation. The bands which had non-zero Chern invariants, will touch one another, and their Chern numbers are no longer well defined.

We can consider a simple case which will have all the features of interest; vary m_T along a single direction (say x), letting it vanish at $x = 0$, having opposite sign on either side (Fig. 2.4).

We shall show that there are edge states here by solving for the zero-energy modes of the Dirac equation:

$$\left[-i\hbar v \left(\partial_x \boldsymbol{\sigma}^y - \partial_y \boldsymbol{\sigma}^x\right) - m_T(x) v^2 \boldsymbol{\sigma}^3\right] \psi = 0 \tag{2.40}$$

We look for spinor solutions in the basis in which σ^x is diagonal. Since the y-direction retains translation invariance, we look for solutions of the form

$$\psi_\alpha(\boldsymbol{r}) = f_\alpha(\boldsymbol{x}) \exp\left(i\alpha \delta k_y y\right), \tag{2.41}$$

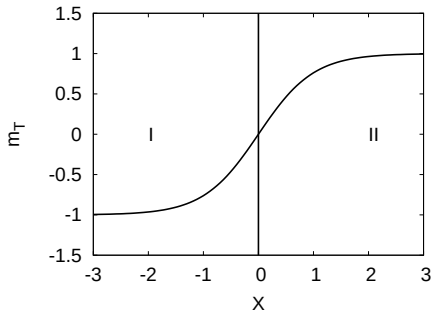

Figure 2.4: A domain wall in 1D

where $\sigma^x f_\alpha = \alpha f_\alpha$, $\alpha = \pm 1$. The spinor f_α obeys a first-order differential equation:

$$i\hbar v\sigma^y f_\alpha(x) = m(x)v\sigma^z f_\alpha(x) \tag{2.42}$$

We multiply through by σ^y, and obtain the differential equation

$$\frac{df_\alpha}{dx} = \frac{\alpha m(x)v}{\hbar} f_\alpha(x), \tag{2.43}$$

whose solutions are

$$f_\alpha(x) = \exp\left(\frac{\alpha v}{\hbar}\int_0^x dx' m(x')\right) f_\alpha(0) \tag{2.44}$$

It is now easily clear why there are unidirectional edge modes in this system. The total wave function is

$$\psi_\alpha(x,y) = f_\alpha(0)\exp\left(-i\alpha\delta k_y y\right)\exp\left(\frac{\alpha v}{\hbar}\int_0^x dx' m(x')\right) \tag{2.45}$$

These solutions correspond to localization in the x-direction and to free propagation in the y-direction. Formally, we have solutions corresponding to free propagation in the positive and negative y- directions (labeled by α). However, only normalizable states can correspond to physical states. We see then that we have to throw away the state that blows up exponentially in the x-direction and we are left with one state - *electrons will travel in one direction only.* The zero-modes of the Dirac equation are our quantum Hall edge modes.

In the next chapter we see how all this arises in a photonic context. We have been careful to never make use of a net magnetic flux - we have been working with Bloch states

until now. Indeed, the electronic poperties which give rise to quantum Hall effects - charge, and Fermi statistics, have not been invoked in the construction of the edge states.

Chapter 3

Photonic analogs of "chiral" quantum Hall edge states

3.1 Introduction

The control of the flow of light using photonic band-gap (PBG) materials has received considerable attention over the past decade [24]. Moreover, the potential for using artificially structured "metamaterials", such as the recently discovered "left-handed media" [39], has shown considerable technological promise. In the past, significant progress has been achieved in the field of photonics by making use of analogies with electronic systems. For instance, the typical PBG material, a system with a spatially varying and periodic dielectric function, was motivated by the well known physics of electronic Bloch states; the dielectric scattering of light in periodic media presents the same formal solutions as those for the scattering of electrons in periodic potentials.

Previous photonic bandstructure calculations have focused on the frequency dispersion of the photon bands; it has been usually been assumed that a knowledge of the spectrum alone represents a complete understanding of dynamics of the system. A primary goal of such calculations has been the quest for a PBG material with a complete bandgap throughout the Brillouin zone in some frequency range, which would prevent the transmission of light with

frequency in the range of the Band gap. Both two and three dimensional bandstructures possessing these properties have now been discovered [36].

Recently, however, in the study of electronic systems, it has become apparent that, even in the absence of interaction effects, the dispersion relations of the energy bands do not fully characterize the semiclassical dynamics of wavepackets, unless both spatial inversion symmetry and time-reversal symmetry are unbroken[56]. The additional information, which is not obtainable from knowledge of the energy bands $\epsilon_n(\boldsymbol{k})$ alone, is the variation of the Berry curvature[53] $\mathcal{F}_n^{ab}(\boldsymbol{k}) = \epsilon^{abc}\Omega_{nc}(\boldsymbol{k})$, which is an antisymmetric tensor in $\boldsymbol{k}$-space, where $\boldsymbol{\Omega}_n(\boldsymbol{k})$ is analogous to a "magnetic field" (flux density) in $\boldsymbol{k}$-space. The "Berry curvature" in $\boldsymbol{k}$-space is related to the Berry phase[6] in the same way that the Bohm-Aharonov phase of an electronic wavepacket is related to the magnetic flux density in real space.

While the uniform propagation of wavepackets in perfectly translationally-invariant systems does not involve the Berry curvature, the "semiclassical" description of the *acceleration* of wavepackets in media with spatial inhomogeneity of lengthscales large compared to the underlying lattice spacing is incomplete if it is not taken into account. Recently Onoda *et al.*[48] have pointed out the role of Berry curvature in photonic crystals without inversion symmetry; while these authors characterize this as a "Hall effect of light", the Hall effect in electronic systems is associated with broken *time-reversal symmetry* rather than broken spatial inversion symmetry, and we have recently discussed[20] some of the at-first-sight-surprising effects that broken time-reversal symmetry could produce in photonic systems.

In the presence of non-vanishing Berry curvature, the usual "semiclassical" expression for the group velocity of the wavepacket is supplemented by an additional "anomalous" contribution proportional to its acceleration and the local Berry curvature of the Bloch band. (The semiclassical treatment of electron dynamics becomes ray optics in the photonic context). This "anomalous velocity" has played an important role in understanding recent experiments on the anomalous Hall effect of ferromagnets [32], for example.

Perhaps the most remarkable among the "exotic" effects associated with Berry curvature, however, is the quantum Hall effect [63], which has been the focus of intensive

experimental and theoretical study in condensed matter physics for over two decades. The physics of the quantum Hall regime and its connection with Berry Curvature phenomena is now well understood. The possibility of transcribing some of the main features of the quantum Hall effect to photonic systems, which brings into play new possibilities in photonics, is the topic of this chapter. Specifically, we shall concern ourselves with analogs of "chiral" (unidirectional) quantum Hall edge states in photonic systems with broken time-reversal symmetry.

The quantum Hall effect is usually associated with two dimensional electron systems in semiconductor heterojunctions in strong applied magnetic fields. By treating the plane of the heterojunction as a featureless two-dimensional (2D) continuum, and considering the quantum mechanical motion of electrons in the presence of a magnetic field, one obtains the electronic Landau levels. The key feature giving rise to the quantization of the Hall conductance is the incompressibility of the electron fluid: either due to the Pauli principle at integer Landau level fillings, with the spectral gap to the next empty level given by the cyclotron frequency, or when a gap opens due to strong electron-electron interactions at fractional fillings[31].

While in the experimentally-realized systems, the quantum Hall effect derives from a strong uniform component of magnetic flux density normal to the 2D plane in which the electrons move, the integer quantum Hall effect can also in principle derive from the interplay of a periodic bandstructure with a magnetic field. An externally applied magnetic field in periodic structures gives rise to the celebrated Hofstadter model of Bloch bands with an elegant fractal spectral structure depending on the rational value of the magnetic flux through the unit cell [21] [10]. The influence of the lattice on the quantum Hall effect was further investigated in an important paper by Thouless et al (TKNN) [59], who discovered a topological invariant of 2D bandstructures known as the "Chern Number" a quantity that was later interpreted in terms of Berry curvature [53].

At first sight, it seems implausible that any of the phenomena associated with the quantum Hall effect can be transcribed to photonics. Incompressibility and Landau level

quantization require fermions and charged particles, respectively, and it is not clear how one could introduce an effect similar to the Lorentz force due to a magnetic field on a system of neutral bosons. However, a hint that possible analogs could exist in photonics, comes from the fact that a "zero-field" quantum Hall effect *without any net magnetic flux density* (and hence without Landau levels) could occur in systems consisting of "simple" Bloch states with Broken time-reversal symmetry, as was shown some time ago by one of us [19]. The explicit "graphene-like" model investigated in Ref. [19] exploits the topological properties of Bloch states, which motivated us to construct its photonic counterpart. This model has also turned out to be a very useful for modeling the anomalous Hall effect in ferromagnetic metals [49], and a recently proposed "quantum spin Hall effect"[25].

While incompressibility of the fluid in the bulk quantizes the Hall conductance, perhaps the most remarkable feature of quantum Hall systems is the presence of zero energy excitations along the *edge* of a finite system. In these edge states, electrons travel along a single direction: this "one-way" propagation is a symptom of broken time-reversal symmetry. In the case that the integer quantum Hall effect is exhibited by Bloch electrons, as in the Hofstadter problem studied by TKNN[59], it is related to the topological Chern invariant of the one-particle bands. The edge states necessarily occur at the interface between bulk regions in which there is a gap at the Fermi energy, which have different values of the sum of the Chern invariants of the fully occupied bands below the Fermi level. While the integer quantum Hall effect in such a system itself involves the filling of these bands according to the Pauli principle, and hence is essentially fermionic in nature, the existence of the edge states is a property of the one-electron band structure, without reference to the Pauli principle, which suggests that this feature is not restricted to fermionic systems. We have found that they indeed have a direct photonic counterpart, and this leads to the idea that topologically non-trivial *unidirectionally propagating photon modes* can occur along domain walls separating two PBG regions having different Chern invariants of bands below the band gap frequency. In this chapter, we present the formal basis of such modes, along with explicit numerical examples, simple model Hamiltonians, and semiclassical calculations confirming

the concept.

We note finally, that while Berry phases are usually associated with quantum mechanical interference, they can in principle occur wherever phase interference phenomena exist and are governed by Hermitian eigenvalue problems, as in the case of classical electromagnetic waves in loss-free media.

This chapter is organized as follows. In section II, we present the basic formalism of the Maxwell normal mode problem in periodic, loss-free media, discuss the Berry curvature of the photonic bandstructure problem, and consider the effects of broken time-reversal symmetry. In section III, we provide explicit numerical examples of bandstructures containing non-trivial topological properties, and show the occurrence of edge states along domain wall configurations. Motivated by the numerical results, in section IV, we derive a simple Dirac Hamiltonian from the Maxwell equations using symmetry arguments as the guiding principle, and we show how under certain conditions the *zero modes* of this Dirac Hamiltonian exhibit anomalous currents along a single direction due to the breaking of time-reversal symmetry. It is these zero modes that play the role of the "gapless" edge excitations, as we shall consider in detail. Section V contains semiclassical analysis, and we end with a discussion and point out possible future directions in section VI.

3.2 Berry Curvature in the Maxwell Normal-mode Problem

In this section, we discuss the formal basis of Berry curvature in the photon band problem. We begin with the basic formulation of the photonic bandstructure problem, which is somewhat more complicated than the electronic counterpart, due to the frequency response of dielectric media. We then briefly review the connection between Chern numbers, Berry curvature, and the occurrence of gapless edge modes along a boundary separating regions where the bands have different Chern numbers.

3.2.1 Basic Formalism

We will be solving the source-free Maxwell equations for propagating electromagnetic wave solutions in linear, loss-free media, and will ignore absorption, nonlinear photon-photon interactions, and other processes which do not conserve photon number. We also assume that the constitutive relations, reflecting the response of the media to the electromagnetic waves, are given by local, but spatially varying tensors with generalized frequency dependence. The Berry phase, and the associated Berry curvature, are commonly identified with quantum mechanics, but in fact are more generally associated with the adiabatic variation of the complex eigenvectors of a Hermitian eigenvalue system as the Hermitian matrix is varied.

In quantum mechanics, this Hermitian eigenvalue problem is the time-independent Schrödinger equation; in the photonic context, it is the classical eigenvalue equation for the normal modes of the Maxwell equations. In order to make the correspondence to the standard quantum-mechanical formulation of Berry curvature clearer, we will use a somewhat unfamiliar Hamiltonian formulation of Maxwell's equations, which is appropriate for loss-free linear media. However, we should emphasize that that our results are in no way dependent on the use of such a formalism, and are properties of the Maxwell equations, however they are written.

In such a loss-free, linear medium, the coupling of electromagnetic modes having different frequencies can be ignored, and the electromagnetic fields and flux densities $\boldsymbol{X}(\boldsymbol{r},t)$, $\boldsymbol{X} \in \{\boldsymbol{D},\boldsymbol{B},\boldsymbol{E},\boldsymbol{H}\}$ will be of the form

$$\boldsymbol{X}(\boldsymbol{r},t) = \left(\tilde{\boldsymbol{X}}^*(\boldsymbol{r},\omega)e^{i\omega t} + \tilde{\boldsymbol{X}}(\boldsymbol{r},\omega)e^{-i\omega t}\right), \tag{3.1}$$

where the quantities $\tilde{\boldsymbol{X}}$ are in general complex-valued functions of position and frequency with the property:

$$\left(\tilde{\boldsymbol{X}}(\boldsymbol{r},\omega)\right)^* = \tilde{\boldsymbol{X}}(\boldsymbol{r},-\omega). \tag{3.2}$$

The dynamics of these fields are governed by the source-free Maxwell equations:

$$\nabla \times \tilde{\boldsymbol{E}} = i\omega\tilde{\boldsymbol{B}} \quad , \quad \nabla \times \tilde{\boldsymbol{H}} = -i\omega\tilde{\boldsymbol{D}}, \tag{3.3}$$

$$\nabla \cdot \tilde{\boldsymbol{D}} = 0 \quad , \quad \nabla \cdot \tilde{\boldsymbol{B}} = 0. \tag{3.4}$$

Consider a single normal mode λ propagating at frequency ω_λ. For the moment, ignore any internal polarization or magnetization modes of the medium, and assume instantaneous, frequency-independent response of the dielectric material. In this limit, the permeability and permittivity tensors, defined by the relations

$$\tilde{B}^a(\boldsymbol{r}, \omega_\lambda) = \mu^{ab}(\boldsymbol{r}) \tilde{H}_b(\boldsymbol{r}, \omega_\lambda), \tag{3.5}$$

$$\tilde{D}^a(\boldsymbol{r}, \omega_\lambda) = \epsilon^{ab}(\boldsymbol{r}) \tilde{E}_b(\boldsymbol{r}, \omega_\lambda), \tag{3.6}$$

are both positive-definite Hermitian tensors and have well-defined, positive definite Hermitian inverses $\epsilon^{-1}_{ab}(\boldsymbol{r})$, $\mu^{-1}_{ab}(\boldsymbol{r})$. Since we have assumed a linear, loss-free medium in which photon number is conserved, it is convenient to work with a Hamiltonian formalism: the time-averaged energy density of the electromagnetic radiation field is given by

$$\mathcal{H}^{\mathrm{em}}(\boldsymbol{r}) = u^e(\boldsymbol{r}) + u^m(\boldsymbol{r}), \tag{3.7}$$

where

$$u^e(\boldsymbol{r}) = \frac{1}{2}\left(\tilde{\boldsymbol{D}}^*_\lambda, \epsilon^{-1}(\boldsymbol{r})\tilde{\boldsymbol{D}}_\lambda\right) \tag{3.8}$$

$$u^m(\boldsymbol{r}) = \frac{1}{2}\left(\tilde{\boldsymbol{B}}^*_\lambda, \mu^{-1}(\boldsymbol{r})\tilde{\boldsymbol{B}}_\lambda\right). \tag{3.9}$$

Then, if H^{em} is the spatial integral of the energy density, the fields $\boldsymbol{E}$ and $\boldsymbol{H}$ are given by its functional derivatives with respect to the divergence-free flux densities $\boldsymbol{D}$ and $\boldsymbol{B}$:

$$\delta H^{\mathrm{em}} = \int d^3\boldsymbol{r} E_a \delta B^a + H_a \delta B^a. \tag{3.10}$$

In the local Hamiltonian formalism, the flux density fields $\boldsymbol{D}(\boldsymbol{r})$ and $\boldsymbol{B}(\boldsymbol{r})$ are the fundamental degrees of freedom, and they obey the following non-canonical Poisson Bracket relations:

$$\{D^a(r), B^b(r')\}_{\mathrm{PB}} = \epsilon^{abc}\nabla_c \delta^3(r - r'). \tag{3.11}$$

This Poisson bracket generates the Faraday-Maxwell equations d(3.3):

$$\frac{d\boldsymbol{D}}{dt} = \{\boldsymbol{D}(\boldsymbol{r}), H^{\mathrm{em}}\}_{\mathrm{PB}}, \quad \frac{d\boldsymbol{B}}{dt} = \{\boldsymbol{B}(\boldsymbol{r}), H^{\mathrm{em}}\}_{\mathrm{PB}}. \tag{3.12}$$

Note that these equations do *not* generate the Gauss law equations (3.4), but merely ensure that any divergences $\nabla_a D^a$ and $\nabla_a B^a$ are constants of the motion; the Gauss laws are additional constraints that are compatible with the Faraday-Maxwell equations of motion.

If internal polarization and magnetization modes of the medium are ignored, a discretized form of the electromagnetic Hamiltonian is formally identical in structure to that of a collection of real oscillator variables x_i with non-canonical Poisson brackets

$$\{x_i, x_j\}_{\rm PB} = S_{ij}, \tag{3.13}$$

where S_{ij} is a real antisymmetric matrix, and the Hamiltonian energy function is

$$\mathcal{H} = \frac{1}{2}\sum_{ij} B_{ij} x_i x_j, \tag{3.14}$$

where B_{ij} is a real-symmetric positive-definite matrix. It is useful to introduce the imaginary antisymmetric Hermitian matrix $A_{ij} = iS_{ij}$; The canonical normal modes are given by

$$q_\lambda \pm ip_\lambda = (\gamma_\lambda)^{-1}\sum_i u^{\pm}_{i\lambda} x_i, \tag{3.15}$$

where γ_λ is an arbitrary scale factor, and where $(u^\sigma_{i\lambda})^* = u^{-\sigma}_{i\lambda}$, $\sigma = \pm$, which obeys the generalized Hermitian eigenvalue equation

$$\sum_j A_{ij} u^{\pm}_{j\lambda} = \pm\omega_\lambda \sum_j B^{-1}_{ij} u^{\pm}_{j\lambda}, \tag{3.16}$$

with $\omega_\lambda > 0$, and the orthogonality condition

$$\sum_{ij} (u^\sigma_{i\lambda})^* B^{-1}_{ij} u^{\sigma'}_{j\lambda'} = \frac{\gamma_\lambda^2}{\omega_\lambda}\delta_{\sigma\sigma'}\delta_{\lambda\lambda'}. \tag{3.17}$$

Because of the antisymmetric Hermitian property of the matrix A_{ij}, and the positive-definite real-symmetric property of the matrix B_{ij}, this eigenproblem has real eigenvalues that either come in pairs, $\pm\omega_\lambda$, or vanish; these equations provide a straightforward transformation to canonical form only if the generalized eigenvalue problem has no zero-frequency eigenvalues, which is only the case if A_{ij} is non-singular.

The coefficients $u_{i\lambda}$ are the analogs of the electromagnetic fields $\tilde{E}(\boldsymbol{r},\omega)$ and $\tilde{H}(\boldsymbol{r},\omega)$. It is also useful to introduce the conjugate quantities

$$v^\sigma_{i\lambda} = \sum_j B^{-1}_{ij} u^\sigma_{j\lambda}, \quad \sum_i (v^\sigma_{i\lambda})^* u^{\sigma'}_{i\lambda'} = \delta_{\sigma\sigma'}\delta_{\lambda\lambda'}; \tag{3.18}$$

these are the analogs of the flux densities $\tilde{\boldsymbol{D}}(\boldsymbol{r},\omega)$ and $\tilde{\boldsymbol{B}}(\boldsymbol{r},\omega)$, and B_{ij} encodes the "constitutive relations" between analogs of fluxes and fields.

The Hamiltonian formulation of the Maxwell equations indeed presents the difficulty of having a null space of zero-frequency eigenvalues: by themselves, the Faraday-Maxwell equations have static (zero-frequency) solutions $\tilde{\boldsymbol{B}}(\boldsymbol{r}) = \boldsymbol{\nabla} f(\boldsymbol{r})$, $\tilde{\boldsymbol{D}}(\boldsymbol{r}) = \boldsymbol{\nabla} g(\boldsymbol{r})$; the role of the additional Gauss law constraints is precisely to eliminate these zero modes. The zero-mode problem in the Hamiltonian formulation is the counterpart of the gauge ambiguity of the solutions of Maxwell's equations in the Lagrangian formulation.

In the Maxwell equations, B_{ij} becomes the following positive-definite 6×6 Hermitian matrix,

$$B_{ij} \to \begin{pmatrix} \epsilon_{ab}^{-1}(\boldsymbol{r}) & 0 \\ 0 & \mu_{ab}^{-1}(\boldsymbol{r}) \end{pmatrix}. \tag{3.19}$$

More precisely, this a 6×6 block of an infinite-dimensional "matrix" that is block-diagonal in terms of the spatial coordinate $\boldsymbol{r}$. (The "A" and "B" matrix notation is common in the context of generalized Hermitian eigenvalue problems, where the positive-definite character of the "B" matrix guarantees reality of the eigenvalues; hopefully the context should distinguish our use of the symbol B for such a matrix from the symbol $\boldsymbol{B}(\boldsymbol{r})$ used for the magnetic flux density.) In this continuum limit, the antisymmetric Hermitian matrix A_{ij} becomes a 6×6 matrix block of differential operators:

$$A^{ac} = \begin{pmatrix} 0 & i\epsilon^{abc}\nabla_b \\ -i\epsilon^{abc}\nabla_b & 0 \end{pmatrix}. \tag{3.20}$$

This A-matrix can be also be elegantly expressed using the 3×3 spin-1 matrix representations of the angular momentum algebra, $\left(L^b\right)^{ac} = i\epsilon^{abc}$:

$$A = \begin{pmatrix} 0 & \boldsymbol{L}^a\nabla_a \\ -\boldsymbol{L}^a\nabla_a & 0 \end{pmatrix}. \tag{3.21}$$

From the antisymmetry of A, it again follows that its eigenvalues come either in $\pm$ pairs, or are zero modes, corresponding to static field configurations. Due to the presence of a

huge band of zero modes (one third of the spectrum), the A matrix cannot be written in canonical form.

Using the Poisson-Brackets, we see that the equation of motion of the electric and magnetic fields is a generalized Hermitian eigenvalue problem of the form

$$\begin{pmatrix} 0 & \boldsymbol{L}^a\nabla_a \\ -\boldsymbol{L}^a\nabla_a & 0 \end{pmatrix} \begin{bmatrix} \tilde{\boldsymbol{E}}_\lambda \\ \tilde{\boldsymbol{H}}_\lambda \end{bmatrix} = \omega_\lambda \begin{pmatrix} \boldsymbol{\epsilon}(\boldsymbol{r}) & 0 \\ 0 & \boldsymbol{\mu}(\boldsymbol{r}) \end{pmatrix} \begin{bmatrix} \tilde{\boldsymbol{E}}_\lambda \\ \tilde{\boldsymbol{H}}_\lambda \end{bmatrix}. \tag{3.22}$$

In this formalism, the energy-density of the normal mode (time-averaged over the periodic cycle) is

$$u(\boldsymbol{r}) = \frac{1}{2} \begin{bmatrix} \tilde{\boldsymbol{E}}^*_\lambda & \tilde{\boldsymbol{H}}^*_\lambda \end{bmatrix} \begin{pmatrix} \boldsymbol{\epsilon}(\boldsymbol{r}) & 0 \\ 0 & \boldsymbol{\mu}(\boldsymbol{r}) \end{pmatrix} \begin{bmatrix} \tilde{\boldsymbol{E}}_\lambda \\ \tilde{\boldsymbol{H}}_\lambda \end{bmatrix}, \tag{3.23}$$

and the period-averaged averaged energy-current density (Poynting vector) is

$$j^a(\boldsymbol{r}) = \frac{1}{2} \begin{bmatrix} \tilde{\boldsymbol{E}}^*_\lambda & \tilde{\boldsymbol{H}}^*_\lambda \end{bmatrix} \begin{pmatrix} 0 & -i\boldsymbol{L}^a \\ i\boldsymbol{L}^a & 0 \end{pmatrix} \begin{bmatrix} \tilde{\boldsymbol{E}}_\lambda \\ \tilde{\boldsymbol{H}}_\lambda \end{bmatrix}. \tag{3.24}$$

For practical real-space-based calculations of the photonic normal mode spectrum with inhomogeneous local constitutive relations, it is very convenient to discretize the continuum Maxwell equations on a lattice (or network) in a way that they in fact have the matrix form (3.16), where the matrix A_{ij} reproduces the zero-mode (null space) structure of the continuum equations, and H_{ij} represents the local constitutive relations at network nodes (which come in dual types, electric and magnetic). In such a scheme, divergence-free electric and magnetic fluxes flow along the links of the interpenetrating dual electric and magnetic networks, while electromagnetic energy flows between electric and magnetic nodes, along the links between nodes of the network, satisfying a local continuity equation (see the following chapter). However, there is one further conceptual ingredient that needs to be added to the formalism before we can discuss the Maxwell normal modes in "non-reciprocal" media which have broken time-reversal symmetry.

3.2.2 Frequency dependence of the dielectric media

The formalism discussed so far treats the constitutive relations as static. In general, although we will treat them as spatially local, we cannot also treat them as instantaneous, and must in principle treat the local permittivity and permeability tensors as frequency-dependent, $\boldsymbol{\epsilon}(\boldsymbol{r}) \to \boldsymbol{\epsilon}(\boldsymbol{r},\omega)$, $\boldsymbol{\mu}(\boldsymbol{r}) \to \boldsymbol{\mu}(\boldsymbol{r},\omega)$. This is because a non-dissipative time-reversal-symmetry breaking component of these tensors is both imaginary and antisymmetric (as opposed to real symmetric) *and* is an odd function of frequency, making frequency-dependence inescapable in principle.

These effects can on the one hand be treated in a Hamiltonian formulation by adding extra local harmonic oscillator modes representing local polarization and magnetization degrees of freedom of the medium that couple to the electromagnetic fields. The full description of this is again a set of harmonic oscillator degrees of freedom described by equations of the form (3.16). On the other hand, with the assumption that we are treating the electromagnetic modes in a frequency range that is not resonant with any internal modes of the medium (*i.e.*, in a frequency range where the loss-free condition is satisfied), we can eliminate the internal modes to yield a purely-electromagnetic description, but with frequency dependent constitutive relations.

The details shall follow below, but we first state the result. If all oscillator degrees of freedom are explicitly described, the eigenvalue problem for the normal modes has the structure (3.16), where B_{ij}^{-1} is positive-definite and real-symmetric. This guarantees that the eigenvalues ω_λ are real. However, the normal modes in some positive frequency range $\omega_1 < \omega < \omega_2$ can be treated by eliminating modes with natural frequencies outside that range, to give an matrix-eigenvalue-like problem of much smaller rank of the form

$$\sum_j A_{ij} u_{j\lambda}^{\pm} = \pm\omega_\lambda \sum_j B_{ij}^{-1}(\omega_\lambda) u_{j\lambda}^{\pm}, \tag{3.25}$$

where $B_{ij}(\omega)$ is now a frequency-dependent matrix with a Kramers-Krönig structure. The matrix $B_{ij}(\omega)$ is no longer in general real-symmetric, but provided the eliminated modes are not resonant in the specified frequency range it instead is generically complex Hermitian.

The "eigenvalue equation" is now a self-consistent equation:

$$\sum_j A_{ij} u^{\pm}_{j\lambda}(\omega) = \pm\omega_\lambda(\omega) \sum_j B^{-1}_{ij}(\omega) u^{\pm}_{j\lambda}(\omega). \tag{3.26}$$

This must be solved by varying ω till it coincides with an eigenvalue. Unfortunately, while $B^{-1}_{ij}(\omega)$ is Hermitian and non-singular in the dissipationless frequency range $\omega_1 < \omega < \omega_2$, it is *not* necessarily positive definite, so *a priori*, the eigenvalues $\omega_\lambda(\omega)$ are not guaranteed to be real, except for the fact that we know that these equations were derived from a standard frequency-independent eigenvalue problem which does have real eigenvalues. As shown in subsection 3.2.3, the Kramers-Kronig structure of $B_{ij}(\omega)$ reflects the stability of the underlying full oscillator system, giving the condition that a modified matrix

$$\tilde{B}^{-1}_{ij}(\omega)) = \frac{d}{d\omega}\left(\omega B^{-1}_{ij}(\omega)\right) \tag{3.27}$$

is positive-definite Hermitian in the specified frequency range, which is sufficient to guarantee reality of the eigenvalues in that range. Furthermore, the quadratic expression for the energy of a normal mode solution is given in terms of $\tilde{B}^{-1}_{ij}(\omega_\lambda)$ rather than $B^{-1}_{ij}(\omega_\lambda)$, reflecting the fact that the total energy of the mode resides in both the explicitly-retained degrees of freedom (the "electromagnetic fields") and the those which have been "integrated out" (the non-resonant polarization and magnetization modes of the medium):

$$x_i(t) = B^{-1}_{ij}(\omega_\lambda) u^{+}_{j\lambda} e^{i\omega_\lambda t} + c.c., \omega_\lambda > 0, \tag{3.28}$$

$$H = \frac{1}{2}\sum_{ij} \tilde{B}^{-1}_{ij}(\omega_\lambda)(u^{+}_{i\lambda})^* u^{+}_{j\lambda}, \frac{dH}{dt} = 0. \tag{3.29}$$

If the frequency dependence of the positive-definite Hermitian matrix $\tilde{B}_{ij}(\omega)$ is negligible in the range $\omega_1 < \omega < \omega_2$, so $\tilde{B}_{ij}(\omega) \approx \tilde{B}_{ij}(\omega_0)$, with $\omega_0 = (\omega_1 + \omega_2)/2$, one can replace $B^{-1}_{ij}(\omega)$ in (3.25) by the positive-definite frequency-independent Hermitian matrix $\tilde{B}^{-1}_{ij}(\omega_0)$. This in turn allows the eigenvalue problem to be transformed into the standard Hermitian eigenvalue problem

$$H_{ij} w^{(\lambda)}_j = \omega_\lambda w^{(\lambda)}_i, \quad \left(\boldsymbol{w}^{(\lambda)}, \boldsymbol{w}^{(\lambda')}\right) = \delta_{\lambda\lambda'}, \tag{3.30}$$

with scalar product

$$(\boldsymbol{w}, \boldsymbol{w}') \equiv \sum_j w^*_j w'_j, \tag{3.31}$$

valid for positive ω_λ in the frequency range where $\tilde{B}_{ij}(\omega) \approx \tilde{B}_{ij}(\omega_0)$, with

$$H_{ij} = \left(\tilde{B}^{1/2}(\omega_0) A \tilde{B}^{1/2}(\omega_0)\right)_{ij}, \tag{3.32}$$

and

$$u^+_{i\lambda} \propto \sum_j \tilde{B}^{1/2}_{ij}(\omega_0) w_{j\lambda}. \tag{3.33}$$

This allows well-known Berry-curvature formulas from the standard Hermitian eigenproblem [53] to be quickly translated into the generalized problem. It turns out that when the full problem with frequency-dependent constitutive relations is treated, the standard formula for the *Berry connection* remains correct with the simple replacement $\tilde{B}_{ij}(\omega_0) \to \tilde{B}_{ij}(\omega_\lambda)$ (the Berry curvature and Berry phase can both be expressed in terms of this Berry connection).

3.2.3 Technical details

In this section, we shall provide the details of the generalization of the normal mode problem to include the frequency-dependent response of the media outlined above. We shall couple the electromagnetic fields to harmonic oscillator degrees of freedom of the medium. Defining $\phi_{i\sigma}$ and $\pi_{i\sigma}$ $(i = 1, \cdots N,\ \sigma = \epsilon, \mu)$ to be a set of N independent canonically conjugate oscillator coordinates and momenta respectively, which represent internal polarization and magnetization modes, we consider the total Hamiltonian

$$H = H^{em} + \sum_\sigma H^\sigma\ , (\sigma = \epsilon, \mu), \tag{3.34}$$

where, for instance,

$$H^\epsilon = \sum_i D^a \left(\alpha_{i\epsilon}(\boldsymbol{r})^a \pi_{i\epsilon}(\boldsymbol{r}) + \beta^a_{i\epsilon}(\boldsymbol{r}) \phi_{i\epsilon}(\boldsymbol{r})\right) + \frac{1}{2} \sum_i \omega_{i\epsilon} \left(\pi_{i\epsilon}(\boldsymbol{r})^2 + \phi_{i\epsilon}(\boldsymbol{r})^2\right).$$

The first term above represents the local coupling between the electric fluxes and the polarization modes, whereas the second term represents the energy of the oscillators themselves. A similar equation exists for the magnetization degrees of freedom coupled with the

magnetic fluxes. The Hamiltonian, as stated in Eq.(3.34), is real-symmetric and positive-definite, and therefore, its eigenvalues are real. The electric and magnetic fields are obtained by varying the Hamiltonian with respect to the associated flux densities: $E_a(\boldsymbol{r}) = \delta\mathcal{H}/\delta D^a(\boldsymbol{r})$, $H_a(\boldsymbol{r}) = \delta\mathcal{H}/\delta B^a(\boldsymbol{r})$

$$E_a(\boldsymbol{r}) = \epsilon^{-1}_{ab}(\boldsymbol{r})D^b(\boldsymbol{r}) + \sum_n \left(\alpha^a_{n\epsilon}(\boldsymbol{r})\phi_{n\epsilon}(\boldsymbol{r}) + \beta^a_{n\epsilon}(\boldsymbol{r})\pi_{n\epsilon}(\boldsymbol{r})\right), \tag{3.35}$$

and similarly for the field H_a. The time-evolution of the oscillator modes are obtained from the Hamilton equations of motion (letting $\partial_t\phi_{n\sigma} = -i\omega\phi_{n\sigma}$, etc)

$$-i\omega\phi_{n\epsilon}(\boldsymbol{r}) = \frac{\delta\mathcal{H}}{\delta\pi_{n\epsilon}(\boldsymbol{r})} = \omega_{n\epsilon}\pi_n(\boldsymbol{r}) + \beta^a_n(\boldsymbol{r})D^a(\boldsymbol{r}) \tag{3.36}$$

$$i\omega\pi_{n\epsilon}(\boldsymbol{r}) = \frac{\delta\mathcal{H}}{\delta\phi_{n\epsilon}(\boldsymbol{r})} = \omega_{n\epsilon}\phi_{n\epsilon}(\boldsymbol{r}) + \alpha^a_{n\epsilon}(\boldsymbol{r})D^a(\boldsymbol{r}). \tag{3.37}$$

We invert this equation to solve for the oscillator coordinates and momenta in terms of the fluxes:

$$\begin{pmatrix} \phi_{n\epsilon}(\boldsymbol{r}) \\ \pi_{n\epsilon}(\boldsymbol{r}) \end{pmatrix} = \frac{1}{\omega^2 - \omega_n^2} \begin{pmatrix} \omega_n & i\omega \\ -i\omega & \omega_n \end{pmatrix} \begin{pmatrix} \alpha^a_{n\epsilon}(\boldsymbol{r}) \\ \beta^a_{n\epsilon}(\boldsymbol{r}) \end{pmatrix} D^a(\boldsymbol{r}). \tag{3.38}$$

By substituting Eq.(3.38) into the expression for the electric field (3.35), we obtain a correction $\delta\epsilon^{-1}_{ab}(\boldsymbol{r}\ \omega)$ to the permittivity tensor coming from the oscillator modes:

$$\delta\epsilon^{-1}_{ab}(\boldsymbol{r}\ \omega) = \sum_n \left(\frac{\Gamma^\epsilon_{ab}(\boldsymbol{r})(\omega+\omega_n) - \Gamma^{*\epsilon}_{ab}(\boldsymbol{r})(\omega-\omega_n)}{\omega^2 - \omega_n^2}\right), \tag{3.39}$$

where

$$\Gamma^{ab}_\epsilon(\boldsymbol{r}) = \left(\alpha^a_{n\epsilon}(\boldsymbol{r}) - i\beta^a_{n\epsilon}(\boldsymbol{r})\right)\left(\alpha^b_{n\epsilon}(\boldsymbol{r}) + i\beta^b_{n\epsilon}(\boldsymbol{r})\right). \tag{3.40}$$

Finally, the correction term above to the permittivity is expressed in Kramers-Krönig form as

$$\delta\epsilon^{-1}_{ab}(\boldsymbol{r},\ \omega) = \sum_n \left(\frac{\Gamma^\epsilon_{ab}(\boldsymbol{r})}{\omega - \omega_n} - \frac{\Gamma^{\epsilon*}_{ab}(\boldsymbol{r})}{\omega + \omega_n}\right). \tag{3.41}$$

The same formal manipulations occur in the frequency dependence of the magnetization modes; in the end, the constitutive relations are given by a tensor $B(\boldsymbol{r},\ \omega)$ defined by

$$B(\boldsymbol{r},\omega) = \begin{pmatrix} \epsilon^{-1}(\boldsymbol{r},\ \omega) & 0 \\ 0 & \mu^{-1}(\boldsymbol{r},\ \omega) \end{pmatrix}, \tag{3.42}$$

which is written in Kramers-Kronig form as:

$$B_{ab}(\boldsymbol{r},\ \omega) = S_{ab}(\boldsymbol{r}) + \sum_n \left(\frac{\Gamma_{ab}(\boldsymbol{r})}{\omega - \omega_n} - \frac{\Gamma^*_{ab}(\boldsymbol{r})}{\omega + \omega_n} \right). \tag{3.43}$$

The first term, $S_{ab}(\boldsymbol{r}) = \lim_{\omega\to\infty} B(\boldsymbol{r},\ \omega)$ is the same tensor defining the Hamiltonian in Eq.(3.14). In the zero frequency limit,

$$B_{ab}(\boldsymbol{r},\ 0) = S_{ab}(\boldsymbol{r}) - \sum_n \left(\frac{\Gamma_{ab}(\boldsymbol{r}) + \Gamma^*_{ab}(\boldsymbol{r})}{\omega_n} \right). \tag{3.44}$$

Stability of the medium imposes the following important constraint:

$$B(\boldsymbol{r},\ 0) > 0. \tag{3.45}$$

Eliminating S_{ab} in Eq.(3.43) using Eq.(3.44), we get

$$\delta B(\omega) = \sum_n \left[\Gamma \left(\frac{\omega}{\omega_n(\omega - \omega_n)} \right) + \Gamma^* \left(\frac{\omega}{\omega_n(\omega + \omega_n)} \right) \right]$$

where $\delta B(\omega) = B(\omega) - B(0)$. Whereas $B(\omega)$ is not a positive-definite matrix, the quantity which is guaranteed to be positive-definite in lossless frequency ranges is

$$\tilde{B}(\omega) = B(\omega) - \omega \frac{\partial}{\partial \omega} B(\omega) > 0, \tag{3.46}$$

because

$$\tilde{B}(\omega) = B(0) + \sum_n \frac{1}{\omega_n} \left[\Gamma_n \left(\frac{\omega}{\omega - \omega_n} \right)^2 + \Gamma^*_n \left(\frac{\omega}{\omega + \omega_n} \right)^2 \right], \tag{3.47}$$

and Γ_n, Γ^*_n, and $B(0)$ are all positive-definite tensors.

Although $B(\omega)$ is not positive-definite, we will be interested in cases where

$$\det(B(\omega)) = 0. \tag{3.48}$$

When this condition is satisfied and $B(\omega)$ has no zero modes corresponding to metallic conditions, there is a well defined inverse tensor $B^{-1}(\omega)$

$$B^{-1}(\boldsymbol{r},\ \omega) = \begin{pmatrix} \epsilon(\boldsymbol{r},\ \omega) & 0 \\ 0 & \mu(\boldsymbol{r},\ \omega) \end{pmatrix}. \tag{3.49}$$

From the stability condition stated for $B(\omega)$, there exists a similar condition for $B^{-1}(\omega)$:

$$B - \omega\frac{\partial}{\partial\omega}B = B\left(B^{-1} + \omega\frac{\partial}{\partial\omega}B^{-1}\right)B > 0,$$

where we have made use of $B^{-1}B = 1$ and $\partial/\partial\omega\left(B^{-1}B\right) = 0$. Supplementing the inequality above with the condition in Eq.(3.48), we obtain

$$\tilde{B}^{-1}(\omega) \equiv \frac{\partial}{\partial\omega}\left(\omega B^{-1}(\omega)\right) > 0. \tag{3.50}$$

The eigenvalue problem is solved for each value of the Bloch vector $\boldsymbol{k}$ in the first Brillouin zone, and The formal strategy for obtaining the energy eigenvalues is to solve $\boldsymbol{A}|\boldsymbol{u}_n(\boldsymbol{k})\rangle = \omega_n(\boldsymbol{k})\boldsymbol{B}^{-1}(\omega(\boldsymbol{k}))|\boldsymbol{u}_n(\boldsymbol{k})\rangle$, and then to *vary* ω until it coincides with a frequency of an eigenmode. The stability condition (see Eq.(3.50)) guarantees that such a prescription enables us to find the entire spectrum in a lossless range of real frequencies, where $\tilde{B}^{-1}$ is Hermitian.

Indeed, if we consider for the moment the Hermitian problem

$$\left(\boldsymbol{A} - \omega\boldsymbol{B}^{-1}(\omega)\right)|\boldsymbol{u}_n\rangle = \lambda_n(\omega)|\boldsymbol{u}_n\rangle, \tag{3.51}$$

and vary ω to find the *zero modes*

$$\lambda_n(\omega) = 0, \tag{3.52}$$

the stability of such a prescription is guaranteed only if

$$\frac{\partial\lambda_n}{\partial\omega} < 0, \tag{3.53}$$

so that the eigenvalues are monotonically-decreasing functions of ω. But from first-order perturbation theory, we know that the requirement above is satisfied only if

$$\langle \boldsymbol{u}_n | \frac{d}{d\omega} \left(\omega B^{-1}(\omega) \right) | \boldsymbol{u}_n \rangle > 0, \tag{3.54}$$

which is precisely equivalent to the condition in Eq.(3.50).

When we eliminate the internal oscillator (polariton) modes and explicitly substitute the expressions in Eq.(3.38) into the total Hamiltonian, Eq. (3.34), we obtain the following quadratic form that involves only the electromagnetic flux densities:

$$H = \frac{1}{2} \sum_{ij} \tilde{B}^{-1}_{ij}(\omega)(u_i)^* u_j. \tag{3.55}$$

Our result can be summarized as follows. We begin with our total Hamiltonian, Eq.(3.34), which can be written as a positive-definite real-symmetric matrix whose states live in an enlarged Hilbert space containing electromagnetic flux densities and internal oscillator modes. When we "integrate out" the non-resonant internal oscillator modes of the media, we are left with a set of effective constitutive relations of the form

$$v_{i\lambda} = \sum_j B_{ij}(\omega_\lambda) u^+_{j\lambda} e^{i\omega_\lambda t} + c.c., \tag{3.56}$$

and an effective Hamiltonian (which represents the conserved time-averaged energy density of the electromagnetic fields as well as the oscillator modes) that involves a *different* tensor $\tilde{B}_{ij}(\omega)$ given in 3.55. Using the relation in Eq.(3.46), we can equivalently write the Hamiltonian as

$$H = \frac{1}{2} \sum_{ij} \tilde{B}_{ij}(v_i)^* v_j. \tag{3.57}$$

For the case of generalized frequency dependence considered here, the normalization of the electromagnetic fields are given (up to a scale factor) in terms of the time-averaged energy density, Eq.(3.55):

$$\sum_{\mu\nu} \left(\boldsymbol{u}_\mu)^*, \tilde{\boldsymbol{B}}^{-1}(\omega_\mu) \boldsymbol{u}_\nu \right) = \frac{1}{\omega_\mu} \delta_{\mu\nu}. \tag{3.58}$$

Finally, the matrix $\tilde{\boldsymbol{B}}^{-1}$ and *not* $\boldsymbol{B}^{-1}$ enters the expression for the Berry connection, since it also defines the normalization of our states.

3.2.4 Berry curvature in Hermitian eigenproblems

Let $H_{ij}(\boldsymbol{g})$ be a family of complex Hermitian matrices defined on a manifold parameterized by a set $\boldsymbol{g}$ of independent coordinates g^μ, $\mu = 1, \ldots D$ It is assumed that the matrix is generic, so its eigenvalues are all distinct; as it is well-known, three independent parameters must be "fine-tuned" to produce a "accidental degeneracy" between a pair of eigenvalues. Thus if the parametric variation of the Hermitian matrix is confined to a two-parameter submanifold, each eigenvalue $\omega_\lambda(\boldsymbol{g})$ will generically remain distinct. Under these circumstances, the corresponding eigenvector is fully defined by the eigenvalue equation and normalization condition, up to multiplication by a unimodular phase factor, that can vary on the manifold:

$$w_{\lambda i}(\boldsymbol{g}) \to e^{i\phi(\boldsymbol{g})} w_{\lambda i}(\boldsymbol{g}). \tag{3.59}$$

This is the well-known "$U(1)$ gauge ambiguity" of the complex Hermitian eigenproblem. Associated with each eigenvector is a gauge-field (vector potential in the parameter space), called the "Berry connection":

$$\mathcal{A}_\mu^{(\lambda)}(\boldsymbol{g}) = -i \left(\mathbf{w}_\lambda(\mathbf{g})\right), \partial_\mu \mathbf{w}_\lambda(\mathbf{g})\big) , \quad \partial_\mu \equiv \frac{\partial}{\partial g^\mu}. \tag{3.60}$$

This field on the manifold is gauge-dependent, like the electromagnetic vector potential $\boldsymbol{A}(\boldsymbol{r})$, but its curvature (the "Berry curvature"), the analog of the magnetic flux density $\boldsymbol{B}(\boldsymbol{r}) = \boldsymbol{\nabla} \times \boldsymbol{A}(\boldsymbol{r})$, is gauge invariant and given by

$$\mathcal{F}_{\mu\nu}^{(\lambda)}(\boldsymbol{g}) = \partial_\mu \mathcal{A}_\nu^{(\lambda)}(\boldsymbol{g}) - \partial_\nu \mathcal{A}_\mu^{(\lambda)}(\boldsymbol{g}). \tag{3.61}$$

The Berry phase associated with a closed path Γ in parameter space is given (modulo 2π) by

$$\exp\left(-i\phi^{(\lambda)}(\Gamma)\right) = \exp\left(-i \oint_\Gamma \mathcal{A}_\mu(\boldsymbol{g}) dg^\mu\right). \tag{3.62}$$

.

Ignoring frequency-dependence, the oscillator system has

$$\boldsymbol{H}(\boldsymbol{g}) = \boldsymbol{B}^{1/2}(\boldsymbol{g}) \boldsymbol{A} \boldsymbol{B}^{1/2}(\boldsymbol{g}), \tag{3.63}$$

where the positive-definite Hermitian matrix $\boldsymbol{B}(\boldsymbol{g})$ can continuously vary as a function of some parameters $\boldsymbol{g}$, but $\boldsymbol{A}$ is invariant. Then converting to the oscillator variables gives

$$\mathcal{A}_\mu^{(\lambda)}(\boldsymbol{g}) \;=\; \text{Im.}\left(\frac{\left(\boldsymbol{u}^{(\lambda)},\tilde{\boldsymbol{B}}^{-1}(\boldsymbol{g},\omega_\lambda)\partial_\mu\boldsymbol{u}^{(\lambda)}\right)}{\left(\boldsymbol{u}^{(\lambda)},\tilde{\boldsymbol{B}}^{-1}(\boldsymbol{g},\omega_\lambda)\boldsymbol{u}^{(\lambda)}\right)}\right). \tag{3.64}$$

Here $\boldsymbol{B}^{-1}(\boldsymbol{g})$ has been replaced by $\tilde{\boldsymbol{B}}^{-1}(\boldsymbol{g},\omega_\lambda)$ which is the correct result when frequency dependence of $\boldsymbol{B}^{-1}(\boldsymbol{g},\omega)$ is taken into account (see subsection 3.2.3).

3.2.5 Photonic bands and Berry curvature

In the case of periodic systems, the normal modes have discrete translational symmetry classified by a Bloch vector $\boldsymbol{k}$ defined in the Brillouin zone, *i.e.*, defined modulo a reciprocal vector $\boldsymbol{G}$. For fixed $\boldsymbol{k}$, the spectrum of normal mode frequencies $\omega_n(\boldsymbol{k})$ is discrete, labeled by band indices n, and, as emphasized by Sundaram and Niu[56] in the electronic context, the Bloch vector of a wavepacket plays the role of the control-parameter vector $\boldsymbol{g}$.

In order to compute the Berry curvature of the photon band Bloch states, we shall find it convenient to work in a fixed Hilbert space for all Bloch vectors $\boldsymbol{k}$, and we do this by performing a unitary transformation on the $\boldsymbol{A}$ "matrix" (which becomes the 6×6 matrix of differential operators (3.20) in the continuum formulation of the Maxwell equations) as

$$\boldsymbol{A}(\boldsymbol{k},\boldsymbol{\nabla}) \equiv e^{-i\boldsymbol{k}\cdot\boldsymbol{r}}\boldsymbol{A}(\boldsymbol{\nabla})e^{i\boldsymbol{k}\cdot\boldsymbol{r}} = \boldsymbol{A}(\boldsymbol{\nabla}+i\boldsymbol{k}). \tag{3.65}$$

Note that parametric dependence on the Bloch vector $\boldsymbol{k}$ is a little different from parametric dependence on parameters $\boldsymbol{g}$ that control the Hamiltonian. After projection into a subspace of fixed $\boldsymbol{k}$, the "$\boldsymbol{A}$" matrix also becomes parameter-dependent, while (if the constitutive relations are taken to be completely local) the "$\boldsymbol{B}$" matrix in the photonics case is only implicitly $\boldsymbol{k}$-dependent through its self-consistent dependence on the frequency eigenvalue. (Parameter-dependence of the "$\boldsymbol{A}$" matrix does not affect the expression (3.64) for the Berry connection.)

The discrete eigenvalue spectrum $\omega_n(\boldsymbol{k})$ is then obtained by solving the self-consistent matrix-differential-equation eigenvalue problem:

$$\boldsymbol{A}(\boldsymbol{k},\boldsymbol{\nabla})\boldsymbol{u}_n(\boldsymbol{k},\boldsymbol{r}) = \omega_n(\boldsymbol{k})\boldsymbol{B}^{-1}(\boldsymbol{r},\omega_n(\boldsymbol{k}))\boldsymbol{u}_n(\boldsymbol{k},\boldsymbol{r}), \tag{3.66}$$

where $\boldsymbol{B}^{-1}(\boldsymbol{r},\omega)$ is the 6×6 block-diagonal permittivity-permeablity tensor $\mathrm{diag}(\boldsymbol{\epsilon}(\boldsymbol{r},\omega),\boldsymbol{\mu}(\boldsymbol{r},\omega))$, and $\boldsymbol{u}_n(\boldsymbol{k},\boldsymbol{r})\exp i\boldsymbol{k}\cdot\boldsymbol{r}$ represents the 6-component complex vector $(\tilde{\boldsymbol{E}}_n(\boldsymbol{k},\boldsymbol{r}),\tilde{\boldsymbol{H}}_n(\boldsymbol{k},\boldsymbol{r}))$ of electromagnetic fields of the normal mode with Bloch vector $\boldsymbol{k}$ and frequency $\omega_n(\boldsymbol{k})$. The eigenfunction satisfies the periodic boundary condition $\boldsymbol{u}_n(\boldsymbol{k},\boldsymbol{r}+\boldsymbol{R})=\boldsymbol{u}_n(\boldsymbol{k},\boldsymbol{r})$, where $\boldsymbol{R}$ is any lattice vector of the photonic crystal, where $\boldsymbol{B}^{-1}(\boldsymbol{r}+\boldsymbol{R},\omega)=\boldsymbol{B}^{-1}(\boldsymbol{r},\omega)$.

The transcription of Eq.(3.64) to the case of periodic media then gives the three-component Berry connection (vector potential) in $\boldsymbol{k}$-space as

$$\mathcal{A}^a_{(n)}(\boldsymbol{k})=\mathrm{Im.}\left(\frac{\left(\boldsymbol{u}_n(\boldsymbol{k}),\tilde{\boldsymbol{B}}^{-1}(\omega_n(\boldsymbol{k}))\nabla^a_k\boldsymbol{u}_n(\boldsymbol{k})\right)}{\left(\boldsymbol{u}_n(\boldsymbol{k}),\tilde{\boldsymbol{B}}^{-1}(\omega_n(\boldsymbol{k}))\boldsymbol{u}_n(\boldsymbol{k})\right)}\right). \tag{3.67}$$

The scalar products in Eq.(3.67) are defined by the trace over the six components of $\boldsymbol{u}_n(\boldsymbol{k},\boldsymbol{r})$, plus integration of the spatial coordinate $\boldsymbol{r}$ over a unit cell of the photonic crystal. By construction, if a "Berry gauge transformation" $\boldsymbol{u}_n(\boldsymbol{k},\boldsymbol{r})\rightarrow\boldsymbol{u}_n(\boldsymbol{k},\boldsymbol{r})\exp i\chi_n(\boldsymbol{k})$ is made, $\mathcal{A}^a_{(n)}(\boldsymbol{k})\rightarrow\mathcal{A}^a_{(n)}(\boldsymbol{k})+\nabla^a_k\chi_n(\boldsymbol{k})$.

In three-dimensional $\boldsymbol{k}$-space, the antisymmetric Berry curvature tensor $\mathcal{F}^{ab}_{(n)}(\boldsymbol{k})=\nabla^a_k\mathcal{A}^b_{(n)}(\boldsymbol{k})-\nabla^b_k\mathcal{A}^a_{(n)}(\boldsymbol{k})$ can also be represented as the three-component "Berry flux density" $\Omega^{(n)}_a(\boldsymbol{k})=\epsilon_{abc}\nabla^b_k\mathcal{A}^c_{(n)}(\boldsymbol{k})$ (the $\boldsymbol{k}$-space curl of the Berry connection), to emphasize the duality between $\boldsymbol{r}$-space and $\boldsymbol{k}$-space, and the analogy between Berry flux in $\boldsymbol{k}$-space and magnetic flux in $\boldsymbol{r}$-space,

If a wavepacket travels adiabatically (without interband transitions) through a region with slow spatial variation of the properties of the medium, so the photonic normal-mode eigenvalue spectrum can be represented as a position-dependent dispersion relation $\omega_n(\boldsymbol{k},\boldsymbol{r})$, the wavepacket must be accelerated as its mean Bloch vector $\boldsymbol{k}$ slowly changes to keep its frequency constant. When translated into the language of photonics, the semiclassical electronic equations of motion then become the equations of ray optics:

$$\hat{n}^a\frac{dk_a}{dt} = -\hat{n}^a\nabla_a\omega_n(\boldsymbol{k},\boldsymbol{r}), \tag{3.68}$$

$$\frac{dr^a}{dt} = \nabla^a_k\omega_n(\boldsymbol{k},\boldsymbol{r})+\mathcal{F}^{ab}_n(\boldsymbol{k},\boldsymbol{r})\frac{dk_b}{dt}, \tag{3.69}$$

where $\hat{n}\propto d\boldsymbol{r}/dt$ is parallel to the ray path, $\nabla_a\equiv\partial/\partial r^a$ and $\nabla^a_k\equiv\partial/\partial k_a$ (it is useful to use covariant and contravariant indices to distinguish components of spatial coordinates r^a

from the dual Bloch vector components k_a). The Bloch-space Berry curvature $\mathcal{F}_n^{ab}(\boldsymbol{k}, \boldsymbol{r})$ controls the additional "anomalous velocity[27]" correction in (3.69) to the familiar group velocity of a wave packet $v_n^a(\boldsymbol{k}) = \nabla_k^a \omega_n(\boldsymbol{k})$, which is active only when the wavepacket is being accelerated by the inhomogeneity of the medium.

Before we conclude our general discussion on Berry curvature in photon band systems, we must state the constraints that inversion and time-reversal symmetries place on the tensor $\mathcal{F}_n^{ab}(\boldsymbol{k})$. In what follows, we will use the Bloch state $\boldsymbol{w}_n$ defined in Eq.(3.33). If inversion symmetry (I) is present, the periodic part of the Bloch state $\boldsymbol{w}_n(\boldsymbol{k}$ has the following property: $\boldsymbol{w}_n(\boldsymbol{k}) = \boldsymbol{w}_n(-\boldsymbol{k})$ whereas if time-reversal symmetry (T) is present, $\boldsymbol{w}_n(\boldsymbol{k}) = \boldsymbol{w}_n^*(-\boldsymbol{k})$. If only (I) is present, it then follows that $\mathcal{F}_n^{ab}(\boldsymbol{k}) = \mathcal{F}_n^{ab}(-\boldsymbol{k})$, whereas if only (T) is present, $\mathcal{F}_n^{ab} = -\mathcal{F}_n^{ab}(-\boldsymbol{k})$. If *both* symmetries are present, then the Berry Curvature is identically zero everywhere except at isolated points of "accidental degeneracy", where it is not well-defined. When $\mathcal{F}_n^{ab}$ is non-zero, the phases of the Bloch vectors cannot all be chosen to be real. These properties will be crucial when we consider the effects of various symmetry-breaking perturbations on the photon band structure.

3.2.6 Topological structure of the photon bands

The main consequence of having bands with non-zero Berry curvature field is that if the path C is closed and encloses an entire Brillouin zone, the single-valuedness of the state $\boldsymbol{w}_n$ requires that

$$\exp\left(\oint \mathcal{A}_n^a dk_a\right) = \exp\left(\int\int dk_a \wedge dk_b \mathcal{F}_n^{ab}\right) = 1$$

or,

$$\int\int_{S_C} dk_a \wedge dk_b \mathcal{F}_n^{ab} = 2\pi \mathcal{C}_n^{(1)}, \tag{3.70}$$

where $\mathcal{C}_n^{(1)}$ is an integer, the *Chern invariant* associated with the nth band, and have well-known consequences in the quantum Hall effect: in the integer quantum Hall effect, where the interactions among electrons are weak, the Hall conductance is expressed in terms of the sum of all Chern invariants of bands below the Fermi level [59]:

$$\sigma_H = \frac{e^2}{2\pi\hbar} \sum_{i,\epsilon_i<\epsilon_f} \mathcal{C}_i^{(1)}. \tag{3.71}$$

The gauge structure of the photon band problem outlined above is formally analogous to the local $U(1)$ gauge invariance of ordinary electromagnetism. Note that the gauge invariance refers to the phase of the of the six-component electromagnetic fields as a whole; adding arbitrary phase $\boldsymbol{k}$-dependent phase factors to each field separately will in general not preserve the Maxwell equation constraint.

A phase convention can be specified, for instance, by arbitrarily choosing real and imaginary axes of the phases; the local gauge-dependent phase fields of the electromagnetic Bloch states are then represented as two-component rotor variables at each point of the Brillouin zone. In addition, a gauge choice may be made separately for each band so long as the spectrum remains non-degenerate.

By representing the phase covering on the Bloch manifold this way, the possibility of the occurrence of topological defects of the gauge field become transparent. Local gauge transformations correspond to local smooth deformations of the rotor variables, and the Chern invariant corresponds to the total winding number of theses rotor variables along a closed path enclosing the entire Brillouin zone.

In the case of two dimensional Bloch bands, the defects of the phase field are gauge singularities, having a zero-dimensional point-like "core" region where a phase convention is not well defined. It is clear that Bands can have non-zero Chern numbers only if time-reversal symmetry is broken. Otherwise, the Berry curvature will be an odd function of k, and its integral over the entire 2D Brillouin zone vanishes.

In three dimensions, the defects of the phase field are line defects or "vortices" and their stability requires quasi- degeneracies to occur along isolated *lines* in reciprocal space.

In the photonic system of interest, even if photon bands can have non-zero Chern numbers, there can be no Hall conductance as given above due to their Bose statistics (and hence, to their finite compressibility). However, the connection between *edge modes* and Chern invariants is independent of statistics: if the Chern number of a band changes at

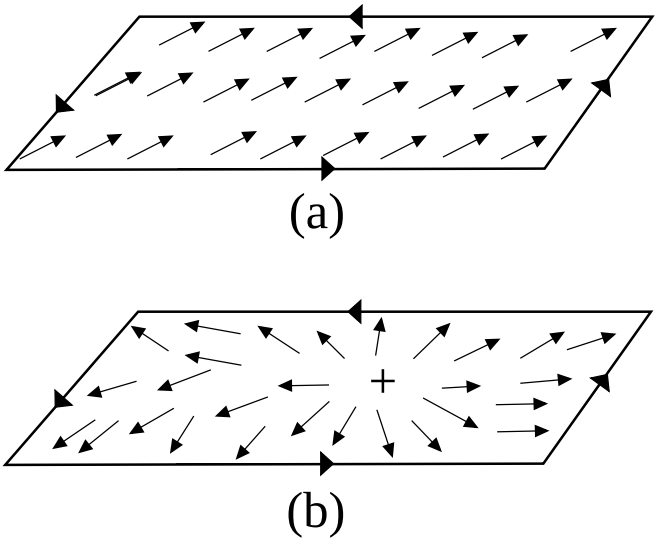

Figure 3.1: A representation of the phase fields of the photonic Bloch states in a two dimensional Brillouin zone using two component rotors. The entire set of six electric and magnetic fields is associated with a single phase at each point in the Brillouin zone. The Chern invariant simply represents the winding number of this phase along the Brillouin zone boundary and is also given by the integral of the Berry curvature $\mathcal{F}^{xy}$ over the two dimensional Brillouin zone. The phases in (a) correspond to bands with both inversion and time-reversal symmetries, and the phases of the band can be chosen to be real every where in the Brillouin zone. For bands having non-zero Chern invariants (b), the phase around the zone boundary winds by an integer multiple of 2π and there is a phase vortex-like singularity somewhere in the Brillouin zone where the Berry connection cannot be defined.

an interface, the net number of unidirectionally moving modes localized at the interface is given by the *difference* of the Chern numbers of the band at the interface. We shall consider the problem of how Chern numbers can change across an interface in the next section.

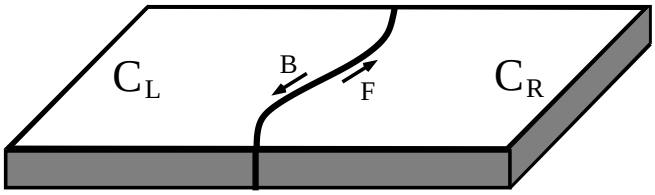

Figure 3.2: The number of forward minus the number of backward moving edgemodes equals the difference of the Chern number of the band across the interface.

Since the Chern invariant of a band is a topological number, it therefore cannot vary smoothly as we vary some parameter of the periodic eigenproblem. So long as a band remains non-degenerate, its Chern number cannot vary. However, if we tune some parameter λ of the Hamiltonian to a critical value λ_c such that two bands having non-zero Chern invariants touch at some isolated point in the Brillouin zone when $\lambda = \lambda_c$, the two bands can exchange their Chern numbers at these degenerate points; if we tuned λ beyond its critical value, the bands would emerge with different Chern invariants. Since the total Berry "magnetic flux" of all bands remains fixed always, if only two isolated bands exchange their Chern numbers at points of degeneracy, the sum of their Chern numbers must remain invariant [53].

Generically, 2D bands with both time-reversal and inversion symmetry touch at isolated points of accidental degeneracy in a linear conical fashion, forming "Dirac cones" in the vicinity of which the spectrum is determined by a massless Dirac Hamiltonian:

$$\mathcal{H} \equiv \omega - \omega_D = v_D \left(\delta k^1 \sigma_1 + \delta k^2 \sigma_2 \right), \tag{3.72}$$

where v_D, is a parameter that gives the slope of the cone close to the accidental degeneracy.

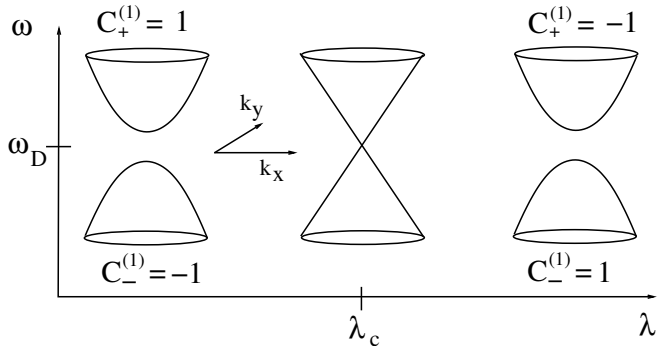

Figure 3.3: As we tune some parameter λ of the Hamiltonian across a critical point where "accidental degeneracies" occur, and two bands touch in a linear fashion forming a "Dirac point", Chern numbers of bands may be exchanged.

3.3 Broken T and I in photonics

In this section, we shall discuss our strategy for constructing photon bands with non-zero Chern invariants, and "chiral" edge states, whose existence is confirmed in the following sections.

To break time-reversal symmetry in photonics, we shall need magneto-optic materials (i.e. a Faraday rotation effect). Such materials are characterized by their ability to rotate the plane of polarization of light, when placed in a magnetic field, and are used in conventional optical isolators. The amount of rotation per length is known as a Verdet coefficient, which depends on temperature as well as on the wavelength of light. Materials known to have large Verdet coefficients ($\sim 10^0 mm^{-1}$ at wavelengths of the order of microns) are the iron garnet crystals such as $Ho_3Fe_50_{12}$ [7]. Due to the breaking of time-reversal symmetry in this materials, the eigenfrequency degeneracy is lifted for light characterized by different states of circular polarization.

While such magneto-optic devices employ magnetic fields in the direction of travel of the light beam, we shall be interested in two dimensional photonic crystals with the magnetic fields placed perpendicular to the plane of propagation of light, as shown in Fig. 3.4. We shall call the axis perpendicular to the 2D photon bands the Faraday axis, and the setup here is reminiscent of a 2D electron gas placed in a perpendicular magnetic field.

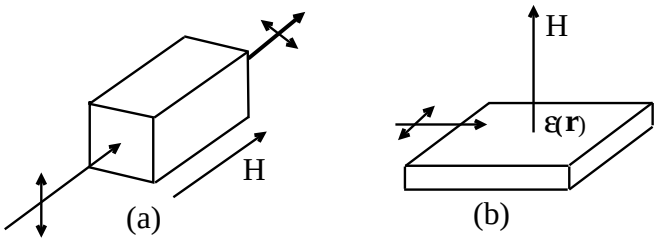

Figure 3.4: In the conventional Faraday effect used in optical isolators, light travels in the same direction as the applied field, resulting in the rotation of its polarization plane. However, in the photonic analog of a 2DEG heterojunction, light travels in the plane perpendicular to the applied field. The Faraday coupling is introduced as an imaginary, anti-symmetric component of the permittivity tensor.

Although we now have a means of introducing broken time reversal symmetry, we still need a strategy for the nucleation of equal and opposite pairs of Chern invariants on bands near points of accidental degeneracy. To do this, we choose hexagonal lattice geometry. The threefold rotation symmetry of such a system guarantees the existence of Dirac points in the Brillouin zone corners when both inversion and time-reversal symmetry are *present*; in this case the only irreducible representations of the space group of three-fold rotations correspond to non-degenerate singlets and degenerate doublets. As a simple example consider the case of free photon "bands" with dispersion $\omega = c|\boldsymbol{k}|$ in the first Brillouin zone of a triangular lattice. The eigenfrequencies of the photons are six-fold degenerate at the zone corners. Adding a weak periodic perturbation in the constitutive relations will lift the degeneracy and the bands will now be either non-degenerate or will form degenerate doublets, as demanded by the symmetry of the perturbation. Due to the 6-fold rotation symmetry, the doublets are allowed to have a linear dispersion close to the zone corners and shall be our Dirac points of interest, whereas the non-degenerate singlet bands disperse quadratically. We shall provide explicit examples of hexagonal photonic bandstructures having Dirac points in section V.

While the existence of such Dirac points are virtually guaranteed in triangular lattice systems, their *stability* has little to do with lattice geometry. Such points are stable in two dimensions only because of the presence of time-reversal symmetry and inversion symmetry,

when the eigenvalue problem is a real-symmetric one: in this case it is possible to find "accidental" degeneracies by varying just two parameters, according to the Wigner-von Neumann Theorem. Thus, if the perfect hexagonal geometry of the constitutive relations is slightly distorted, the Dirac points will simply move elsewhere in the two dimensional Brillouin zone.

If, however, inversion or time-reversal symmetry is broken in the system, the eigenvalue problem becomes complex Hermitian, and according to the Wigner-von Neumann theorem, three parameters are required to ensure stability of the Dirac points - in this case, the Dirac point degeneracy of the 2D bandstructure is immediately lifted. In both cases, the two bands which split apart each acquire a non-zero Berry curvature field $\mathcal{F}_{xy}(\boldsymbol{k})$.

If inversion symmetry alone is broken, $\mathcal{F}_{xy}(\boldsymbol{k})$ is an *odd* function of $\boldsymbol{k}$, as discussed above. While the bands do have interesting semiclassical dynamics due to their anomalous velocity, they do not have any interesting topological properties since their Chern invariants are identically zero.

On the other hand, if time-reversal symmetry alone is broken, via the Faraday coupling, the Berry curvature field will be an *even* function of $\boldsymbol{k}$, and each band which split apart due to the Faraday coupling will have equal and opposite non-zero Chern invariants.

Finally, if we can slowly tune the Faraday coupling in *space*, from a positive value, across the critical value of zero, where the local bandstructure problem would permit Dirac spectra, to a negative value, we would generate a system of photonic bands with non-zero Chern numbers, that get exchanged at the region of space corresponding to the critical zero Faraday coupling. It then follows, that modes with exact correspondence to the integer quantum Hall edge states would arise in such a system. In the following section, we shall display this explicitly using an example bandstructure.

3.4 Explicit Realization of Edge modes

An example of a photonic bandstructure with the desired properties is shown in Fig. 3.6. It consists of a triangular lattice of dielectric rods ($\epsilon_a = 14$) placed in a background of

air ($\epsilon = 1$) with a area filling ratio of $f = 0.431$. The authors of ref. [52], in a quest for optimal photonic bandgap materials, first studied this system. They computed the TE mode spectrum and found a full band gap in the TE spectrum. We have reproduced numerically their calculation and have also computed the spectrum for the TM modes.

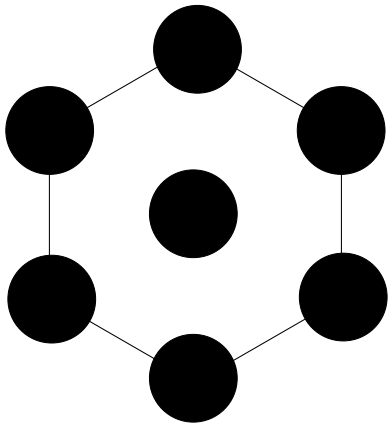

Figure 3.5: The hexagonal array of dielectric rods, as seen from above.

The key feature of this particular system which is of importance to us are the presence of a pair of Dirac points in the spectrum of the TE modes which are well isolated from both the remaining TE and TM modes. Each of the six zone corners contains the Dirac cone spectrum, but there are only two distinct Dirac points, the others being related by reciprocal lattice translations of these points. In this particular system, the two Dirac points are related by inversion in k-space.

As we have discussed, a gap immediately opens when either inversion or time-reversal symmetries are broken in this system. We break inversion symmetry in the simplest possible way by introducing a slight imbalance in the value of the dielectric tensor inside the rods about a line of inversion symmetry (in the hexagonal system, the symmetry of 3−fold rotations will also be broken along with inversion symmetry). We parameterize the inversion symmetry breaking by defining the quantity

$$m_I = \log\left(\frac{\epsilon_+}{\epsilon_-}\right), \tag{3.73}$$

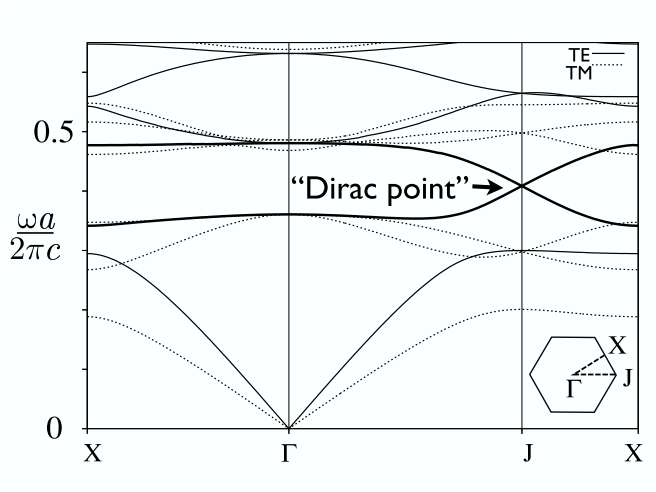

Figure 3.6: Photon bands in the $k_z = 0$ plane of a 2D hexagonal lattice of cylindrical dielectric rods. Electromagnetic waves are propagating only in the $x - y$ plane (Brillouin zone shown in the lower right). As in Ref. [52], the rods have a filling fraction $f = 0.431$, $\epsilon = 14$, and the background has $\epsilon = 1$. The band structure contains a pair of Dirac points at the zone corners (J).

where ϵ_+ and ϵ_- are the values of the permittivity inside the rods on either side of an inversion axis.

To break time-reversal symmetry, we add a Faraday effect term in the region outside the rods. This is done by giving the dielectric tensor a slight imaginary component without varying the constitutive relations inside the rods:

$$\text{outside rods: } \epsilon_{ij}^{-1}(\mathbf{x}) = \begin{pmatrix} \epsilon_b^{-1} & i\Lambda \\ -i\Lambda & \epsilon_b^{-1} \end{pmatrix}, \tag{3.74}$$

$$\text{inside rods: } \epsilon_{ij}^{-1}(\mathbf{x}) = \begin{pmatrix} \epsilon_a^{-1} & 0 \\ 0 & \epsilon_a^{-1} \end{pmatrix}. \tag{3.75}$$

We also define a parameter

$$m_T = \Lambda, \tag{3.76}$$

to define the strength of the time-reversal symmetry breaking perturbation.

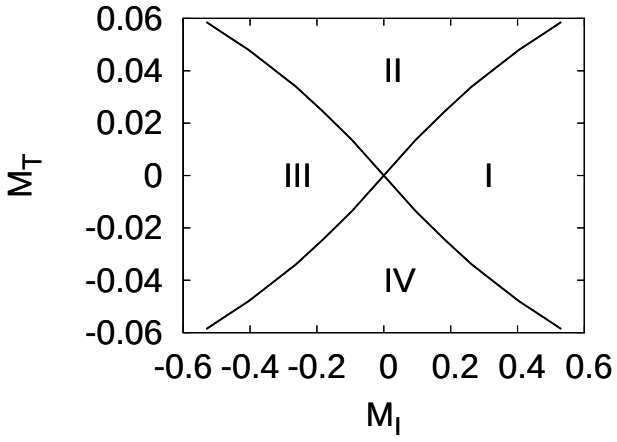

Figure 3.7: Phase diagram of the photonic system as a function of inversion and time-reversal symmetry breaking. In regions I and III, the gap openings of both Dirac points are primarily due to inversion symmetry breaking, whereas in regions II and IV, the breaking of time-reversal symmetry lifts the degeneracy of the bands which formed the Dirac point. In all four regions, the two bands of interest have non-zero Berry curvature, but only in regions II and IV do they contain non-zero Chern numbers.

We first determined the phase diagram of the system in the (m_I, m_T) plane by breaking both inversion *and* time-reversal symmetry, and locating special values of the symmetry breaking parameters that result in the closing of the bandgap at one or more Dirac points (Fig. 3.7). The phase diagram separates regions characterized by bands just below the band gap having a non-zero Chern number from regions with all bands having zero Chern numbers. The boundary between these phases are where the gap at one or more of the Dirac points vanishes, as shown in Fig. 3.7. Since there are two Dirac points, each phase boundary corresponds to the locus of parameters for which the gap at one of the Dirac points closes. Thus, both Dirac points close only when both lines intersect, namely at the point $(m_I = 0, m_T = 0)$, where both inversion and time-reversal symmetries are simultaneously present. When inversion symmetry alone is broken, the Berry curvature field of Dirac point 1 is equal in magnitude and opposite in sign of the Berry curvature at the second Dirac point. When time-reversal symmetry is broken, on the other hand, each Dirac point has an identical (both in magnitude and sign) Berry curvature field. In this case, the photon bands which split apart at the Dirac point each have Non-zero Chern number, which depends only

on the direction of the Faraday axis ($\pm\hat{z}$).

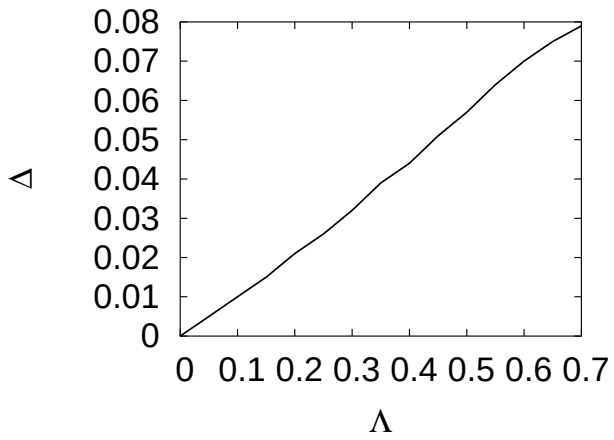

Figure 3.8: The bandgap opened by time-reversal breaking as a function of the strength of the Faraday coupling shows that the gap is linearly proportional to Λ.

We have also studied numerically the frequency gap as a function of the time-reversal breaking perturbation above and found that so long as the dielectric tensor remains positive-definite, the gap increases linearly with ϵ_{xy} (3.8). This will be important when we consider effective Dirac Hamiltonians for this problem: as we shall see, the fact that exactly at the zone corner, the gap rises linearly with M_T is consistent with the spectrum of a massive Dirac Hamiltonian with mass M_T. Thus, we have shown an example of a bandstructure which contains Dirac points whose gaps can be tuned using time-reversal and inversion symmetry breaking perturbations. We can now show the existence of "chiral" edge states in this system.

To study edge states in this system, we introduce a "domain wall" configuration across which the Faraday axis reverses. As we shall now show numerically, (and justify analytically in the following section), the edge modes that occur along the domain wall are bound states that decay exponentially away from the wall while propagating freely in the direction parallel to the interface. In order to study the exponential decay of these modes, we glue together N copies of a single hexagonal unit cell along a single lattice translation direction $\boldsymbol{R}_\perp$, which shall be the direction perpendicular to the domain wall. We treat this composite cell as

a unit cell with periodic boundary conditions. Since a domain corresponds to a certain direction of the Faraday axis, we study a configuration here in which the axis changes direction abruptly across the domain wall from the $+\hat{z}$ to the $-\hat{z}$ direction.

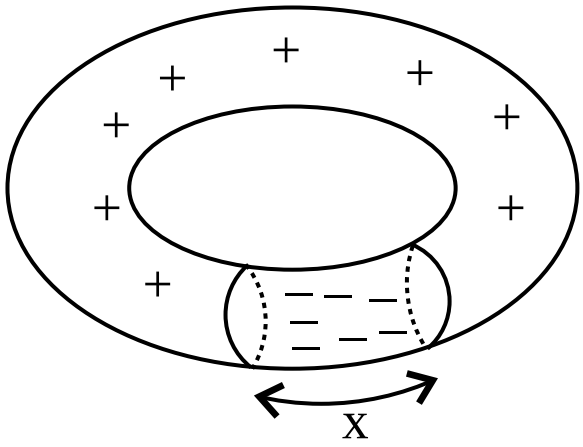

Figure 3.9: In a system with periodic boundary conditions, there are necessarily two domain walls separating regions with different faraday axes. We study the gap of the spectrum at the (now non-degenerate) Dirac points as a function of the distance $\boldsymbol{x}$ between the two walls.

When we consider the spectrum on a torus, there are necessarily two domain walls. Furthermore, since many unit cells are copied in this system, there are as many duplicates of the bands in the enlarged system under consideration. We study the bandgap precisely at the Dirac point as a function of the fractional distance between the two domain walls on the torus x (Fig. 3.9) for a composite unit cell consisting of $N = 30$ unit cells copied along the $\boldsymbol{R}_\perp$ direction. When $x = 0$ or $x = 1$, the two domain walls are at the same point, and this corresponds to a single domain with a single Faraday coupling Λ. For all other values of x, the "unit cell" comprises a two domain system with non-equivalent lengths. In Fig. 3.10, the gap between the two bands closest to the Dirac frequency decays exponentially as a function of the distance between the two domain walls. We shall show that the exponential decay in the gap corresponds to the localization of the edge modes along each domain wall. The small gap at intermediate values of x, when the two walls are far apart corresponds to the fact that each edge mode has a small amplitude, and therefore hardly mix with each

other at those length scales.

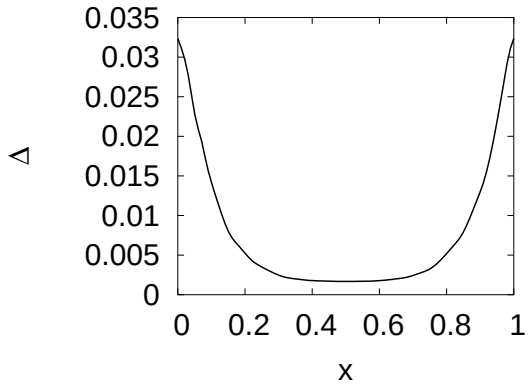

Figure 3.10: The spectral gap between the two bands which split apart due to the breaking of time-reversal symmetry. The spectrum is computed on a torus for the extended system consisting of 30 copies of the hexagonal unit cell. Furthermore, domain walls, across which the sign of the Faraday axis flips are introduced, and the spectrum is plotted as a function of the separation $\boldsymbol{x}$ between the walls (see also Fig. 3.9).

When the domain wall is introduced, translational symmetry is still preserved along the direction parallel to the wall, and the states of the composite system of 30 unit cells can be labeled by $\boldsymbol{k}_{\|}$, the Bloch vector in the direction parallel to the wall. Figures 3.11, 3.12,and 3.13 consist of a spectral series of a system without any broken time-reversal symmetry (Fig. 3.11), with uniformly broken time-reversal symmetry (Fig 3.12), and a domain wall configuration (Fig. 3.13) for the 30 unit cell composite system. The bands are plotted along a trajectory in $\boldsymbol{k}$-space in the $\boldsymbol{k}_{\|}$ direction which contains the two distinct Brillouin zone corners. It is clear that in the domain wall, there are two additional modes formed in the band gap that arose from the Faraday coupling. Since the domain walls are duplicated on the torus, the spectrum of edge modes will also be doubled; in Fig. 3.13, only the two non-equivalent modes are shown. Each mode in the band gap has a free photon linear dispersion along the direction of the wall; moreover, both have positive group velocities, and therefore propagate *unidirectionally*.

To be certain, however, that these "chiral" modes are indeed localized near the interface, we have numerically computed $\langle u(\boldsymbol{r})|\boldsymbol{B}^{-1}|u(\boldsymbol{r})\rangle$, the electromagnetic energy density (the $\boldsymbol{B}$

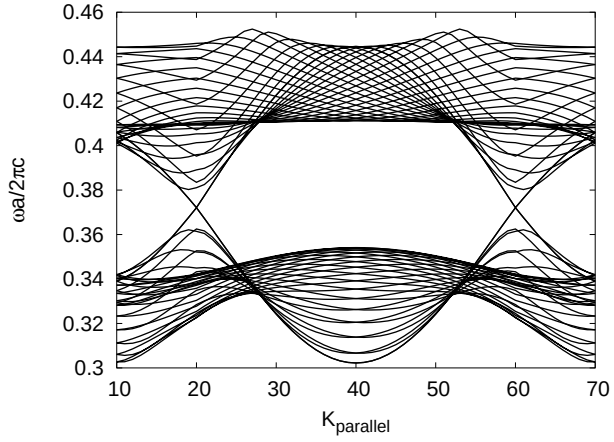

Figure 3.11: The spectrum of the composite system consisting 30 copies of a single hexagonal unit cell duplicated along a direction $\boldsymbol{R}_{\perp}$. Both inversion and time-reversal symmetries are present, and the Dirac points are clearly visible. While the composite system has a spectrum containing many bands, only two bands touch at the Dirac point. The dispersion is computed in $\boldsymbol{k}$ space along the direction *parallel* to the wall.

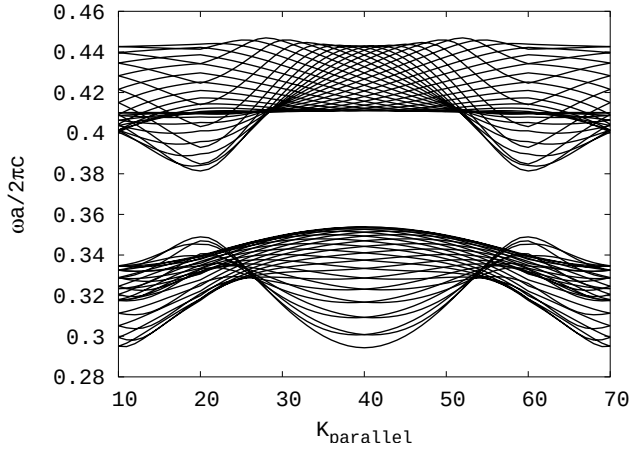

Figure 3.12: The same system as above, but with broken time-reversal symmetry without a domain wall. There is a single Faraday axis in the rods of the entire system.

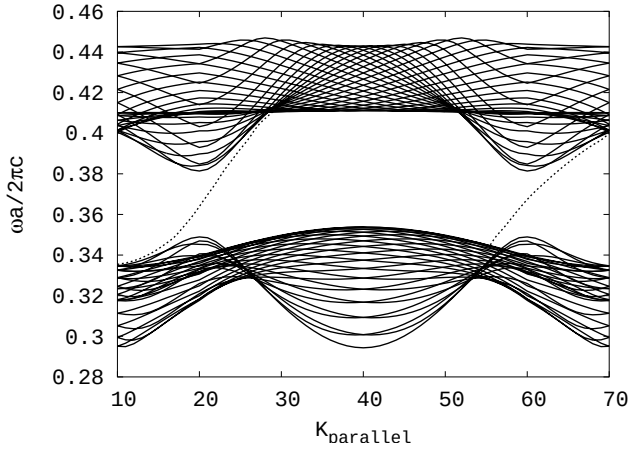

Figure 3.13: Same system as above, but with a domain wall introduced corresponding to maximum separation of the walls on the torus. The two additional modes present in the gap correspond to edge modes with a "free photon" linear dispersion along the wall. There are two modes, since across the domain wall, the Chern number of the band just below the band gap changes by 2.

matrix, defined in section II, is not to be confused with the magnetic flux density), the photon probability density in real space. We have computed this quantity along with all the spectra of the composite system using the real space bandstructure algorithms described in the following chapter. As shown in Fig. 3.14, the energy density is a gaussian function, peaked at the position of the domain wall, decaying exponentially away from the wall. From this calculation, we extract a localization also approximately 5 unit translations in the direction perpendicular to the interface.

We have therefore shown here using explicit numerical examples that photonic analogs of the "chiral" edge states of the integer quantum Hall effect can exist along domain walls of hexagonal photonic systems with broken time-reversal symmetry. We have studied the unphysical case in which such domain walls are abrupt changes in the axis of the Faraday coupling. However, due to the topological nature of these modes, a smoother domain wall in which the Faraday axis slowly reverses over a length scale much larger than a unit cell dimension would also produce such modes. The most important requirement for the existence of these modes, is that at some spatial location, the Faraday coupling is

tuned across its critical value. How this particular tuning is effected is irrelevant. In the following section, after deriving the effective Hamiltonians for these modes, we shall consider a smoothly varying Faraday coupling, which corresponds to an exactly soluble system, and shall show the evolution of these modes as the smoothness of the Faraday coupling is varied towards the step function limit considered here.

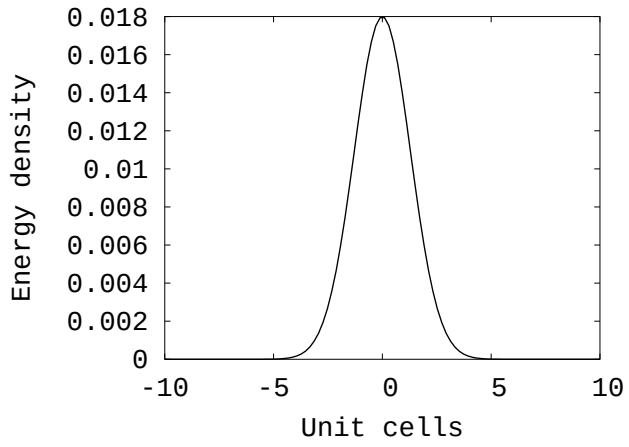

Figure 3.14: The real-space electromagnetic energy density profile associated with the edge modes in Fig. 3.13 plotted as a function of the direction *perpendicular* to the domain wall (and "integrated" over the direction parallel to the interface) and fit to a gaussian profile. The integrated energy density depicted here plays the role of the photon probability density which confirms that light is confined to the interface.

3.5 Model Hamiltonian Approach

The crucial feature exploited in the previous sections was the possibility of tuning bandgaps at Dirac points by adding time-reversal breaking perturbations. Before adding these perturbations, the linear conical spectrum at these Dirac points are governed by two dimensional massless Dirac Hamiltonians, and time-reversal or inversion symmetry breaking perturbations contribute *mass terms* to the Hamiltonian. In this section, we shall construct these Dirac Hamiltonians starting from the Maxwell equations for two dimensional photonic systems with hexagonal symmetry.

To motivate a discussion of Dirac Hamiltonians in photonic systems, we begin this

section by considering a "nearly-free photon" approach in which a two dimensional "free photon" spectrum consisting of plane waves is perturbed by a weak periodic and hexagonal modulation of $\epsilon(\boldsymbol{r})$. Due to the underlying symmetry of the perturbation, the plane waves mix in a manner to generate Dirac points in the zone corners of this system. We then consider the effect adding time-reversal and inversion symmetry breaking perturbations in this system and derive an expression for the Dirac mass. We then revert back to our photon band problem and derive expressions for the Dirac mass in these systems.

In analogy with the "nearly-free electron" approximation, we consider the photon propagation problem in the weak-coupling regime, in which the dielectric properties of the medium act as a weak perturbation. We solve the Maxwell normal mode problem for Bloch state solutions, and work out corrections to the free photon dispersion relations in the Brillouin zone boundaries. We shall assume continuous translational invariance in the z-direction, and study the propagation of electromagnetic waves in the x-y plane.

The free photon constitutive relations are isotropic and uniform in the plane:

$$B_0 = \begin{pmatrix} \epsilon_0 & 0 \\ 0 & \mu_0 \end{pmatrix}. \tag{3.77}$$

We consider the "free photon bands" in the first hexagonal Brillouin zone depicted in Fig. 3.15. Let $\boldsymbol{G}_i$, $i = 1, 2, 3$ be the three equal-length reciprocal lattice vectors each rotated 120^0 with respect to one another. The hexagonal zone corners correspond to the points $\pm\boldsymbol{K}_i$, where $\boldsymbol{K}_1 = (\boldsymbol{G}_2 - \boldsymbol{G}_3)/3$, etc., and $|\boldsymbol{K}| = |G|/\sqrt{3}$. At each of the zone corners, the free-photon spectrum is six-fold degenerate with $\omega_0 = c_0 K$. In two dimensions, the modes decouple into TE (E_x, E_y, H_z), and TM (H_x, H_y, E_z) sets, and we shall focus only on the TE modes and consider the 3-fold TE mode symmetry at the zone corners (the TE and TM modes do not mix in 2 dimensions). The eigenvalue equation for the free photon plane wave modes at the zone corners is $\boldsymbol{A}|\boldsymbol{u}_0\rangle = \omega_0 \boldsymbol{B}_0^{-1}|\boldsymbol{u}_0\rangle$, or equivalently, $\boldsymbol{B}_0^{1/2}\boldsymbol{A}\boldsymbol{B}_0^{1/2}|\boldsymbol{z}_0\rangle = \omega_0|\boldsymbol{z}_0\rangle$ and the states $|\boldsymbol{z}_0\rangle = \boldsymbol{B}_0^{-1/2}|\boldsymbol{u}_0\rangle$ satisfy $\langle \boldsymbol{z}_0^{(\lambda)}|\boldsymbol{z}_0^{(\lambda')}\rangle = \delta_{\lambda\lambda'}$.

Next, keeping the uniform isotropic permeability fixed, we add a weak periodic perturbation to the permittivity of the form

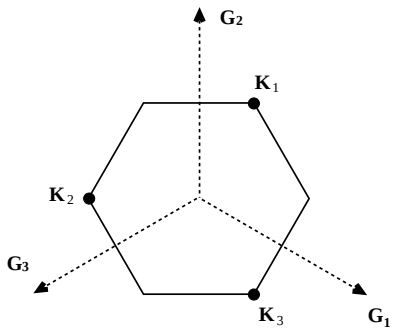

Figure 3.15: In the weak coupling approach, the free photon TE mode plane waves are perturbed by a periodic modulation in the permittivity. The plane wave frequency at the three equivalent zone corners ($\boldsymbol{K}_i$, i=1,2,3) is lifted by the permittivity in "$\boldsymbol{k}\cdot\boldsymbol{p}$" perturbation theory into a non-degenerate singlet and a degenerate doublet.

$$\lambda B_1^{-1} = \begin{pmatrix} \epsilon_0 \lambda V_G(\boldsymbol{r}) & 0 \\ 0 & 0 \end{pmatrix}, \tag{3.78}$$

with

$$V_G(\boldsymbol{r}) = 2\sum_{n=1}^{3} \cos\left(\boldsymbol{G}_n \cdot \boldsymbol{r}\right). \tag{3.79}$$

After this perturbation is added, the TE and TM modes no longer remain degenerate; while the TM modes remain 3-fold degenerate at the zone corners at the frequency $\omega = c_0|\boldsymbol{K}|$, the TE modes split apart into a singlet and a degenerate doublet. We now determine the splitting to leading order in λ with within a weak-coupling "nearly-free photon" approach.

With the periodic perturbation, the eigenvalue problem is

$$\boldsymbol{A}|\boldsymbol{u}\rangle = \omega\left(\boldsymbol{B}_0^{-1} + \lambda \boldsymbol{B}_1^{-1}\right)|\boldsymbol{u}\rangle, \tag{3.80}$$

which is equivalent to

$$\boldsymbol{B}_0^{1/2}\left(\boldsymbol{A} - \lambda\omega\boldsymbol{B}_1^{-1}\right)\boldsymbol{B}_0^{1/2}|\boldsymbol{z}\rangle = (\omega_0 + \delta\omega)\,|\boldsymbol{z}\rangle. \tag{3.81}$$

The energy splittings are worked out in degenerate perturbation theory (see subsection 3.5.1) as

$$\begin{aligned}\frac{\delta\omega_n}{\omega_0} &= -\lambda\langle\tilde{\boldsymbol{z}}_n|\boldsymbol{B}_0^{1/2}\boldsymbol{B}_1^{-1}\boldsymbol{B}_0^{1/2}|\tilde{\boldsymbol{z}}_n\rangle \\ &= -\lambda\langle\tilde{\boldsymbol{u}}_n|\boldsymbol{B}_1^{-1}|\tilde{\boldsymbol{u}}_n\rangle,\end{aligned}$$

where $|\tilde{\boldsymbol{z}}_n\rangle$ are appropriate combinations of the three free photon plane-plane waves that diagonalizes the periodic potential. These states are obtained by requiring them to be invariant under 3-fold rotations in the plane. Instead of writing the fields in the coordinate basis, it is convenient to use a redundant basis of the three vectors $(e^{i\boldsymbol{K}_1\cdot\boldsymbol{r}}, e^{i\boldsymbol{K}_2\cdot\boldsymbol{r}}, e^{i\boldsymbol{K}_3\cdot\boldsymbol{r}})$, with $\sum_n \boldsymbol{K}_n = 0$, and $\boldsymbol{K}_i \cdot \boldsymbol{K}_j = -K^2/2, i \neq j$. In this basis, the magnetic field of the TE modes is written as ($\eta = e^{2\pi i/3}$):

$$H_1^z = (1, 1, 1)\,, \tag{3.82}$$

$$H_2^z = (1, \eta^*, \eta)\,, \tag{3.83}$$

and

$$H_3^z = (1, \eta, \eta^*)\,. \tag{3.84}$$

The corresponding electric flux densities are easily obtained:

$$D_1^{\parallel} = \frac{1}{\omega}\left(\hat{z}\times\boldsymbol{K}_1, \hat{z}\times\boldsymbol{K}_2, \hat{z}\times\boldsymbol{K}_3\right), \tag{3.85}$$

$$D_2^{\parallel} = \frac{1}{\omega}\left(\hat{z}\times\boldsymbol{K}_1, \eta^*\hat{z}\times\boldsymbol{K}_2, \eta\hat{z}\times\boldsymbol{K}_3\right), \tag{3.86}$$

$$D_3^{\parallel} = \frac{1}{\omega}\left(\hat{z}\times\boldsymbol{K}_1, \eta\hat{z}\times\boldsymbol{K}_2, \eta^*\hat{z}\times\boldsymbol{K}_3\right), \tag{3.87}$$

and

$$|\tilde{\boldsymbol{z}}_i\rangle = \begin{pmatrix} E_i^{\parallel} \\ H_i^z \end{pmatrix}. \tag{3.88}$$

Clearly, these are the plane wave solutions that satisfy Maxwell equations and transform appropriately under 3-fold rotations in the plane. We are therefore led to the simple result that the splitting at the zone corners due to the mixing of the three plane waves is related to the integral over the unit-cell of the electric fields and the periodic potential, which is a traceless, real-symmetric 3×3 problem. It is easy to see that the problem is traceless because diagonal terms of the form $\langle u_i|B_1|u_i\rangle$ vanish identically since u_i are plane waves.

To leading order in λ, the three photon bands split to form a singlet band at frequency $\omega_0 = c_0|K|\left(1 + \lambda/2 + O(\lambda^2)\right)$ and a degenerate doublet at frequency

$$\omega_D = c_0|K|\left(1 - \lambda/4 + O(\lambda^2)\right). \tag{3.89}$$

Exactly at the zone corners, the singlet and doublet states above diagonalize the perturbation in Eq.(3.78). To leading order in λ and $\delta\boldsymbol{k} \equiv \boldsymbol{k} - \boldsymbol{K}_i$, the deviation in the Bloch vector from the zone corners, the states $|\tilde{\boldsymbol{z}}_2(\delta\boldsymbol{k})\rangle$ and $|\tilde{\boldsymbol{z}}_3(\delta\boldsymbol{k})\rangle$, (where $|\tilde{\boldsymbol{z}}_i(\delta\boldsymbol{k})\rangle = \exp(i\delta\boldsymbol{k}\cdot\boldsymbol{r})|\tilde{\boldsymbol{z}}_i\rangle$), which are degenerate at $\delta\boldsymbol{k} = 0$ mix and split apart linearly as a function of $|\delta\boldsymbol{k}|$, forming a "Dirac point". To leading order, the Dirac point doublet does not mix with the singlet state $|\tilde{\boldsymbol{z}}_1(\delta\boldsymbol{k})\rangle$. The effective Hamiltonian governing the spectrum of the doublet, to leading order in $\delta\boldsymbol{k}$ is a 2D massless Dirac equation:

$$\omega_\pm(\delta\boldsymbol{k}) = \omega_D \pm v_D\left(\delta k_x \sigma^x + \delta k_y \sigma^y\right), \tag{3.90}$$

where $v_D = c_0/2 + O(\lambda)$, and σ^i are the Pauli matrices written in the subspace of the doublet states. The linear dispersion of the doublet in the neighborhood of the zone corners is immediately obtained by solving Eq.(3.90):

$$\omega = \omega_D \pm v_D|\delta\boldsymbol{k}|. \tag{3.91}$$

The frequency of the singlet band remains unchanged to leading order in $\delta\boldsymbol{k}$: $\omega_0(\delta\boldsymbol{k}) = \omega_0 + O(|\delta\boldsymbol{k}|^2)$. Thus, we have shown that the periodic modulation of the permittivity having 3-fold rotational symmetry gives rise to a quadratically dispersing singlet band and a "Dirac point" with linear dispersion.

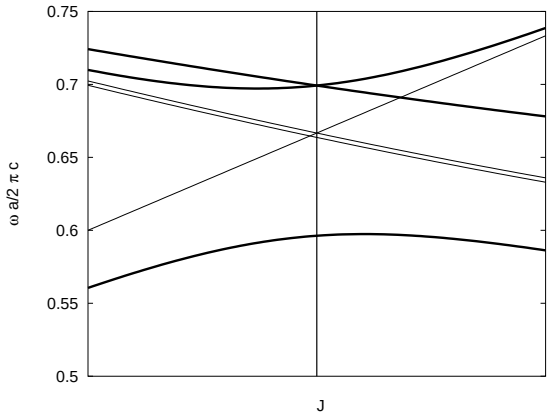

Figure 3.16: Spectrum of photon dispersion in the vicinity of the zone corners. We have arbitrarily set $\lambda < 0$ so that the singlet band has a lower frequency than the Doublet. Free photon spectra are given by dashed lines. Away from the zone corners, the free spectrum is not affected to leading order in λ.

Next, we add a Faraday term, with an axis normal to the xy-plane, to the permittivity tensor $\epsilon^{xy} = -\epsilon^{yx} = i\epsilon_0\eta(\boldsymbol{r}, \omega)$, where

$$\eta(\boldsymbol{r}, \omega) = \eta_0(\omega) + \eta_1(\omega)V_G(\boldsymbol{r}). \tag{3.92}$$

Both $\eta_0(\omega)$ and $\eta_1(\omega)$ are odd functions of ω. In the limit that the Faraday coupling is much weaker in strength than the periodic modulation, $|\eta_0|$, $|\eta_1| \ll |\lambda| \ll 1$, the mixing between the non-degenerate singlet state and the doublet remains negligible, and the energy of the singlet state is unaffected by the Faraday perturbation. However, the doublet states split apart at the Dirac point. Using the expression for the Dirac point splitting, derived in subsection 3.5.1, we find that the splitting of the doublet at the zone corner is given by

$$\omega_\pm - \omega_D = \pm v_D\kappa, \quad \kappa = |K|\left(\frac{3}{2}\eta_1(\omega_D) - 3\lambda\eta_0(\omega_D)\right). \tag{3.93}$$

Away from the Dirac point (but still close enough to the zone corners so that the "nearly-free photon" approximation for the three plane wave states remains valid), the doublet bands acquire a dispersion

$$\omega = \omega_D \pm v_D\left(|\delta\boldsymbol{k}|^2 + \kappa^2\right)^{1/2}, \tag{3.94}$$

which is the spectrum of a 2D massive Dirac Hamiltonian:

$$\omega_{\pm}(\delta\boldsymbol{k}) = \omega_D \pm v_D \left(\delta k_x \sigma^x + \delta k_y \sigma^y + \kappa\sigma^z\right). \tag{3.95}$$

The Dirac points that occur in the "nearly-free photon" approximation are not isolated points of degeneracy, since, away from the zone corners, the two bands which formed the Dirac point merge together to resume their original free-photon form. Consequently, the type of modes studied in the previous section cannot be reproduced using this type of weak-coupling expansion.

However, we can gain understanding by suppose that we have the exact solutions of the electromagnetic Bloch states and eigenfrequencies of a system containing isolated Dirac points, such as the one studied numerically in section IV. We can use precisely the same weak Faraday coupling approximation to work out the splitting of the Dirac point with a Faraday term. Assuming we are given example photonic bandstructures of long hexagonal systems with $k_z = 0$, which contain only isolated Dirac points, a weak Faraday coupling would split apart the bands that formed the Dirac point, and the splitting is identical to that in (3.94). Suppose that the two bands having a Dirac point, otherwise form a PBG with a gap $\Delta \gg v_D\kappa$ (as in the case of the numerical example given in the previous section). In this case, since the Faraday term removes all points of degeneracy, the now non-degenerate bands have a well-defined Berry curvature field

$$\mathcal{F}_{\pm}(\delta\boldsymbol{k}) = \pm\frac{1}{2}\kappa\left(|\delta\boldsymbol{k}|^2 + \kappa^2\right)^{-3/2}, \tag{3.96}$$

which decays rapidly away from the Dirac point, and contributes a total integrated Berry curvature of $\pm\pi$. Since there are two non-equivalent Dirac points in the hexagonal geometry under consideration, the net Berry curvature of the system is the sum of the contributions from each Dirac point. If, as in the case under consideration, spatial inversion symmetry is preserved, but time-reversal symmetry is broken, the Berry curvature fields at each Dirac point of a given band add, giving total Chern numbers ± 1 for each of the split bands. However, if time-reversal symmetry were preserved, and inversion symmetry breaking caused

the gap to open, the Berry curvature field of each Dirac point for a given band are equal in magnitude but opposite in sign, and the Chern number would vanish.

As before, to get unidirectional edge modes of light in this system, the Faraday coupling must be tuned across its critical value $\eta(\boldsymbol{r},\omega) = 0$. To do this, we consider a Faraday coupling that varies slowly and adiabatically in space, we shall assume negligible frequency dependence of the Faraday coupling, and we shall parameterize the local value of the Faraday coupling by a smoothly varying function $\kappa(\boldsymbol{r})$, which is positive in some regions and negative in other regions of the 2D plane perpendicular to the cylindrical axis of the hexagonal array of rods. Due to the adiabatic variation of $\kappa(\boldsymbol{r})$, each point in space is characterized by a local bandstructure problem, and the splitting at the Dirac point is given again by the expression in (3.94), but with the local value of κ. In this limit, the smooth variation of $\kappa(\boldsymbol{r})$ leads to a 2D Dirac Hamiltonian with a adiabatically spatially varying mass gap. At all points where $\kappa(\boldsymbol{r}) = 0$, the local bandstructure in the vicinity of the Dirac point is the massless 2D Dirac Hamiltonian; provided that $|\kappa(\boldsymbol{r})| \ll \Delta$, the PBG, the spectrum far away from the Dirac points is unaffected by $\kappa(\boldsymbol{r})$. In what follows, we assume that when $\kappa = 0$, our bandstructure contains Dirac points which are formed by two isolated bands in a PBG region having no other points of degeneracy.

We neglect the mixing between modes at different Dirac points, and consider the situation in which $\kappa(\boldsymbol{r})$ vanishes along a single line ($x = 0$ for instance), and we assume translational invariance along the direction parallel to the interface ($y-$direction). As before, we consider the degenerate perturbation problem of the normal modes close to the Dirac point. Now, however, the coefficients of the degenerate solutions of the Maxwell equations are spatially varying quantities. Let $|u_\sigma(\pm\boldsymbol{k}_D)\rangle$, $\sigma = \pm$, be the degenerate solutions (i.e. the periodic parts of the photon Bloch state wave functions) at a pair of Dirac points when $\kappa = 0$. With the local variation, we take spatially varying linear combination of these Bloch states

$$u(\boldsymbol{k}_D, \boldsymbol{r}) = \sum_{\sigma,\pm} \psi_\sigma(\boldsymbol{r}) \exp\left(\pm i\boldsymbol{k}_D \cdot \boldsymbol{r}\right) u_\sigma(\pm\boldsymbol{k}_D, \boldsymbol{r}), \tag{3.97}$$

and arrive at the fact that the local value of the splitting of the two bands at $\boldsymbol{k}_D$ is

$$\omega_+(\boldsymbol{k}_D) - \omega_-(\boldsymbol{k}_D) = 2\kappa(\boldsymbol{r}). \tag{3.98}$$

In the neighborhood of the Dirac point, the degenerate perturbation problem gives us a 2D massive Dirac Hamiltonian, with δk_x replaced by the operator $-i\nabla_x$ in the position representation, since translation symmetry in the x-direction is broken by $\kappa(x)$. We thus obtain an expression of the form $v_D\hat{K}|\psi\rangle = \delta\omega|\psi\rangle$, and

$$\hat{K} = -i\boldsymbol{\sigma}^x\nabla_x + \delta k_\parallel \boldsymbol{\sigma}^y + \kappa(x)\boldsymbol{\sigma}^z. \tag{3.99}$$

The Bloch vector in the y-direction, which remains conserved due to the preservation of translation invariance along this direction, is $k_{Dy} + \delta k_\parallel$.

For the particular choice of $\kappa(x) = \kappa^\infty \tanh(x/\xi)$, $\xi > 0$, (where κ^∞ is the asymptotic value of the Dirac point splitting at distances $\gg \xi$ from the interface), the problem is exactly solvable, since the Dirac Hamiltonian $\hat{K}$, when squared, becomes a 1D Schrödinger Hamiltonian $\hat{K}^2$ corresponding to the integrable Poschl-Teller Hamiltonian [30].

To see how this comes about, we explicitly work out the operator $\hat{K}^2$, making use of the anti-commuting property of the Pauli matrices $\{\sigma^a, \sigma^b\} = 2\delta^{ab}$:

$$\hat{K}^2 - \delta k_\parallel^2 = -\nabla_x^2 + \kappa(x)^2 - \boldsymbol{\sigma}^y\kappa'. \tag{3.100}$$

The spatially varying Dirac mass term that changed sign across the interface becomes a "potential well" with bound states given by[30]

$$\omega_0(\delta k_\parallel) = \omega_D + s_\kappa v_D \delta k_\parallel, \quad s_\kappa = sgn(\kappa^\infty) \tag{3.101}$$

$$\omega_{n\pm} = \omega_D \pm v_D\left(\delta k_\parallel^2 + \kappa_n^2\right)^{1/2}, \quad n > 0. \tag{3.102}$$

where $|\kappa_n = 2n|\kappa^\infty|/\xi$, $n < |\kappa^\infty\xi/2$. In the $n = 0$ mode, light propagates unidirectionally, with velocity v_D, in the direction parallel to the wall. All other bound modes are bidirectional modes. The numerical example of a Dirac mass studied in the previous section that changed sign abruptly, as a step function, has the 1D Schrodinger problem in an attractive

delta function potential as its square. Consequently, as we have seen, the model permitted for only a single bound state, corresponding to the unidirectional mode.

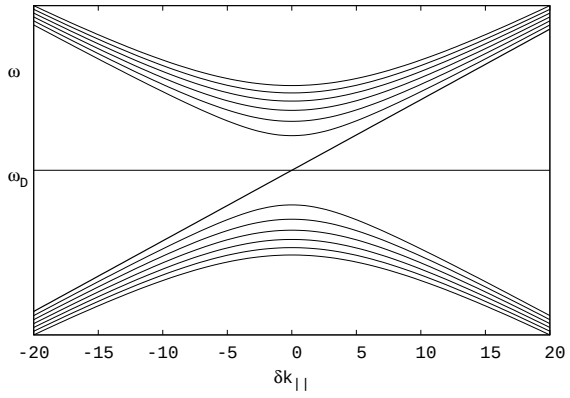

Figure 3.17: Spectrum of the integrable Poschl-Teller model. With the exception of the zero mode, all bound states correspond to bi-directionally propagating modes localized at the interface where the function $\kappa(\boldsymbol{r}) = 0$. The zero mode, on the other hand, is unbalanced, and furthermore, it corresponds to unidirectional propagation.

For the generic case, the second order differential equation for the $n > 0$ bound states can not be solved analytically. However, a formal solution for the zero mode eigenfrequency can be obtained, as it is obtained by solving a *first order* equation, as we now discuss. Starting from the Dirac equation for the more general case

$$v_D \left(-i\boldsymbol{\sigma}^x \nabla_x + -i\boldsymbol{\sigma}^y \nabla^y + \kappa(x)\boldsymbol{\sigma}^z\right) |\psi_\pm\rangle = \delta\omega |\psi_\pm\rangle, \tag{3.103}$$

by definition, the "zero mode" has the free photon dispersion along the direction parallel to the wall, which implies that the function $|\psi\rangle \propto \exp(i\delta k_\parallel y)$. We are thus left with the equation

$$\left(-i\boldsymbol{\sigma}^x \nabla_x + \kappa(x)\boldsymbol{\sigma}^z\right) |\psi_\pm\rangle = 0. \tag{3.104}$$

Multiplying both sides with $\boldsymbol{\sigma}^x$, we arrive at the following first order differential equation :

$$\left(\nabla_x + \kappa(x)\boldsymbol{\sigma}^y\right) = 0, \tag{3.105}$$

which has as its formal solution

$$|\psi_\pm\rangle = \exp\left(i\delta k_\parallel y + \alpha \int^x dx' \kappa(x')\right) |\phi_\pm(\alpha)\rangle, \tag{3.106}$$

where $\boldsymbol{\sigma}^y|\phi_\pm(\alpha)\rangle = \alpha|\phi_\pm(\alpha)\rangle$. Although there are formally two solutions for the zero mode, corresponding to $\alpha = \pm 1$, only one can occur; the other is not normalizable and thus cannot represent a physically observable state.

3.5.1 Derivation of the Dirac Point Splitting

In this section, we derive a general expression for the frequency splitting at the Dirac point caused by inversion or time-reversal symmetry breaking perturbations. We will use "Bra-ket" notation to represent our eigenvectors instead of writing equations for each component. We suppose that we know the exact eigenstates of the problem

$$\boldsymbol{A}|\boldsymbol{u}_0\rangle = \omega_D \boldsymbol{B}_0^{-1}|\boldsymbol{u}_0\rangle, \tag{3.107}$$

and that the solutions are two fold degenerate at the Dirac point, as for example, in the numerical examples we have considered. Now add a perturbation in the constitutive relations:

$$\boldsymbol{B}^{-1} = \boldsymbol{B}_0^{-1} + \lambda \boldsymbol{B}_1^{-1}. \tag{3.108}$$

This term represents our inversion or time-reversal breaking perturbation. To find the splitting of the Dirac point (our "Dirac mass"), we solve the modified problem

$$\boldsymbol{A}|\boldsymbol{u}\rangle = \omega \left(\boldsymbol{B}_0^{-1} + \lambda \boldsymbol{B}_1^{-1}\right)|\boldsymbol{u}\rangle. \tag{3.109}$$

Since the $\boldsymbol{B}_0^{-1}$ matrix is positive-definite, it has a well defined positive-definite inverse square root matrix $\boldsymbol{B}_0^{1/2}$, and we can rewrite the unperturbed problem in the form of a conventional Hermitian eigenvalue problem

$$\boldsymbol{B}_0^{1/2}\boldsymbol{A}\boldsymbol{B}_0^{1/2}|\boldsymbol{z}_0\rangle = \omega_D|\boldsymbol{z}_0\rangle, \tag{3.110}$$

where

$$|\boldsymbol{z}_0\rangle = \boldsymbol{B}_0^{-1/2}|\boldsymbol{u}_0\rangle. \tag{3.111}$$

The new eigenvalue problem with the symmetry breaking terms is

$$\begin{aligned} \boldsymbol{A}|\boldsymbol{u}\rangle &= \omega \left(\boldsymbol{B}_0^{-1} + \lambda \boldsymbol{B}_1^{-1}\right)|\boldsymbol{u}\rangle \\ &= \omega \boldsymbol{B}_0^{-1/2}\left(1 + \lambda \boldsymbol{B}_0^{1/2}\boldsymbol{B}_1^{-1}\boldsymbol{B}_0^{1/2}\right)\boldsymbol{B}_0^{-1/2}|\boldsymbol{u}\rangle, \end{aligned}$$

which subsequently is rewritten in the canonical form as

$$\boldsymbol{B}_0^{1/2}\left(\boldsymbol{A}-\lambda\omega\boldsymbol{B}_1^{-1}\right)\boldsymbol{B}_0^{1/2}|\boldsymbol{z}\rangle=\omega|\boldsymbol{z}\rangle, \tag{3.112}$$

where $|\boldsymbol{z}\rangle=\boldsymbol{B}_0^{-1/2}|\boldsymbol{u}\rangle$. The correction to the spectrum to first order in perturbation theory in the eigenvalue problem above is then

$$\begin{aligned}\delta\omega &= -\omega_D\lambda\langle\boldsymbol{z}_0|\boldsymbol{B}_0^{1/2}\boldsymbol{B}_1^{-1}\boldsymbol{B}_0^{1/2}|\boldsymbol{z}_0\rangle\\ &= -\omega_D\lambda\frac{\langle\boldsymbol{u}_0|\boldsymbol{B}_1^{-1}|\boldsymbol{u}_0\rangle}{\langle\boldsymbol{u}_0|\boldsymbol{B}_0^{-1}|\boldsymbol{u}_0\rangle}.\end{aligned}$$

We have restored the normalization factor for the state $|\boldsymbol{u}_0\rangle$ in the last line above. Thus, our main result here is a general expression for the splitting of the Dirac point frequency spectrum, given by the dimensionless quantity

$$\frac{\delta\omega}{\omega_D}=-\lambda\frac{\langle\boldsymbol{u}_0|\boldsymbol{B}_1^{-1}|\boldsymbol{u}_0\rangle}{\langle\boldsymbol{u}_0|\boldsymbol{B}_0^{-1}|\boldsymbol{u}_0\rangle}. \tag{3.113}$$

3.6 Semiclassical Analysis

Now let the "Dirac mass" term that opens the photonic band gap be a slowly varying function $\kappa(x)$ that changes monotonically (and analytically) from $-k_0$ at $x=-\infty$ to k_0 at $x=+\infty$. The photonic spectrum of modes with wavenumbers $\boldsymbol{k}=\boldsymbol{k}_D+\delta\boldsymbol{k}$ near the "Dirac point" $\boldsymbol{k}_D$, and which become doubly-degenerate at $\boldsymbol{k}_D$, is an adiabatic function of x:

$$\begin{aligned}\omega(x,\delta k_x,\delta k_y) &= \omega_D\pm v_D\left(\delta k_y^2+k(x,\delta k_x)^2\right)^{1/2},\\ k(x,\delta k_x)^2 &= \delta k_x^2+\kappa(x)^2,\end{aligned} \tag{3.114}$$

where $v_D>0$ is the "Dirac speed". For $k(x,\delta k_x)^2<k_0^2$, the modes are evanescent as $x\to\pm\infty$, so are localized on the wall. In the $x-\delta k_x$ plane, the contours of constant $k(x,\delta k_x)^2<k_0^2$ are simple closed curves, enclosing a finite dimensionless area $\phi(k^2)$, given by

$$\phi(k^2) = 2\int_{x_-}^{x_+}dx\left(k^2-\kappa(x)^2\right)^{1/2}, \tag{3.115}$$

where $x_-(k^2) < x_+(k^2)$ are the two "turning point" solutions of $\kappa(x_\pm)^2 = k^2$. Since $\kappa(x)$ is assumed to be monotonic, this can be written as

$$\begin{aligned} \phi(k^2) &= 2\int_0^{|k|} dy \left(k^2 - y^2\right)^{1/2} \left(\frac{1}{\kappa'_+(y^2)} + \frac{1}{\kappa'_-(y^2)}\right), \\ \kappa'_\pm(k^2) &\equiv \left.\frac{d\kappa}{dx}\right|_{x_\pm(k^2)}, \end{aligned} \tag{3.116}$$

Note that this transformation has turned $\phi(k^2)$ into a *signed* area, where $\mathrm{sgn}(\phi) = \mathrm{sgn}(k_0)$, which is indeed the correct form (the function $\phi(k^2)$ vanishes as $k_0 \to 0$, when its domain $k^2 \le k_0^2$ shrinks to zero). In the limit $k^2 \to 0$, $x_\pm(k^2) \to x_0$, the formal location of the interface. Then $\kappa'_\pm(k^2) \to \kappa'(x_0)$, and $\phi(k^2)$ vanishes as

$$\phi(k^2) \to \frac{\pi k^2}{\kappa'(x_0)}, \quad (k/k_0)^2 \to 0. \tag{3.117}$$

It is very instructive to examine the special case

$$\kappa(x) = k_0 \tanh(\alpha(x - x_0)), \tag{3.118}$$

which is integrable. In this case,

$$\kappa'(x) = \alpha k_0 \mathrm{sech}^2(\alpha(x - x_0)), \tag{3.119}$$

$$k_0 \mathrm{sech}^2(\alpha(x_\pm(k^2) - x_0)) = \frac{k_0^2 - k^2}{k_0}. \tag{3.120}$$

Thus the explicit dependence on $x_\pm(k^2)$ can be eliminated, and

$$\kappa'_\pm(k^2) = \alpha\left(\frac{k_0^2 - k^2}{k_0}\right). \tag{3.121}$$

This make the integral for $\phi(k^2)$ trivial (it becomes expressible in terms of a simple Hilbert transform), and the asymptotic small-k^2 form (3.117) remains valid for *all* values of k^2 in the domain of the function:

$$\phi(k^2) = \frac{\pi k^2}{\alpha k_0}, \quad k^2 \le k_0^2. \tag{3.122}$$

Then the frequency of the interface mode with wavenumber $\delta k_y = \delta k_\parallel$ along the interface can be expressed as

$$\begin{aligned} \omega(\delta k_\parallel, \phi) &= \omega_D \pm v_D \left(\delta k_\parallel^2 + \kappa_\perp^2(\phi)\right)^{1/2}, \\ \kappa_\perp^2(\phi) &\equiv |\alpha k_0 \phi|/\pi. \end{aligned} \tag{3.123}$$

A standard "semiclassical" analysis of interference effects on a light ray trapped in a "waveguide" at an interface would conclude that the "quantized" values of ϕ corresponding to interface modes were

$$\phi_n = 2\pi n + \gamma, \tag{3.124}$$

where γ is a "Maslov phase", usually π. In this case, comparison with the exact solution of the integrable problem confirms that this problem instead has a vanishing "Maslov phase" $\gamma = 0$. This can be attributed to an underlying "Z_2" Berry phase factor of -1 (Berry phase of π) for orbiting around the degeneracy point at $(x - x_0, k_x) = (0, 0)$.

We then conclude that the interface modes at a slowly-varying interface are in general given (for small $\delta k_\parallel$) by

$$\begin{aligned} \omega_0(\delta k_\parallel) &= \omega_D + v_D \mathrm{sgn}(\mathrm{k}_0)\delta k_\parallel, \\ \omega_{n\pm}(\delta k_\parallel) &= \omega_D \pm v_D \left(\delta k_\parallel^2 + k_n^2\right)^{1/2}, n \geq 1, \\ \phi(k_n^2) &= 2\pi n, \quad k_n^2 \leq k_0^2. \end{aligned} \tag{3.125}$$

The unidirectional "zero mode" persists however sharp the interface is; the bidirectional modes with $n \geq 1$ must obey $2\pi n < \phi(k_0^2)$, which has fewer and fewer (and eventually no) solutions as the width of the interface region shrinks. In the special case of the integrable model (3.118), this spectrum is exact for small $\delta k_\parallel$ without any condition that the wall is slowly varying.

3.7 Discussion

We have shown that under certain circumstances, the zero-energy modes of the 2D Dirac Hamiltonian are have the same properties of the edge modes of quantum Hall systems: they are chiral (unidirectional), and dissipationless. We have taken a system that can be described by a 2D Dirac Hamiltonian, and we have tuned the parameters of the system in a special way, such that the mass term of the Dirac Hamiltonian changes sign at certain critical values of a tuning parameter. In the photonic system, this tuning parameter is precisely

the Faraday effect, a perturbation that breaks time-reversal symmetry and generates Dirac mass terms in a system with hexagonal symmetry.

We have shown that analogs of quantum Hall effect edge modes can exist in photonic crystals whose band gaps can be tuned by a Faraday coupling. The crucial new feature we present here here is that photonic systems can have bands with non-trivial topological properties including non-zero Chern invariants. These in turn can be varied in a controlled manner to yield unidirectional ("chiral") edge modes. The edge modes are robust against elastic back-scattering since they are states which are protected by the underlying 2D band structure topology. However, they are not robust against photon number non-conserving processes, such as absorption and other non-linear effects. We believe that this could be an entirely new direction in "photonic band structure engineering" due to the absence of scattering at bends and imperfections in the channel.

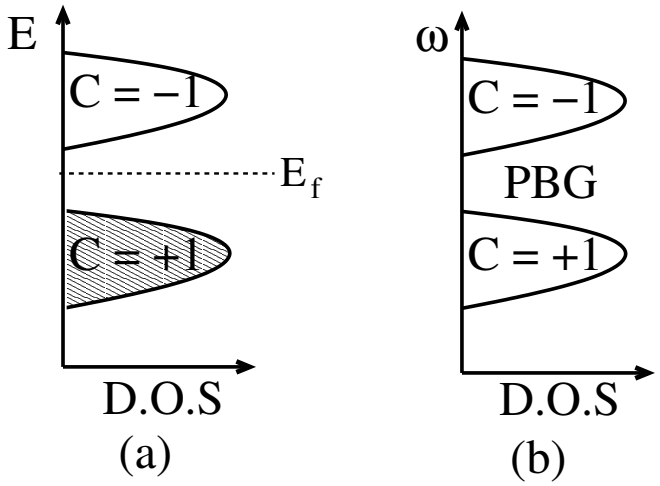

Figure 3.18: We have shown in this chapter that because the photon bands (b) cannot be filled as in the electronic case (a), they can have no analog of the bulk quantum Hall effect. However, the Chern number is a topological invariant of Bloch states independent of the constituents. With the Faraday term, we are able to tune the system such that the total Chern number below a photonic band gap changes across in interface, which gives rise to unidirectionally propagating edge modes of photons localized at the interface. These modes are direct analogues of the "Chiral" edge modes of electronic systems which occur at interfaces between two regions having different total Chern invariants below the Fermi level (i.e. with different Hall conductances).

A practical realization of such one-way transmission channels in photonics will necessarily have to deal with the problem of finding a magneto-optic material with a strong enough Faraday effect to confine the light close to the interface. Furthermore, in a practical design, the problem of TE/TM mode mixing when light is confined in the direction perpendicular to the 2d system will have to be addressed. A practical design could, for instance, make use of PBG materials to confine light in the z-direction.

Throughout, we have been discussing the case of two dimensional bandstructures. The stability of the Dirac points, and the topological Chern invariants which we derived are not stable in a three dimensional bandstructure. The reason for this is as follows. In the two dimensional bandstructures, the Dirac points are not degenerate with other modes. However, the Dirac points will be degenerate with other bands when k_z, the Bloch vector in the z-direction, is non-zero. This would destroy the robustness of the edge modes. A successful realization of the modes discussed here will therefore also have to confine the light to two-dimensions. A possible way to achieve this would be to vary the filling factor of the dielectric rods along the z-axis, so that the light would remain confined to a region of somewhat larger filling factor. To design the correct shape of the rods to achieve this, one must remember that the two dimensional bandstructure itself is highly sensitive to the filling factor of the rods. One must be careful, therefore, not to introduce states in the vicinity of the Dirac points by varying this filling fraction too drastically. This is a somewhat delicate optimization problem, but there is no reason to believe that the problem is insurmountable. It is interesting to think of the technological applications of the modes constructed and analyzed in this chapter. Provided the effect of photon number non-conserving effects remains minimal, there are many interesting applications of these modes for which conventional optical isolators remain inappropriate. The chirality of the modes, for instance, could be employed to define a photonic analog of a bit. As these modes are robust against backscattering and imperfection along bends, they could be used to transmit light (and information) in a narrow frequency window with minimal loss. There seem to be endless possibilities for the use of a topologically protected dissipationless unidirectional

modes of light in fields as diverse as computer science, engineering, and medicine.

Although there are many obstacles to the realization of such interesting effects in photonics, none of them are fundamental, and we believe that these unidirectional channels could have potentially useful technological applications which could in principle be realized someday through "bandstructure engineering".

Chapter 4

Numerical Algorithms for bandstructure computations

In this chapter, we shall describe our formulation of the photonic bandstructure problem which has been used in the numerical computations of the edge mode spectra.

The standard approach to the numerical problem of computing photon spectra in dielectric media [41] is restricted to periodic structures, and the complication of anisotropy in the constitutive relations is usually omitted. Within the standard approach, the Maxwell normal-mode problem is recast into an ordinary Hermitian eigenvalue problem of Schrodinger type $\boldsymbol{A}|\psi\rangle = \omega|\psi\rangle$, where

$$\boldsymbol{A} = \boldsymbol{\nabla} \times \left(\frac{1}{\epsilon(\boldsymbol{r})} \boldsymbol{\nabla} \times \right) \tag{4.1}$$

and $|\psi(\boldsymbol{r})\rangle$ is the local magnetic field vector $\boldsymbol{H}(\boldsymbol{r})$. The divergence-free condition $\boldsymbol{\nabla} \cdot \boldsymbol{H} = 0$ is an auxiliary condition which is justified within the approximation that the permeability tensor remains isotropic and uniform. The divergence-free condition is then used as a criterion to accept or reject possible solutions to the eigenproblem. The eigenvalue equation is written in $\boldsymbol{k}-$ space after expanding the fields in a set of plane waves, whose wave vectors are reduced to the first Brillouin zone, and standard linear algebra packages are used to treat the brute-force diagonalization of the problem. With this method, it is not possible to study frequency-dependent constitutive relations.

The method to be discussed below, however, is based on a real-space discretization of the Maxwell normal-mode problem. It is by no means restricted to periodic media (and can be readily used to study photonic "quasicrystals" [38] for which Bloch states do not exist). Furthermore, anisotropy and frequency dependence of the constitutive relations are immediately tractable within our method. Our motivation for developing this method has already been discussed in the previous chapter - in which we studied modes associated with domain walls in real space, across which the sign of the time-reversal breaking Faraday perturbation (an imaginary, anti-symmetric component of the dielectric tensor) changed.

The numerical approach described here only requires that the medium remains loss-free, linear, and describable by local constitutive relations. No other restrictions are imposed. Since we always neglect absorption/emission and other non-linear processes of light (i.e. we work within an approximation of photon number conservation), we seek a Hamiltonian formulation of the source-free Maxwell problem.

We have already described the basic formal structure of the continuum Hamiltonian formulation of the Maxwell normal mode problem in the previous chapter.

In the numerical implementation of a Hamiltonian formulation, we shall treat the continuum flux densities $\langle \boldsymbol{y}| = (\boldsymbol{D}, \boldsymbol{B})$ rather than $\langle \boldsymbol{r}| = (\boldsymbol{E}, \boldsymbol{H})$ as our fundamental dynamical variables. The former set obey the source-free Gauss' relations:

$$\nabla \cdot |\boldsymbol{y}\rangle = 0. \tag{4.2}$$

The Hamiltonian of our system is given by the following quadratic form:

$$\mathcal{H} = \frac{1}{2}\left(\boldsymbol{D}, \epsilon^{-1}\boldsymbol{D}\right) + \frac{1}{2}\left(\boldsymbol{B}, \mu^{-1}\boldsymbol{B}\right). \tag{4.3}$$

Furthermore, the propagating solutions of Maxwell's equations require the fields to be coupled in non-canonical Poisson bracket relations:

$$\{D^a(x), B^b(x')\} = \epsilon^{abc}\nabla_c \delta^3(x - x') \tag{4.4}$$

The two sets of fields are related by $|\boldsymbol{y}\rangle = \boldsymbol{B}|\boldsymbol{r}\rangle$, where $\boldsymbol{B}$ is the matrix of constitutive

relations introduced in the previous chapter:

$$B = \begin{pmatrix} \epsilon_{ab}(\boldsymbol{r}) & 0 \\ 0 & \mu_{ab}(\boldsymbol{r}) \end{pmatrix} \tag{4.5}$$

The source free Maxwell equations are slight variants of the ones described in section II. Written as a generalized eigenmode problem of form

$$\boldsymbol{A}\tilde{\boldsymbol{B}}|\boldsymbol{y}\rangle = \omega|\boldsymbol{y}\rangle. \tag{4.6}$$

The matrix $\boldsymbol{A}$ is the imaginary anti-symmetric matrix introduced in section II, and $\tilde{\boldsymbol{B}} = \boldsymbol{B}^{-1}$ is a positive-definite Hermitian matrix. The eigenmode problem here is formally analogous to the problem of a non-canonical harmonic oscillator with Hamiltonian

$$\mathcal{H} = \frac{1}{2}\sum_{ij} \tilde{B}_{ij} y_i y_j, \tag{4.7}$$

and Poisson brackets

$$\{y_i, y_j\} = -iA_{ij}. \tag{4.8}$$

Since $\boldsymbol{A}$ is imaginary and anti-symmetric, its eigenvalues are either zero, or come in pairs with opposite sign. It is the presence of zero modes which prevents a canonical treatment of the problem. In the Maxwell problem, one third of the $\boldsymbol{A}$ matrix eigenvalues are zero modes.

4.1 Spatial discretization of the normal-mode problem

We now discuss the spatial discretization of this problem which is needed for the computational algorithm. We start by constructing a tessellation of space into polyhedral cells, whose vertices $\boldsymbol{R}_i^e$ shall store the local inverse permittivity tensor $\epsilon_{ab}^{-1}(\boldsymbol{R}_i^e)$. We also define the sites $\boldsymbol{R}_i^m$, where the local values of the inverse permeability tensor $\mu_{ab}^{-1}(\boldsymbol{R}_i^m)$ will be represented. The polyhedra whose vertices are $\boldsymbol{R}_i^e$ are "dual" to the polyhedra whose vertices are the sites $\boldsymbol{R}_i^m$, as we explain below. For the moment, however, consider only the electric component.

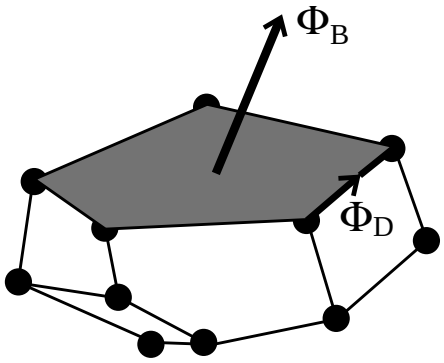

Figure 4.1: The generic discretization scheme for the photon Band structure problem. Space is broken up into polyhedra. Local electric energy density is defined at the vertices of each polyhedron, and the electric fluxes, defined on the edges of the polyhedron, connect two electric energy sites. The volume of the polyhedron is associated with local magnetic energy density, and magnetic fluxes "live" on the faces of the polyhedron. The scheme here has electric-magnetic duality in that a dual polyhedron can be defined on the vertices of which magnetic energy density defined, etc. The scheme here is inspired by lattice QED, which ensures the correct long wavelength photon dispersion; the only difference here is absence of sources.

Before we discuss the fluxes, we note here that the polyhedra of electric sites need not form a regular array - the set of points may be chosen quite randomly, and in a sophisticated calculation, the points could be chosen in an optimal fashion in order to discretize the continuum most efficiently (the criterion of what set of points are optimal for a given problem will depend on the geometry of the system to be studied on a macroscopic scale).

4.1.1 The Voronoi cell construction

Having specified the points where the electric constitutive relations are defined, we next describe a scheme by which we partition the local electric energy density in space. To each point in the electric lattice $\boldsymbol{R}_i^e$, we identify a volume of space which is closer to the point $\boldsymbol{R}_i^e$ than to any other electric point. This is a generalization of the wigner-Seitz construction of Brillouin zones, and is known as the *Voronoi* construction. The voronoi construction is the most general method of assigning energy to each point, and it is also used to define the network properties of the electric polyhedron: two points $\boldsymbol{R}_i^e$ and $\boldsymbol{R}_j^e$ are neighbors if their respective Voronoi cells share a common face. We label each Voronoi cell by the site $\boldsymbol{R}_i^e$ to

which they belong.

If two electric sites are neighbors as defined above, then local energy density may be transported from one cell to its neighbor via the electric flux vector, which will be associated with the common face connecting the two sites $\boldsymbol{R}_i^e$ and $\boldsymbol{R}_j^e$. To endow the flux with a direction in real space, we associate a normal vector to each face of the voronoi cell (the sign of the normal vector is ambiguous and we are free to set our own Z_2 convention here). Notice that in the special case in which the points $\boldsymbol{R}_i^e$ form a simple cubic array, the electric fluxes are defined on the directed bonds of the lattice. Having specified a convention for the signed area of each face of every Voronoi cell, we can unequivocally identify each electric flux vector to either be entering or leaving a Voronoi cell.

Let us define the quantity $\delta_j(\boldsymbol{R}_i^e)$ associated with each electric flux Φ_j^e of the system by $\delta_j(\boldsymbol{R}_i) = +1$ if Φ_j is an outward flux, $\delta_j(\boldsymbol{R}_i^e) = -1$ if it is an inward flux, and $\delta(\boldsymbol{R}_j^e) = 0$ if Φ_j is not associated with one of the faces of the Voronoi cell $\boldsymbol{R}_i^e$. This way, we define the electric divergence of each cell to be

$$\delta\Phi^e(\boldsymbol{R}_i^e) = \sum_j \delta_j(\boldsymbol{R}_i^e)\Phi_j \tag{4.9}$$

4.1.2 Self-duality

Having specified the electric energy sites and fluxes, we now turn to the magnetic sector. To each polyhedron of the electric sublattice, we associate a dual polyhedron whose vertices will consist of the set $\boldsymbol{R}_i^m$ where local values of the inverse permeability tensor $\mu_{ab}^{-1}(\boldsymbol{R}_i^m)$ are defined. The duality is such that the vertices $\boldsymbol{R}_i^m$ of the magnetic site polyhedra are associated with the enclosed volumes of each of the electric polyhedra (we do not require the magnetic sites to correspond to the centroid of the electric polyhedra; the requirement that they remain somewhere in the interior is sufficient. This way, magnetic energy can flow from one site $\boldsymbol{R}_i^m$ to another $\boldsymbol{R}_j^m$ via local magnetic fluxes Φ^m which we associate with the links of the magnetic polyhedron. We can repeat the above construction for the magnetic cells $\boldsymbol{R}_i^m$ by constructing the dual magnetic Voronoi cells and by defining the local magnetic divergence $\delta\Phi^B(\boldsymbol{R}_i^m)$ as in Eq. 4.9. In both cases, the fluxes will be divergence free due to

the absence of electric and magnetic sources in our formulation.

The self-duality of the source-free Maxwell equations (in three spatial dimensions) is preserved in our method. To see this, observe that we need not have defined a second dual set of polyhedra to describe the magnetic sector of our system. Simply by working with the electric polyhedra, we may proceed correctly by associating magnetic energy density with the enclosed volume of each polyhedron, and magnetic fluxes with the faces of the polyhedron, as shown in Fig. 4.1. As we did in the Voronoi construction, we choose a convention for the sign of the area of each face of the electric polyhedron. This will ensure well defined magnetic fluxes satisfying the local divergence-free condition. The next thing to describe is the coupling of the electric and magnetic fluxes which comes from the Faraday-Maxwell equations.

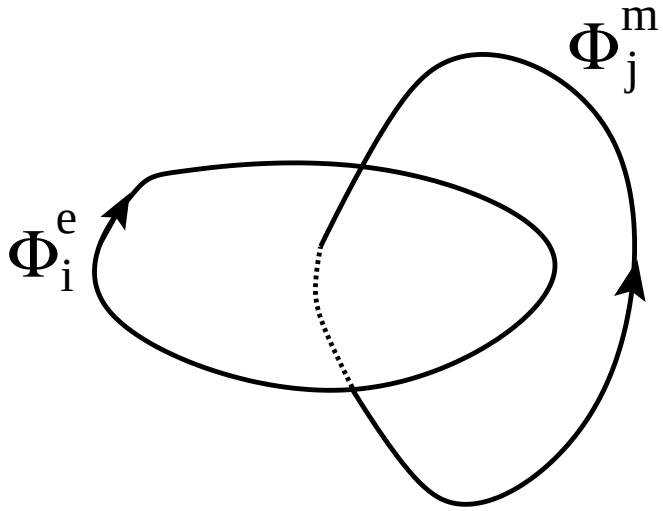

Figure 4.2: The topological linking number $\mathcal{L}_{ij}$ which encodes the Poisson bracket relations equivalent to the Faraday-Maxwell equations. The Linking number shown here corresponds to $\mathcal{L}_{ij} = +1$, since the two loops are oriented such that, for example, the flux Φ^e_i crosses the surface whose perimeter consists of magnetic fluxes Φ^m_j, and flows in the same direction as the outward normal vector of the loop, and vice-versa.

From the value of the outward normal vector for each face of the electric polyhedron, we can associated perimeters of every polyhedron face with directed loop - whose signs are determined by a right-hand convention based on the choice of the outward normal

vector. The perimeters allow us to define electromotive forces (EMFs) and magnetomotive forces (MMFs) locally Having specified the directed loops of the system, we now shall see that the Hamiltonian dynamics, given by the Poisson-bracket relations in Eq. 4.8, takes a particularly simple and elegant form in this construction. We define the *linking number* $\mathcal{L}_{ij}$ between an electric flux Φ_i^e and magnetic flux Φ_j^m to be zero if the directed loops associated with fluxes Φ_i^e and Φ_j^m do not entwine. We also define the linking number to be $\mathcal{L}_{ij} = +(-)1$ (see Fig. 4.2) if the loops associated with the two fluxes entwine in a positive (negative) manner. The Faraday-Maxwell equations are expressible in terms of the linking numbers as

$$\partial_t \Phi_i^e = \sum_j \mathcal{L}_{ij} \frac{\partial H}{\partial \Phi_i^e}, \tag{4.10}$$

$$\partial_t \Phi_i^m = -\sum_j \mathcal{L}_{ij} \frac{\partial H}{\partial \Phi_i^m} \tag{4.11}$$

The flux derivatives in the above equations are the EMF's and MMF's along the electric and magnetic perimeters, respectively. The Faraday-Maxwell laws relates the EMF around the perimeter associated with an electric flux Φ_i^e with the time variation of the magnetic flux traversing the face bounded by the perimeter. In this fashion, the electric and magnetic fluxes are coupled in a purely topological (i.e. metric independent) fashion as

$$\{\Phi_i, \Phi_j\} = \mathcal{A}_{ij} = i\mathcal{L}_{ij} \tag{4.12}$$

We now consider the problem of discretizing the Hamiltonian on the network. We construct a local Hamiltonian of the form

$$H = \sum_i h(\boldsymbol{R}_i^e) + h(\boldsymbol{R}_i^m). \tag{4.13}$$

To encode the Poisson bracket relations correctly, we simply tabulate the linking numbers associated with every pair of fluxes in the system. Clearly, such a matrix will be huge but extremely sparse, reflecting the locality of the Maxwell equations.

While the Poisson bracket relations are purely metric-independent, the Hamiltonian involves the geometry of the network. To generate the local Hamiltonian matrix, which couples fluxes of the same type only in standard electromagnetism, we proceed as follows.

For each vertex $\boldsymbol{R}_i^e$ of the electric polyhedron, we first determine the number of electric fluxes associated with the vertex (which is the same as the number of links emanating from the site, or , in the Voronoi construction, the number of faces of the Voronoi cell). Next, we compute the scalar products of every electric flux pair (which depends on the geometry of the polyhedron, and the anisotropy of the constitutive relations), and compute the inverse areas and lengths associated with each such flux. The Hamiltonian in the magnetic sector proceeds in precisely the same manner, except that the inverse areas and volumes of the magnetic fluxes are computed using the dual polyhedron. To see how all this is done within a simple context, we shall construct the Hamiltonian matrix and the Poisson bracket relations for the case where the set of points $\boldsymbol{R}_i^e$ form a regular lattice.

4.2 Discretization on regular lattices

In this section, we make some of the ideas presented above more concrete by discussing a practical implementation of the structure on a regular network. We have successfully implemented the discretized versions of the Poisson bracket relations and the Hamiltonian on simple cubic, body-centered cubic, and face-centered cubic networks, but for the sake of clarity, we describe here the simple cubic implementation. The ideas presented here are somewhat similar to earlier work by Pendry [51], where a simple cubic network was used to compute transmission amplitudes of photonic systems. Although the discretization scheme is similar to Ref. [51], our formulation of the eigenvalue explained above is entirely different.

Consider the simple cubic lattice, with the lattice spacing set to a. The elementary translations,

$$\boldsymbol{a}^1 = (a, 0, 0)\,, \boldsymbol{a}^2 = (0, a, 0)\,, \boldsymbol{a}^3 = (0, 0, a)\,, \tag{4.14}$$

and half-translations $\boldsymbol{b}^i = \boldsymbol{a}^i/2$ will be used to identify all the flux sites. In this network, the inverse permittivity ϵ_{ij}^{-1} tensor will "live" on the vertices $\{\boldsymbol{R}_i^e\} = \{l\boldsymbol{a}^1 + m\boldsymbol{a}^2 + n\boldsymbol{a}^3\}$, whereas the permeability μ_{ij}^{-1} will live on the dual lattice sites corresponding to the centers of each cube of the electric lattice: $\{\boldsymbol{R}_i^m\} = \{(l + 1/2)\,\boldsymbol{a}^1 + (m + 1/2)\boldsymbol{a}^2 + (n + 1/2)\boldsymbol{a}^3\}$. The dynamical flux variables "live" on the links of this network as follows: $\{D^j(\boldsymbol{R}_i^e)\} =$

$\{\boldsymbol{R}_i^e + \boldsymbol{b}^j\}$, $\{B^j(\boldsymbol{R}_i^m)\} = \{\boldsymbol{R}_i^m + \boldsymbol{b}^j\}$, $(j = x, y, z)$. Thus, the electric fluxes $(\Phi^e(\boldsymbol{R}_i^e + \boldsymbol{b}^j) = D^j(\boldsymbol{R}_i^e)/a^2)$ are associated with the directed links of the simple cubic lattice whereas the magnetic fluxes $(\Phi^m(\boldsymbol{R}_i^e + \boldsymbol{b}^j) = B^j(\boldsymbol{R}_i^e)/a^2)$ are defined on the directed faces of the network, which are the directed links of the "dual" magnetic network (which is also a simple cubic array). Since each face/link of the network unambiguously specifies the type of flux associated with it, the superscripts $\{x, y, z\}$ of the fluxes are redundant, and are omitted.

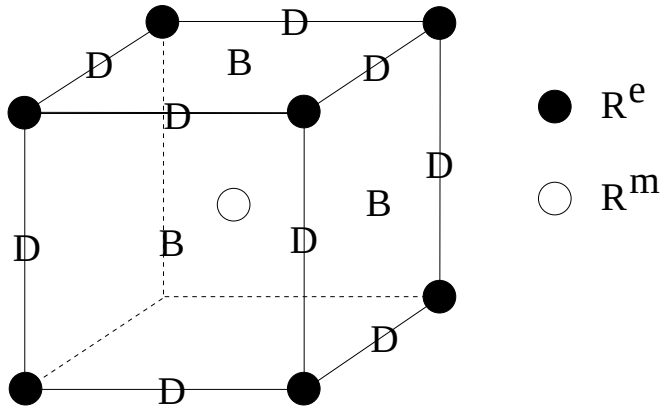

Figure 4.3: The enumeration of the Basis on the simple cubic network. Here, D and B refer to the electric and magnetic flux sites, respectively.

The non-canonical Poisson bracket relations between the electric and magnetic fluxes are implemented by the following equation:

$$\{\Phi^e(\boldsymbol{R}^e + \boldsymbol{b}^i), \Phi^m(\boldsymbol{R}^m + \boldsymbol{b}^j\} = i \sum_{\sigma=\pm} \sigma \epsilon^{ijk} \delta \left(\boldsymbol{R}^m - \boldsymbol{R}^e, \boldsymbol{b}^i - \boldsymbol{b}^j + \sigma \boldsymbol{b}^k \right), \tag{4.15}$$

where we have made use of the Kronecker delta function $\delta(\boldsymbol{x}, \boldsymbol{y}) = 1$ if $\boldsymbol{x} = \boldsymbol{y}$ and 0 otherwise. Furthermore, the Hamiltonian is simply

$$H = \frac{a^2}{2} \sum_n \sum_{ij} \epsilon_{ij}^{-1}(\boldsymbol{R}_n^e) \Phi^e(\boldsymbol{R}_n^e + \boldsymbol{b}^i) \Phi^e(\boldsymbol{R}_n^e + \boldsymbol{b}^j) + \mu_{ij}^{-1}(\boldsymbol{R}_n^m) \Phi^m(\boldsymbol{R}_n^m + \boldsymbol{b}^i) \Phi(\boldsymbol{R}_n^m + \boldsymbol{b}^j) \tag{4.16}$$

From the discretization above, we construct the basis set, on which our $\boldsymbol{A}$ and $\boldsymbol{B}$ matrices will act, by defining $|\boldsymbol{R}^e + \boldsymbol{b}^i\rangle$ and $|\boldsymbol{R}^m + \boldsymbol{b}^i\rangle$ to represent the local electric and magnetic fluxes, respectively. The $\boldsymbol{A}$-matrix has the following action in this basis:

$$\begin{aligned} \boldsymbol{A}|\boldsymbol{R}^e + \boldsymbol{b}^i\rangle &= i\sum_{jk\pm} \pm\epsilon^{ijk}|\boldsymbol{R}^e + \boldsymbol{b}^i \pm \boldsymbol{b}^j\rangle \\ \boldsymbol{A}|\boldsymbol{R}^m + \boldsymbol{b}^i\rangle &= -i\sum_{jk\pm} \pm\epsilon^{ijk}|\boldsymbol{R}^m + \boldsymbol{b}^i \pm \boldsymbol{b}^j\rangle \end{aligned}$$

The $\boldsymbol{B}$-matrix, which encodes the local constitutive relations is a sum of independent electric and magnetic parts. As part of the input data, the user supplies the local values of the permittivity and permeability tensors on their respective sites. We define (repeated indices are *not* summed in the following set of equations)

$$\boldsymbol{a}^i \epsilon^{-1}_{ij}(\boldsymbol{R}^e)\boldsymbol{a}^j = a^2 B^{ij}(\boldsymbol{R}^e) \tag{4.17}$$

$$\boldsymbol{a}^i \mu^{-1}_{ij}(\boldsymbol{R}^m)\boldsymbol{a}^j = a^2 B^{ij}(\boldsymbol{R}^m) \tag{4.18}$$

If the system is described by constitutive relations that are purely diagonal, the $\boldsymbol{B}$-matrix acting in this Hilbert space is purely diagonal. The off-diagonal parts of the constitutive relations will couple nearby fluxes on the lattice.

Next, we consider the complication where the constitutive relations are frequency- dependent. We tackle this by introducing extra degrees of freedom in our lattice corresponding to local oscillator modes. We discuss this in the simple context of the cubic network next.

4.3 Polaritons: frequency-dependence of constitutive relations

We have already discussed the formal aspects of the frequency dependence of the constitutive relations in the previous chapter. Here, we consider its implementation on the discrete network. For the sake of concreteness, we consider the implementation on the simple cubic network above.

Until now, our dynamical variables were simply our electric and magnetic fluxes, which are associated with directed links and faces of our electric lattice respectively. To treat the frequency dependence of the constitutive relations, we expand our Hilbert space and

introduce dynamical oscillator degrees of freedom at each of the electric and magnetic sites $\boldsymbol{R}^e$ and $\boldsymbol{R}^m$, and denote them as electric and magnetic polarization degrees of freedom, respectively. Each electric or magnetic polarization mode on any given site are represented by a set of canonical oscillator coordinates and momenta ϕ_{na}, π_{na} respectively (here n is an integer that labels the mode, and $a = x, y, z$) obeying the Poisson bracket relations:

$$\{\phi^{\sigma}_{ma}(\boldsymbol{r}), \pi^{\sigma'}_{nb}(\boldsymbol{r}')\} = \delta_{ab}\delta_{mn}\delta^{\sigma\sigma'}\delta(\boldsymbol{r} - \boldsymbol{r}'), \tag{4.19}$$

where $\sigma = e, m$. On the discrete network, the electric and magnetic polarizations live on different sites, the Dirac delta function in the Poisson bracket above becomes a Kronecker delta and is automatically satisfied by keeping the electric and magnetic polarization modes as independent degrees of freedom. On each polarization site $\boldsymbol{R}^{\sigma}$, let $N(\boldsymbol{R}^{\sigma})$ be the number of oscillator modes needed to capture the frequency response of the media. We allow the possibility that $N(\boldsymbol{R}^{\sigma})$ may vary from one site to another. Our system is now characterized by two sets of Poisson brackets - those which are non-canonical representing the fluxes, and the canonical relations representing the oscillators. The $\boldsymbol{A}$- matrix, is enlarged to accommodate the oscillator modes as follows. We add to our flux basis the states $|\boldsymbol{R}^{\sigma}; 1, n, a\rangle$ and $|\boldsymbol{R}^{\sigma}; 2, n, a\rangle$ to represent ϕ^{σ}_{na} and π^{σ}_{na} respectively. We choose the following convenient linear combination

$$|\boldsymbol{R}^{\sigma}; \pm, n, a\rangle = \frac{(|\boldsymbol{R}^{\sigma}; 1, n, a\rangle \pm |\boldsymbol{R}^{\sigma}; 2, n, a\rangle)}{\sqrt{2}} \tag{4.20}$$

The action of the discretized $\boldsymbol{A}$ -matrix on these states is the simple diagonal

$$\boldsymbol{A}|\boldsymbol{R}^{\sigma}; \pm, n, a\rangle = \pm|\boldsymbol{R}^{\sigma}; \pm, n, a\rangle \tag{4.21}$$

It thus turns out that in this expanded basis, the $\boldsymbol{A}$-matrix is no longer anti-symmetric.

Next, consider the $\boldsymbol{B}$-matrix enlarged to accommodate the polarization modes. For the sake of notational simplicity, we only discuss electric polarization. The magnetic polarization modes are constructed in exactly the same manner. As we have recorded in the previous chapter (section 3.2.3), we suppose that each oscillator mode n has a natural frequency ω_n associated with it, and the additional energy purely due to the oscillator mode is

$$H^{\epsilon} = \sum_i D^a \left(\alpha_i(\boldsymbol{r})^a \pi_i(\boldsymbol{r}) + \beta^a_i(\boldsymbol{r})\phi_i(\boldsymbol{r})\right) + \frac{1}{2}\sum_i \omega_i \left(\pi_i^2(\boldsymbol{r}) + \phi_i(\boldsymbol{r})^2\right)$$

Let us define

$$Z_n^a(\boldsymbol{r}) = \alpha_n^a(\boldsymbol{r}) + i\beta_n^a(\boldsymbol{r}) \tag{4.22}$$

As we saw in the previous chapter, the coupling of the oscillators to the local fluxes above led to the definition of a Hermitian tensor

$$\Gamma_n^{ab}(\boldsymbol{r}) = Z_n^{a*} Z_n^b \tag{4.23}$$

In the discrete network, the natural frequencies $\omega_n(\boldsymbol{R}^e)$, and the tensors $\Gamma_n^{ab}(\boldsymbol{r})$, in addition to the inverse dielectric tensor, will live on the electric polarization sites $\boldsymbol{R}^e$ (these are the input variables in our problem).

When the basis $|\boldsymbol{R}^e; \pm, n, a\rangle$ is used, the B-matrix has the following additional couplings:

$$\boldsymbol{B}|\boldsymbol{R}^e; +, n, a\rangle = \omega_n(\boldsymbol{R}^e)|\boldsymbol{R}^e; +, n, a\rangle + \frac{1}{2}\sum_{j,\pm} Z_{na}^{j*}(\boldsymbol{R}^e)|R^e \pm \boldsymbol{b}_j\rangle \tag{4.24}$$

$$\boldsymbol{B}|\boldsymbol{R}^e; -, n, a\rangle = \omega_n(\boldsymbol{R}^e)|\boldsymbol{R}^e; -, n, a\rangle + \frac{1}{2}\sum_{j,\pm} Z_{na}^{j}(\boldsymbol{R}^e)\boldsymbol{R}^e \pm \boldsymbol{b}_j\rangle \tag{4.25}$$

This completes our specification of the matrices when the constitutive relations have frequency dependence. We have assumed all along that the characteristic frequency of the media is out of range of the frequencies of interest.

4.4 Boundary conditions

Having assembled the machinery, we now discuss the boundary conditions. In order to get out the photon band spectra of a crystal, we proceed as follows. We consider a single unit cell of the crystal of interest, we discretize space as described above such the discretization forms a fine mesh closely approximating the continuum. To study the spectrum as a function of the Bloch vector, we study the unit cell of the crystal on a torus (of dimension $L_x \times L_y$, where L_x and L_y are the discretizations in the x, and y directions), with twisted boundary conditions for the fluxes:

$$\Phi^\sigma(\boldsymbol{r} + L_a\hat{a}) = \exp(ik_a)\Phi^\sigma(\boldsymbol{r}) \tag{4.26}$$

By varying $\boldsymbol{k}$ in the Brillouin zone, we can compute the spectra of the bands. This was the method by which we determined spectra of two dimensional bandstructures in the previous chapter.

It is also quite straightforward to consider metallic boundaries with this method, as follows. We place the perfect conductor on our network, and determine the electric sites corresponding to zero values of the inverse dielectric tensor. When these zero's are introduced, it becomes clear that some fluxes emanating from these sites do not contribute to the energy, and must be excluded when we create our basis set. In the perfect metal, we will also have magnetic flux sites which are static since the electric fields are identically zero. These static magnetic flux sites must also be excluded. In our basis set, we keep all fluxes whose Poisson brackets with the Hamiltonian do not vanish.

4.5 Summary

We now recap the results of this section and make a few additional comments.

In our scheme, The electrical fluxes, Φ_D are defined on the edges of the polyhedron, while the magnetic fluxes, Φ_B are associated with the faces of each cell. Finally, magnetic energy and the local inverse permeability tensor $\mu_{ij}^{-1}(\boldsymbol{r})$ are defined on the centers of each polyhedron.

This discretization scheme preserves the self-duality of the source-free Maxwell equations in three dimensions; for each such electric polyhedron described above, there is a dual magnetic polyhedron whose faces correspond to the edges of the electric polyhedron, and whose center corresponds to the vertices of the electric polyhedron.

The discretized form the $\boldsymbol{A}$ matrix couples electric fluxes to magnetic ones, and vice-versa. The coupling is (see Fig. 4.4)

$$A_{ij}^{DB} = \{\Phi_i^D, \Phi_j^B\} = 0, \pm i. \tag{4.27}$$

The $\boldsymbol{B}$ matrix couples fluxes of the same type, and depends on the geometry of the polyhedra used to discretize space. For the case of a simple cubic discretization, and for

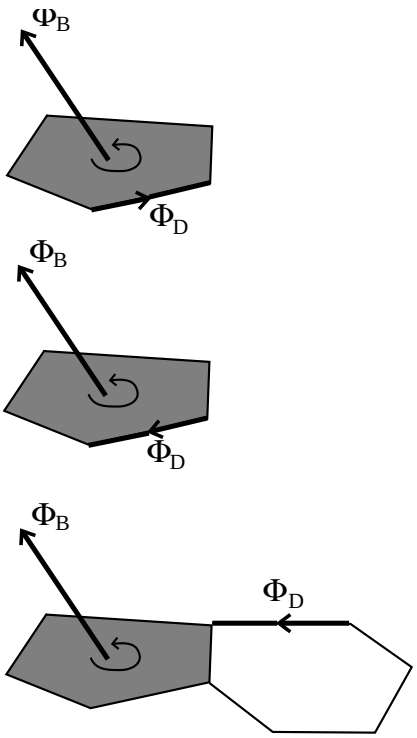

Figure 4.4: The discretized form of the $\boldsymbol{A}$, which contains the Poisson bracket relations of the fluxes. Shown here are example configurations of $\{\Phi_i^D, \Phi_j^B\} = +i$ (top), $-i$ (middle), and 0 (bottom).

the electric fluxes (see Fig. 4.5),

$$B_{ii} = \frac{1}{2}\left(\epsilon_{ii}^{-1}(\boldsymbol{r}_1) + \epsilon_{ii}^{-1}(\boldsymbol{r}_2)\right) \tag{4.28}$$

$$B_{ij} = \frac{1}{4}\epsilon_{ji}^{-1}(\boldsymbol{r}_2). \tag{4.29}$$

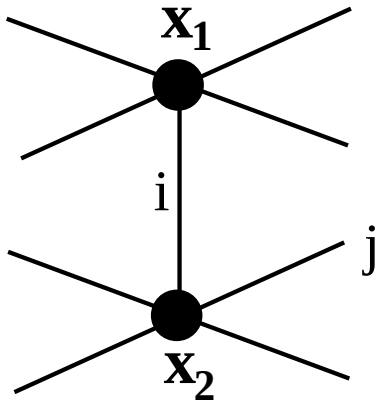

Figure 4.5: The discretized form of the $\boldsymbol{B}$, which contains the contains the geometric as well as the dynamics information. It couples fluxes of the same type only, and allows for anisotropy in the constitutive relations.

Identical relations involving the inverse permeability tensor are constructed for the magnetic fluxes. With the present formulation, the complete Hamiltonian of the system is expressed as a sum of local terms, $\mathcal{H} = \sum_n h(\boldsymbol{r}_n)$, with

$$h(\boldsymbol{r}_n) = \sum_{ij} B_{ij}(\boldsymbol{r}_n) y_i y_j. \tag{4.30}$$

Using this method, we can handle the case where the constitutive relations have generalized anisotropy, and vary in space.

Both the $\boldsymbol{A}$ and $\boldsymbol{B}$ matrix are sufficiently sparse and are stored as matrix-vector multipliers and are treated using a Lanczos algorithm. The standard Lanczos method determines extremal eigenvalues, while we seek the small positive eigenvalues of Eq. 4.6 that are just above a highly-degenerate set of zero modes.

The Lanczos adaptation for the Photonic problem is done by modifying the $\boldsymbol{A}$ matrix to

$$\boldsymbol{A} \rightarrow \boldsymbol{A}' = \boldsymbol{A}\boldsymbol{B}\boldsymbol{A} - 2\omega_0 \boldsymbol{A}, \tag{4.31}$$

$$\boldsymbol{A}'\boldsymbol{B}|\boldsymbol{y}\rangle = \omega(\omega - 2\omega_0)|\boldsymbol{y}\rangle. \tag{4.32}$$

Here, ω_0 is the lowest eigenvalue, and the low lying (negative) eigenvalues of the modified problem are now the physically relevant ones which are easily found with the Lanczos implementation. The dimensions of the matrices are $d = 6N$, where N is the number of points used to discretize the constitutive relations. We have found system sizes up to 10^6 to be accessible within this approach.

Chapter 5

Vortex dynamics and the Nernst effect

In this chapter, we study the problem of thermoelectric transport of extreme type II superconductors in a magnetic field. The magnetic field, which breaks time-reversal symmetry, endows the system with a net imbalance of vortices. These vortices, which are topological defects of the phase of the superconducting pair amplitude function, act in many ways as ordinary charges, which are defects of the electric field. We shall restrict our attention to the somewhat idealized case of a two-dimensional superconducting layer, in which case, the vortices are point defects. In this chapter, we investigate the role vortices play in thermoelectric transport experiments of extreme type II superconductors. The work here is motivated by a series of experiments done by Ong and collaborators on the Nernst effect and diamagnetism in the cuprate superconductors. The results presented here could also apply to quasi 2D granular superconductors, and Josephson junction arrays. The work presented in this chapter has been the result of an ongoing collaboration with Daniel Podolsky and Ashvin Vishwanath at U.C. Berkeley. I also have benefited from enlightening discussions with David Huse on this topic, whose ideas are reflected in some of the material of this chapter. At the time of writing, the material in this chapter remains unpublished.

5.1 Introduction

Since their discovery almost two decades ago, the cuprate superconductors continue to present a formidable challenge to our understanding of strongly correlated electronic systems. To date, a definitive microscopic theory which accounts for the superconductivity when the parent mott insulating materials are doped remains controversial. The primary challenge amounts to understanding the pseudogap regime, the crossover region between the mott insulating and superconducting phases which possesses many anomalous experimental signatures. The understanding of the relationship between the superconducting and pseudogap regimes continues to be one of the central puzzles in this area.

While these issues remain theoretically unresolved, recent experiments that have probed the dynamics and transport properties in this region of the phase diagram, have placed important constraints on potential theoretical models. In one such experiment, the frequency-dependent electrical conductivity $\sigma(\omega)$ was measured in underdoped BSCCO at zero applied field [12]. The results indicate that the proliferation of vortex- antivortex pairs contribute to the short time dynamics in the system above T_c. The experimental data is consistent with the notion first introduced by Emery and Kivelson [15], that the superconducting transition into the "normal" underdoped region marks the loss of phase coherence, rather than the destruction of the superconducting gap and pair formation.

Furthermore, the experiments on the Nernst effect [69] [67] [65] [66], and more recently, the measurements of diamagnetism [34], [64] have produced strong evidence for the presence of vortex degrees of freedom at temperatures well above T_c, which seem to develop smoothly out of the ordinary type II superconducting vortices below the transition temperature. In the Nernst experiments (see Fig. 5.1), the system is placed in a magnetic field ($\mathbf{H} = H\hat{z}$ with $\hat{z}$ taken to be along the c-axis), in a thermal gradient ($-\nabla T = -\hat{x}\frac{dT}{dx}$), and a DC electrical voltage is measured in the y-direction under open-circuit boundary conditions in both x and y directions. The Nernst signal is defined by the ratio

$$e_n = \frac{E_y}{-\nabla T} \tag{5.1}$$

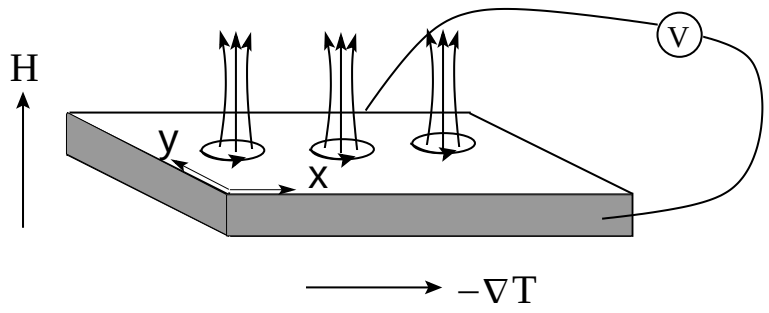

Figure 5.1: The setup of the Nernst experiment. A temperature gradient in the x-direction, and a magnetic field in the z-direction are applied. The DC electrical voltage is measured along the $y-$direction.

It is easily seen why the Nernst experiments are an ideal probe of vortex motion. If the system consisted of quasiparticles alone, the open circuit boundary condition constraint would be satisfied by a counterflow of hot and cold quasiparticles whose Hall voltages cancel identically, resulting in a negligible transverse electrical signal. Despite the heuristic nature of the above argument, the approximate cancellation of the Nernst signal in a system consisting of charged quasiparticles alone is well understood [54]. Vortex motion, on the other hand, can easily account for a non-zero Nernst signal; as a vortex diffuses down the temperature gradient, its phase slippage produces a voltage pulse transverse to its direction of motion. If there is a net imbalance of vorticity, which occurs at non-zero applied fields, there will be an unbalanced electrical signal which is interpreted as the Nernst signal.

While the frequency dependent conductivity measurements are heavily dependent on the dynamics of quasiparticles, the Nernst signal and more recent measurements of magnetization [34] [64] seem almost to be independent of quasiparticle dynamics. Indeed, while both conductivity and Nernst experiments point to vortex-like behavior above T_c, the temperature at which this behavior emerges differs depending on which experiment is used as the probe. The conductivity experiments, not surprisingly, point to a somewhat lower onset temperature of vortex excitations, which can be attributed to the complication of quasiparticle dynamics. For this reason, the Nernst experiments shall be the primary focus of this chapter.

Since the precise microscopic mechanism for superconductivity in the cuprates remains

unknown, theoretical work on the Nernst effect have all been phenomenological in flavor. Among the existing theoretical treatments of the Nernst experiments, the most promising approach has been to consider the Nernst signal as arising from superconducting fluctuations [61] obeying model A critical dynamics in the notation of Hohenberg and Halperin [22]. In this approach, vortices are not explicitly invoked, and thermoelectric response of superconducting (amplitude and phase) fluctuations is considered within time-dependent Ginzburg-Landau (TDGL) theory. At high temperature, near the onset temperature for the Nernst signal, a model of gaussian superconducting fluctuations accounts reasonably well for the experimental data, especially at optimal doping [61].

Here, we present a study of transverse thermoelectric transport within an idealized lattice london model that contains only phase fluctuations arising from vortex motion. Our model does not contain fermionic quasiparticles, nor does it contain amplitude fluctuations. Furthermore, due to the highly two dimensional nature of the layered cuprate superconductors, we are motivated to further simplify the problem by studying the Nernst effect in a two dimensional model.

This chapter is organized as follows. First, we review the magnetic phase diagram of a type II quasi 2D superconductor, derive our model Hamiltonian - the 2D frustrated XY model, and discuss the simplifying assumptions being made therein. Next, we consider relaxational (model A) dynamics for the Hamiltonian, construct expressions for currents, while carefully taking into account surface magnetization currents which do not transport net charge or energy. The magnetization and transverse thermoelectric transport coefficient α_{xy} are measured in simulations of the frustrated XY model with model A dynamics. We also show analytical results for the magnetization and α_{xy} at high temperatures.

In the second half of the chapter, we repeat some of the calculations above in the dual vortex representation using the Coulomb gas Hamiltonian. We consider the problem of dynamics of the Coulomb gas, and also discuss energy transport in this model. We then show results of measurements of magnetization and α_{xy} from Monte Carlo simulations. Some analytical results for magnetization at low temperatures are also presented. We also present

numerical results of thermoelectric transport in the dual model for small system sizes. We see that up to finite-size effects, the results from both the 2D frustrated XY model and its dual counterpart, the 2D coulomb gas model, are consistent with each other. Our main conclusion here is that 2D models with only phase fluctuations capture much of the experimentally observed phenomena of the Nernst effect and diamagnetism in the underdoped cuprate superconductors. Our work is consistent with the picture that the supercoducting transition in this regime is not a conventional BCS-type depairing transitions, but rather, it marks the loss of phase coherence in these systems.

5.2 Basic layout of the problem

In this section, we first provide some background by considering the phase diagram of a type II superconductor, focusing on quasi two dimensionality, and we consider the effects of thermal fluctuations on the mean field phase diagram [17]. From this, we setup our model, and discuss the simplifying assumptions being made.

5.2.1 The Magnetic phase diagram of a type II superconductor

A superconductor is classified as "type II" if the ratio of its magnetic penetration depth λ to its coherence length ξ is greater than $1/\sqrt{2}$.

At the level of mean-field theory, a type II superconductor has two distinct broken symmetry phases. At the lowest temperatures and fields, there is the Meissner phase, characterized by perfect diamagnetism, in which the system exhibits long-range phase coherence, and off-diagonal-long- range-order (ODLRO),

$$\lim_{r\to\infty}\langle\Psi^\dagger(0)\Psi(\boldsymbol{r})\rangle \approx \langle\Psi^\dagger(0)\rangle\langle\Psi(\boldsymbol{r})\rangle \neq 0. \tag{5.2}$$

Above a critical field $H_{c1}(T)$, the field begins to penetrate the system in the form of h/e^* vortices, and in addition to having ODLRO, the system breaks translational symmetry forming a vortex lattice. At higher fields and temperatures, the vortex lattice melts and the system loses its superconductivity altogether.

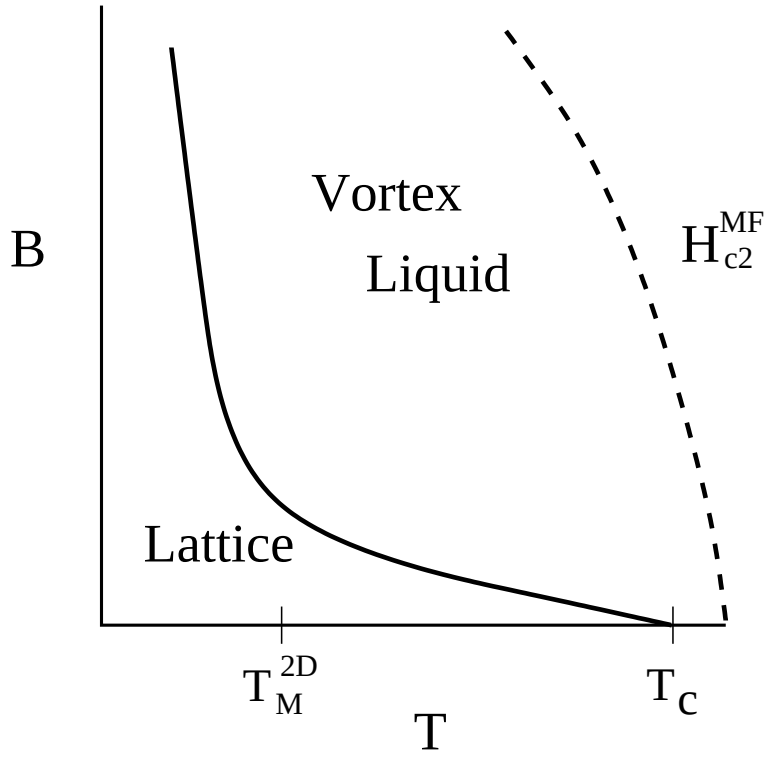

Figure 5.2: Magnetic phase diagram of a layered quasi 2D extreme type II superconductor.

When thermal fluctuations and disorder are properly taken into account [17] [16], the picture changes dramatically. Although the Meissner phase does not change much, the vortex lattice is less robust against disorder and fluctuations. For instance, quenched disorder, due to random pinning centers for the vortex cores, destroys the vortex lattice, and gives rise to the "vortex glass" phase [17] which remains superconducting, as long as the vortices remain pinned. We will ignore the Meissner phase in this chapter, and we do not study the complications associated with disorder. For a comprehensive account, see Ref. [17].

At higher temperatures, but at fields below the mean-field $H_{c2}(T)$, fluctuations melt the vortex lattice (or glass) into the "vortex liquid" phase, which is no longer superconducting (it has an Ohmic "flux-flow" resistance caused by the motion of vortices), at least at length scales larger than the zero temperature coherence length. This region of the phase diagram is connected by a smooth crossover to the normal phase above the mean-field upper critical field H_{c2}^{MF}. In the vortex fluid phase well below H_{c2}, there are local superconducting correlations still present, and the system can be consistently described using mobile vortices. However, the vortex picture begins to break down at higher fields, since pairing is essentially lost in this regime. The vortex liquid phase will be the focus of this chapter.

The phase diagram for a quasi 2D (layered) system is shown in Fig. 5.2. At zero field, there is a Kosterlitz-Thouless transition which occurs at a temperature, which is larger than the 2D melting temperature, but which is less than the mean field transition temperature. Depending on the anisotropy of the system, there will be a regime at low fields where the system will display 3D XY criticality. As the field is increased, however, there is a first order melting transition of the vortex lattice or glass into the liquid state which occurs somewhat below the zero-field Kosterlitz-Thouless temperature [16]. We shall always have in mind a highly anisotropic layered material which remains quasi 2D essentially throughout the vortex liquid regime. In this case, we may assume that the superconducting transition temperature occurs roughly at T_{KT}.

To be concrete, we consider the Ginzburg-Landau free energy for a layered type II superconductor in the presence of a magnetic field. The free energy density for such a

system is of the Lawrence-Doniach type:

$$f = \frac{\hbar^2}{2m_{ab}} \left| \left(\boldsymbol{\nabla} - i\frac{e^*}{\hbar c}\boldsymbol{A} \right) \psi_n(\boldsymbol{r}) \right|^2 + a(T) \left|\psi_n(\boldsymbol{r})\right|^2 + \frac{1}{2}\beta \left|\psi_n(\boldsymbol{r})\right|^4 + \sum_{<n,n'>} J_z \left|\psi_n - \psi_n'\right|^2, \quad (5.3)$$

where n labels the layer, m_{ab} is related to the inverse coherence length in the ab plane, J_z is the strength of the interlayer Josephson coupling.

The interlayer coupling cannot strictly vanish; in this case, although the systems conductivity will remain large, the Meissner phase is absent). However, we assume that $J_z << T_{KT}$, so that the 3D regime is essentially suppressed. Well above the superconducting transition, this system will consist of decoupled layers, each resembling a 2D superfluid film.

Well above the mean field transition temperature, the parameter β can be ignored, and the system has gaussian superconducting fluctuations. Thermoelectric transport in the gaussian regime has been treated in [61]).

Here, we will consider the regime which far enough above T_c such that a 2D description applies, but we also want to be sufficiently below the mean field transition temperature (where $a(T)$ changes sign) so that the amplitude of the superconducting order parameter remains frozen. When β is large, the value of T_c is suppressed well below its mean field value, and the dominant fluctuations are those of the phase. In this limit, focusing on a single independent layer, we have

$$\psi(\boldsymbol{r}) = \sqrt{\rho}_s \exp(i\theta(\boldsymbol{r})), \quad (5.4)$$

where ρ_s is a constant equal to the superfluid density, which we take to be a constant with no dynamics - an approximation equivalent to the statement that the superconducting phase fluctuations are classical, and our free energy resembles that of a London model of a superconductor. We further simplify the free energy by working in the extreme type II limit, where the superconducting coherence length ξ is much smaller than the magnetic penetration depth λ and the fluctuations in the gauge fields $\boldsymbol{A}$ may be reasonably neglected: when the system's penetration depth is much greater than the coherence length, it is quite reasonable to approximate the system as being placed in a uniform magnetic flux density. Thus, neglecting magnetic excitations altogether, along with fluctuations in the quadratic

term above, we obtain

$$F = \frac{\hbar^2}{2m} \int d^2 r \rho_s \left(\boldsymbol{\nabla} \theta(\boldsymbol{r}) - \frac{e^* \boldsymbol{A}}{\hbar c} \right)^2 . \tag{5.5}$$

The gaussian free energy makes the problem seem trivial; the missing ingredient here is that we have not considered the compact nature of the phase angles, a feature which permits topological defects - the vortex degrees of freedom. To remedy this, we shall work instead with a 2D frustrated XY model, and while the London model, strictly speaking, is defined in the continuum, we discretize onto a lattice:

$$\mathcal{H} = -J \sum_{<ij>} \cos \left(\theta(\boldsymbol{r}_j) - \theta(\boldsymbol{r}_i) - A_{ij} \right), \tag{5.6}$$

where $J = \hbar \rho_s / m$, (we set the lattice spacing to unity) $\boldsymbol{r}_i$ are the sites of a two-dimensional network, $\theta(\boldsymbol{r}_i)$ are angular variables defined on each site, corresponding to the phase of the superconducting order parameter (pair amplitude). $\boldsymbol{A}_{ij} =$ are quenched gauge fields defined on each link of the network as

$$A_{ij} = \frac{e^*}{\hbar c} \int_i^j \mathbf{A} \cdot d\mathbf{r} \tag{5.7}$$

The gauge invariant quantity of course, is the magnetic flux density perpendicular to the superconducting plane (a is the lattice spacing) :

$$H a^2 = \partial_x A^y - \partial_y A^x. \tag{5.8}$$

With these conventions, if the magnetic flux per plaquette of the lattice is one flux quantum $\phi_0 = hc/e^*$, then the gauge field A_{ij} winds by 2π around each plaquette

The model described here has been studied extensively in the past, both analytically [47] and (mostly) numerically [57]. In addition, most of the previous work here has been focused on numerical studies of special values of the external field: an example is the "fully frustrated" XY model, which occurs when there is half a flux quantum per plaquette. Our primary interest here is in the thermoelectric transport properties of this model, which have received somewhat less attention. We are interested not at particular values of the applied field; our main goal is to study thermoelectric response in this system as a function of applied field. In the next section, we introduce dynamical equations for the phase variables.

5.3 Relaxational Dynamics

To study transport, we must introduce some dynamics for the angles. There are many possible choices for the dynamics of the phase variables $\theta(\boldsymbol{r}_i, t)$, the only constraint being that it faithfully reproduces the equilibrium thermodynamic quantities of the Hamiltonian. In general, transport coefficients, such as the electrical and thermal conductivities, will depend on the details of the choice of dynamics, since their values depends on the relaxation time. Interestingly, however, the transverse thermoelectric coefficient, α_{xy}, does not depend on the relaxation time, a fact that can be understood from dimensional analysis, as we shall show later. An interesting and unresolved issue is to what extent α_{xy} is independent of the choice of dynamics. For instance, if we chose our dynamics such that various relaxation times depended either on energy or momentum, it is not clear whether α_{xy} remains insensitive to the value of the relaxation time.

Among the simplest dynamical choices are purely relaxational dynamics, for which

$$\tau\dot{\theta}(\mathbf{r}_i) = -\frac{\delta\mathcal{H}}{\delta\theta(\mathbf{r}_i)} + \eta(\mathbf{r}_i, t), \tag{5.9}$$

where the first term causes the phases to relax towards local minima of the free energy landscape, whereas the second term, the gaussian white noise, represents interactions with the phase variables with local degrees of freedom operating on a shorter length and time scales than those of interest (they transport charge and energy on much shorter time scales than the hydrodynamic ones of interest - observe that our lattice discretization used for the phases are in no way connected to the underlying chemical lattice). In our problem, they could represent, for example, a phonon bath, and without them, the system would remain trapped in metastable states. To ensure that the system obeying these dynamics reaches equilibrium, the correlators of the noise must satisfy

$$\langle \eta(\mathbf{r}_i, t)\eta(\mathbf{r}_j, t')\rangle = 2T\tau\delta_{ij}\delta(t - t') \tag{5.10}$$

The model described above, also known as time-dependent-Ginzburg-Landau (TDGL), or Model A dynamics [22], does not contain any conserved variables. Other dynamical choices,

which do contain conserved variables, include for instance the resistively-shunted-junction (RSJ) dynamics, which are appropriate for granular superconductors, and which conserve the local supercurrent at each junction. Still another example is that of Monte Carlo (i.e. Metropolis) dynamics, which are closely related to relaxational dynamics in classical systems. The issue of which set dynamical equations appropriately describes the superconducting transition has received much attention during recent times. To date, the issue remains unsettled (see, for instance, [2] and references therein). In what follows, we shall use the relaxational TDGL dynamics to compute the transport coefficients of interest.

5.4 Transport

Within the dynamical framework described above, local charge and heat current densities were heuristically motivated by the authors of Ref. [60] (see also [61]) for the system with both amplitude and phase fluctuations:

$$\boldsymbol{j} = -i\frac{e^*\hbar}{2m^*}\langle\psi^*\left(\boldsymbol{\nabla} - i\frac{e^*}{\hbar c}\boldsymbol{A}\right)\psi\rangle + c.c. \tag{5.11}$$

$$\boldsymbol{j}^Q = -\frac{\hbar^2}{2m^*}\langle\left(\partial_t - i\frac{e^*}{\hbar c}A^0\right)\psi^*\left(\boldsymbol{\nabla} - i\frac{e^*}{\hbar c}\boldsymbol{A}\right)\psi\rangle + c.c., \tag{5.12}$$

where $A^0 = c\phi$, and ϕ is the electric potential. When the amplitude of the order parameter is held fixed, we obtain the following:

$$j_{ij} = J\sin\left(\theta_j - \theta_i - A_{ij}\right) \tag{5.13}$$

$$j^E_{ij} = -\frac{J}{2}\left(\dot{\theta}_i + \dot{\theta}_j\right)\sin\left(\theta_j - \theta_i - A_{ij}\right) \tag{5.14}$$

The various transport coefficients are then obtained either by computing the average value of these currents in externally applied electric fields and temperature gradients, or by calculating the various current-current correlation functions in equilibrium via the Kubo formulae. In the absence of the magnetic field, the task of determining transport coefficients is fairly straightforward and both the external gradient and Kubo formula methods will produce the same result.

5.4.1 Magnetization currents

In the presence of a magnetic field, however, the current profile of the system can be dramatically be modified by the presence of diamagnetic currents which remain confined to the surface of the system. These currents are non-zero even at equilibrium in the absence of electric fields and temperature gradients. In general, the energy and charge current densities can be separated into a transport sector and a magnetization sector, namely,

$$\boldsymbol{j}(\boldsymbol{r}) = \boldsymbol{j}_{tr}(\boldsymbol{r}) + \boldsymbol{j}_{mag}(\boldsymbol{r}) \tag{5.15}$$

$$\boldsymbol{j}^E(\boldsymbol{r}) = \boldsymbol{j}^E_{tr}(\boldsymbol{r}) + \boldsymbol{j}^E(\boldsymbol{r}) \tag{5.16}$$

where the charge and energy magnetization currents are defined by

$$\boldsymbol{j}_{mag}(\boldsymbol{r}) = \boldsymbol{\nabla} \times \boldsymbol{M} \tag{5.17}$$

$$\boldsymbol{j}^E_{mag} = \boldsymbol{\nabla} \times \boldsymbol{M}^E, \tag{5.18}$$

and $\boldsymbol{M}^E$ is known in the literature (see e.g. [11] and [46]) as the "energy magnetization", representing the flow of energy around the edge of the system due to the breaking of time-reversal symmetry. The heat current density is defined by

$$\boldsymbol{j}^Q(\boldsymbol{r}) = \boldsymbol{j}^E(\boldsymbol{r}) - \phi(\boldsymbol{r})\boldsymbol{j}(\boldsymbol{r}), \tag{5.19}$$

where the total current densities are used in the definition above. Magnetization currents are divergence-free and by definition, they do not transport net charge or energy. Therefore,

$$\int \boldsymbol{j}(\boldsymbol{r}) \cdot \hat{n}\ dl = \int \boldsymbol{j}_{tr} \cdot \hat{n}\ dl \tag{5.20}$$

$$\int \boldsymbol{j}^E(\boldsymbol{r}) \cdot \hat{n}\ dl = \int \boldsymbol{j}^E_{tr} \cdot \hat{n}\ dl \tag{5.21}$$

Here, the integral is over a path that traverses the sample, and we compute the total charge and energy currents that cross this curve ($\hat{n}$ is perpendicular to the local tangent vector to the curve).

It turns out however, that there is a slight subtlety with the heat current. Unlike the energy and charge currents, the heat current cannot be sifted apart into a transport current and a divergence-free "heat magnetization" current. To see this, we use 5.19, and find that

$$\boldsymbol{j}^Q(\boldsymbol{r}) = \boldsymbol{j}^Q_{tr} + \boldsymbol{\nabla} \times \boldsymbol{M}^Q + \boldsymbol{\nabla}\phi \times \boldsymbol{M}, \tag{5.22}$$

where $\boldsymbol{j}^Q_{tr}(\boldsymbol{r}) = \boldsymbol{j}^E_{tr}(\boldsymbol{r}) - \phi(\boldsymbol{r})\boldsymbol{j}_{tr}(\boldsymbol{r})$, and $\boldsymbol{M}^Q = \boldsymbol{M}^E - \phi(\boldsymbol{r})\boldsymbol{M}$ (a quantity that does not seem to have a clear physical meaning). Thus, the heat current, when integrated across a path with traverses the system, is

$$\int \boldsymbol{j}^Q_{tr}(\boldsymbol{r}) \cdot \hat{n}\ dl = \int \left(\boldsymbol{j}^Q(\boldsymbol{r}) + \boldsymbol{\nabla}\phi(\boldsymbol{r}) \times \boldsymbol{M}\right) \cdot \hat{n}\ dl \tag{5.23}$$

This fact will prove to be crucial when measuring transport coefficients, which we next discuss.

5.4.2 Transport coefficients

Let us define

$$\boldsymbol{J}_{tr} = \frac{1}{L}\int \boldsymbol{j}_{tr} \cdot \hat{n}\ dl \tag{5.24}$$

$$\boldsymbol{J}^Q_{tr} = \frac{1}{L}\int \boldsymbol{j}^Q_{tr} \cdot \hat{n}\ dl \tag{5.25}$$

The various transport coefficients which are measured in experiments are related to the transport part of the electric and heat currents as follows:

$$\begin{pmatrix} \boldsymbol{J}_{tr} \\ \boldsymbol{J}^Q_{tr} \end{pmatrix} = \begin{pmatrix} \sigma & \alpha \\ \tilde{\alpha} & \tilde{\kappa} \end{pmatrix} \begin{pmatrix} \boldsymbol{E} \\ -\boldsymbol{\nabla}T \end{pmatrix}. \tag{5.26}$$

The transport coefficients σ, α, respectively, the electrical and thermoelectric conductivities, and the thermal thermal conductivity, κ, defined by $\boldsymbol{J}^Q_{tr} = -\kappa\boldsymbol{\nabla}T$ under open circuit boundary conditions, is given by $\kappa = \tilde{\kappa} - \tilde{\alpha}\sigma^{-1}\alpha$. The Nernst signal, defined in Eq. 5.1, is given by the ratio

$$e_N = \frac{\alpha_{xy}}{\sigma_{xx}}, \tag{5.27}$$

where we have neglected contributions from α_{xx} and σ_{xy} which only contribute when particle-hole symmetry is broken. This "zero Hall angle" approximation seems to be consistent with experimental data of flux-flow resistivity and the Nernst signal.

By looking at the Kubo formulae for the electrical conductivity,

$$\sigma_{xx} = \frac{1}{T}\int_0^\infty dt\langle j_x(t)j_x(0)\rangle, \tag{5.28}$$

and for α_{xy}

$$\alpha_{xy} = \frac{1}{T^2}\int_0^\infty dt\langle j_x(t)j_y^E(0)\rangle, \tag{5.29}$$

and by looking at the formulae for the currents themselves, we see that the electrical conductivity is proportional to the TDGL auto-correlation time, whereas α_{xy} is independent of it. Consequently, the Nernst signal, along with the electrical conductivity is quite sensitive to the choice of dynamics, whereas α_{xy} is less dependent on this choice. For this reason, we will for the most part focus on α_{xy} rather than e_N. This will also be the case later in this chapter, when we formulate the problem in the dual vortex representation.

Additionally, the transport coefficients obey the Onsager relations, which require that $\tilde{\alpha} = T\alpha$. Clearly, if the wrong currents are calculated (e.g. $\boldsymbol{j}^Q$ instead of $\boldsymbol{j}^Q_{tr}$), then one will find that the Onsager relations are not verified, and that the resulting transport coefficients have nothing to do with those measured in experiments. Therefore, we must be careful to add or to subtract the contributions from the magnetization currents in order to remain on the correct track. We have computed the transport coefficients both numerically and analytically at high temperatures by recasting the Langevin equation of motion into an action principle. We shall first describe the numerical simulations and next the high temperature expansions.

5.5 Results

We have simulated the frustrated 2D XY model (Eq. 5.6) with relaxational (model A) dynamics (Eq. 5.9) The phase degrees of freedom are discretized on the sites of a square lattice, and the gauge fields live on the directed links of the 2D lattice. We integrate the

Langevin equations of motion via a standard fourth-order Runge-Kutta method [5]. First, we establish the Kosterlitz-Thouless transition in this model by measuring the universal jump in the helicity modulus at zero magnetic field, which is given by the standard formula [68]:

$$\Upsilon = -\frac{< U >}{2N} - \frac{\beta}{N} \sum_i \sin\left(\theta_{i+\hat{x}} - \theta_i\right), \tag{5.30}$$

where U is the total energy of the system, and N are the number of lattice sites. We measure this quantity on a torus, and find that $T_{KT} = 0.887J$, which is consistent with the known literature. In what follows, we shall report all temperatures in units of T_{KT}. We have also studied numerically the helicity modulus at finite fields and find that our numerics reproduces standard numerical results [57]. We do not mention them further, as they are not relevant to our main focus.

Whereas the Kosterlitz-Thouless transition temperature is determined on a torus, we use a cylindrical setup to measure the remaining quantities. The geometry is described in Fig. 5.3. If either electric fields or temperature gradients are present, they are applied along the axis of the cylinder. Transport coefficients are also computed using the Kubo formulae by computing current-current time displaced correlation functions along the azimuthal directions of the cylinder.

We focus first on magnetization, which is independent of the choice of dynamics. We measure the diamagnetic reponse of our system to the externally applied magnetic field by measuring the surface magnetization currents along the edge rims of our cylinder. We have studied the supercurrent profile (i.e. the gauge-invariant phase differences associated with each link of the lattice) and indeed, we find the edge mode corresponding to the magnetization currents; the bulk currents are vanishingly small at equilibrium. To measure the magnetization, we make use of the relation

$$M = \sum_{x=1}^{N_x} \langle j^y(x) \rangle \left(x - x_0\right), \tag{5.31}$$

where N_x is the lattice discretization along the axial direction (taken to be the x-direction), $\langle j^y(x) \rangle$ is the average supercurrent density at position x, and x_0 is an arbitrary constant

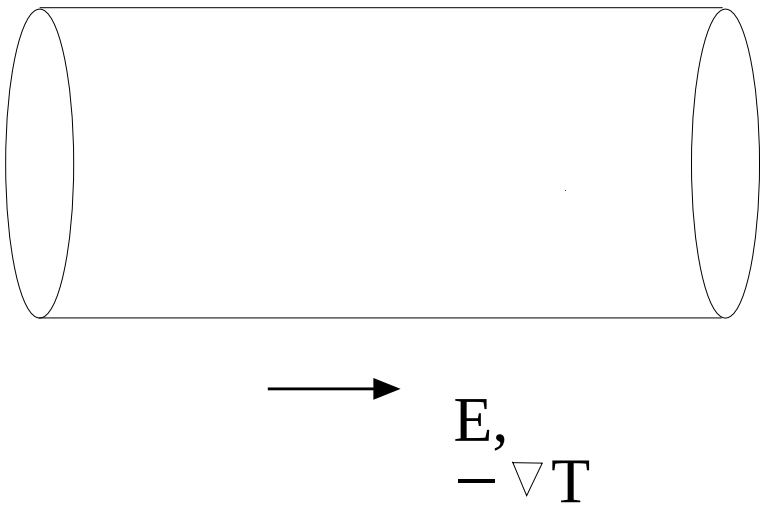

Figure 5.3: Geometry used in the simulations, the results of which are presented below. External fields are applied along the axial direction of the cylinder and in the measurements of the transverse thermoelectric coefficients, the resulting steady-state currents are measured along the azimuthal direction.

(since $\sum_x j^y = 0$). This relation is identical to $\boldsymbol{M} = 1/2\,(\boldsymbol{r} \times \boldsymbol{j})$, applied to the cylindrical geometry. The numerically computed magnetization is shown in Fig. 5.4. Indeed, there is a separatrix in the data at $T = T_{KT}$, below which the magnetization diverges logarithmically at low fields, and above which the magnetization appears linear in the magnetic flux density. The data is shown as a function of applied field (in our units, a unit flux quantum represents 2π worth of flux). Various temperatures (in units of T_{KT}) are shown.

Next, we consider dynamical quantities. The electrical conductivity is determined both via the Kubo formula, and via the direct method, in which an electric field (introduced via a time-varying vector potential $\boldsymbol{E} = -\partial_t \boldsymbol{A}$) is applied and the resulting bulk supercurrent density profile is computed. We have verified that indeed both methods produce statistically equivalent results. The results shown in Fig. 5.5 are obtained via the direct method on a 60×60 cylindrical system. The data corresponds to the same temperatures as those in Fig. 5.4. The conductivity becomes roughly field-independent above a critical field, but continues to decrease with increasing temperature in this model. Since we have neglected the quasiparticle contribution here altogether, the results here can be thought of as the

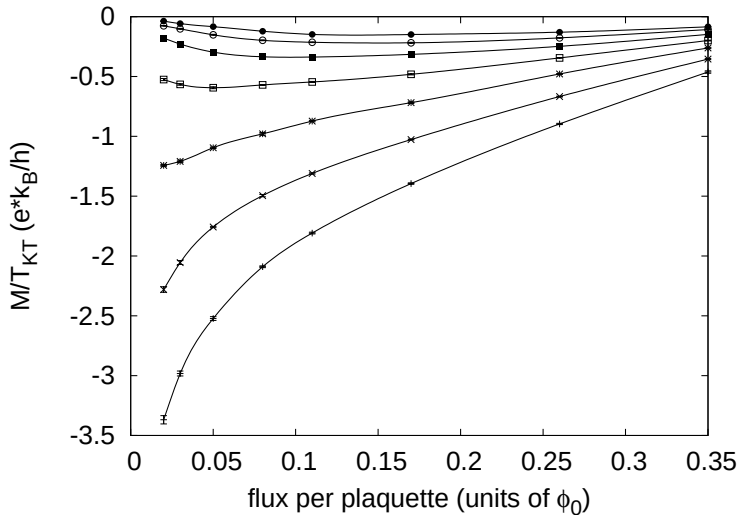

Figure 5.4: Magnetization measured in Langevin simulations of the frustrated XY model. The data is plotted for temperatures 0.5,0.75,1.0,1.25,1.5,1.75,2.0, in units of T_{KT}.

vortex contribution (i.e. "flux-flow") to the conductivity. A more accurate model will take into account quasiparticle dynamics. We note here that the conductivity depends rather sensitively on the choice of dynamics. Simulations of the XY model with RSJ dynamics, for instance, produce qualitatively different results with different finite-size scaling properties (see Ref. [23]).

We next turn to our principal transport quantity of interest, the transverse thermoelectric coefficient α_{xy} which describes the electrical response of the system perpendicular to an applied temperature gradient. By the Onsager relations, α_{xy} may also be determined by measuring the transport part of the heat current perpendicular to an applied electric field.

We have found that in the numerical simulations, measurements of α_{xy} and $\tilde{\alpha}_{xy}/T$ are equivalent within statistical noise. We have also found that the $\tilde{\alpha}_{xy}$ experiment produces a considerably higher signal-to-noise ratio. The same was found in simulations of the full TDGL equation having phase and amplitude fluctuations (including the quartic term) [42], as well as in the dual Coulomb gas approach to be described later on in the chapter. To measure α_{xy}, we again impose an electric field via the time variation of the vector potential along the axial direction of the cylinder, and we determine the transport part of the heat

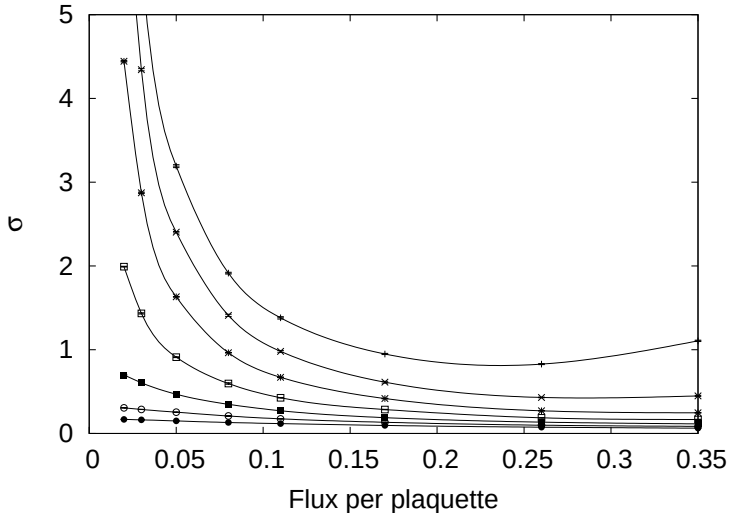

Figure 5.5:

currents which develop along the azimuthal direction under steady state conditions.

Figures 5.6 and 5.7 show the results for the 60×60 cylindrical system for temperatures below and above T_{KT} respectively. For temperatures below T_{KT}, α_{xy} appears to diverge logarithmically for low fields (it certainly vanishes at zero fields, as required, which is not presented here).

Above T_{KT}, however, this divergence disappears, as shown in Fig. 5.7. A signal which is statistically different than the noise persists in this model up to temperatures twice the Kosterlitz-Thouless transition temperature. Our simulations also show the characteristic asymmetry of α_{xy} (which is equivalent to the Nernst signal e_N up to a constant above T_{KT}, since the experimentally determined resistivities at these temperatures are roughly field independent), namely, that the signal rises sharply at low fields and decreases slowly after reaching its maximum value. Furthermore, the fields at which the maximum is reached (which Ong and collaborators refer to as the "ridge field" [69]) increases as a function of temperature, which is another feature visible in our simulations.

We see from our simulations then that the 2D frustrated XY model, a simple model for an extreme type II superconductor with an infinitely large pair-amplitude (but which lacks

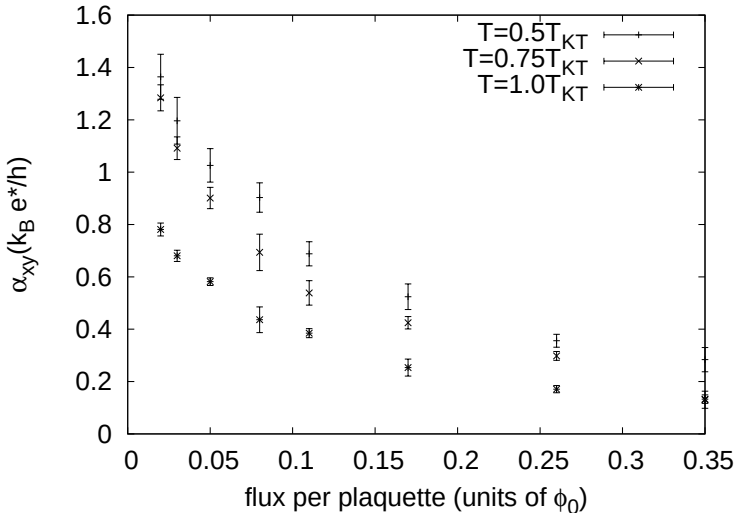

Figure 5.6: The transverse thermoelectric coefficient α_{xy} for a 60×60 cylindrical system at temperatures 0.5,0.75, and 1.0 in units of T_{KT}.

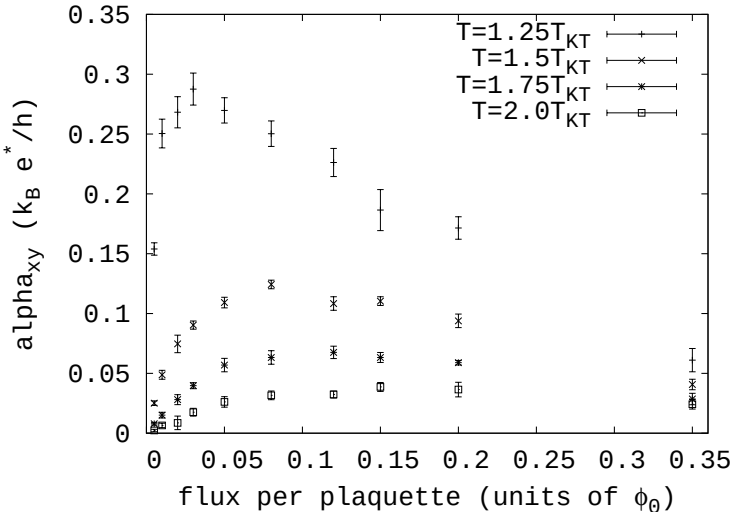

Figure 5.7: α_{xy} measured for temperatures above the Kosterlitz-Thouless transition temperature. The data shown corresponds to the temperatures 1.25, 1.5, 1.75, and 2.0 in units of T_{KT}. At temperatures as high as twice T_{KT}, a statistically significant value of the thermoelectric coefficient is detectable.

phase coherence) produces anomalously large transverse thermoelectric transport signatures well above the Kosterlitz-Thouless transition temperature. In the following section, we generate some analytical results which are consistent with our numerical simulations at high temperatures.

5.6 High temperature expansions

In this section, we derive analytical expressions for magnetization and α_{xy} at high temperatures. The high temperature expansion for magnetization is a standard exercise in statistical mechanics, whereas to compute α_{xy}, we recast the Langevin equation of motion into an effective action and generate high temperature expansions with this action. The conversion of a classical stochastic differential equation into an action principle was shown by Martin, Siggia, and Rose [40].

First, we consider the calculation of magnetization. By expanding the XY model partition function in powers of $K = J/k_B T$,

$$Z = \int D\theta \prod_{<i,j>} \left[1 - K \cos\left(\theta_j - \theta_i - A_{ij}\right)\right] \tag{5.32}$$

At leading order on a square lattice, the magnetic field dependence of Z will come from closed diagrams enclosing a single plaquette. Also, we see that the result is then gauge invariant since only the magnetic flux per plaquette enters the result. From the partition, one computes the free energy and the magnetization. The result is

$$\frac{M}{T} = -\frac{2\pi e^* k_B}{8h} K^4 \sin\frac{B}{B_{c2}} + O\left(K^6 \sin\frac{2B}{B_{c2}}\right), \tag{5.33}$$

where the correction comes from closed diagrams which enclose two plaquettes (and hence twice the flux).

To obtain a series expansion for α_{xy} in powers of K, we recast the Langevin dynamical equations of the XY model in terms of an effective Martin-Siggia-Rose [40] action, so that the expectation value of a dynamical variable X is computed as

$$\langle X[\theta_i]\rangle = \int D\theta_i \; X[\theta_i] \exp\left(-S_0[\theta_i] - S_1[\theta_i]\right), \tag{5.34}$$

where

$$S_0 = \frac{1}{4T\tau}\int dt \sum_i \left[\tau^2\dot{\theta}_i^2 + J^2\left(\sum_{j\in N.N.(i)} \sin\left(\theta_j - \theta_i - A_{ij}\right)\right)\right], \tag{5.35}$$

and

$$S_1 = \frac{J}{\tau}\int dt \sum_{<ij>} \cos\left(\theta_j - \theta_i - A_{ij}\right) \tag{5.36}$$

The high temperature expansion is done perturbatively in J, using the $J = 0$ action, which is gaussian in $\dot{\theta}$. We compute α_{xy} using the Kubo formula for an infinite plane. Note that the Kubo formula, which involves a dynamical correlation function, becomes a static quantity in the Martin-Siggia-Rose action, which is a space-time action. Again, at leading order in K, we pick up contributions from closed diagrams enclosing a single plaquette. The result using the Kubo formula for α_{xy} is

$$\alpha_{xy} = \frac{2\pi e^* k_B}{16h} K^4 \sin\frac{B}{B_{c2}} + O\left(K^6 \sin\frac{2B}{B_{c2}}\right) \tag{5.37}$$

Interestingly, at leading order, we find that the ratio

$$\frac{-M}{T\alpha_{xy}} = 2, \tag{5.38}$$

If the same analysis is repeated on a different lattice we do not get the same K-dependence for M and α_{xy}. For example, on a triangular lattice, $M/T \sim K^3$ at leading order, since the smallest closed diagram consists of three bonds. The same holds true for α_{xy} using the MSR action principle. This is not surprising; at temperatures much greater than the transition temperature, we do not expect to find universal results. But surprisingly, the ratio of $-M/T$ to α_{xy} remains the same. The reason for this robustness is not clear.

5.7 Dynamics and thermoelectric transport in the dual vortex model

In this section we study the Nernst effect in a dual representation in which vortex positions play the key role. Having understood diamagnetism and transverse thermoelectric transport signatures of the frustrated XY model, it may seem unnecessary to study the dual

version of this problem. However, in the XY model, the degrees of freedom are the local phases variables, and vortices are not at all invoked. By formulating the problem in a way that vortices play the primary role, we can gain further insight and learn how vortex parameters (core energy, entropy, etc) influence the Nernst effect. If the experiments do tell us something about vortex properties above the transition temperature, we will have a greater handle on a possible microscopic approach to the problem. Furthermore, although dual representations have been used to study equilibrium properties of the Kosterlitz-Thouless transition, it remains unclear whether both phase and vortex representations give rise to the same thermoelectric signatures in a magnetic field. That will be the task in the remainder of this chapter.

We consider the dual vortex representation of the XY model in which the vortices "live" on the sites of the dual lattice (see Fig. 5.8), and a dual electric field $\mathbf{e}$ is defined on the links of the dual lattice, by

$$\mathbf{e}(\tilde{\mathbf{x}}) = \nabla\theta(\mathbf{x}) \times \hat{z} \tag{5.39}$$

where the tildes are used to flag the dual sites. With this definition, the circulation of $\nabla\theta$ along a contour c in the original lattice translates to the outward flux of the dual field $\mathbf{e}$ across the boundary c, and therefore, the electric fields satisfy Gauss' law:

$$\Delta \cdot \mathbf{e} = 2\pi n_v \tag{5.40}$$

In this representation, the transverse part of the electric field represents the smooth spin wave deformations, whereas the longitudinal part is associated with vorticity.

The well known decoupling between spin wave and vortex degrees of freedom occurs in the Villain representation of the 2D XY model; the spin wave hamiltonian is gaussian, whereas the vortex excitations are described by a Coulomb gas model, as can be shown using standard manipulations (see Appendix (B.1):

$$\mathcal{Z} = \mathcal{Z}_{SW} \cdot \sum_{n(\boldsymbol{r})=-\infty}^{\infty} e^{-2\pi^2\beta J \sum_{\boldsymbol{r},\boldsymbol{r}'}[n(\boldsymbol{r})-b]V(\boldsymbol{r}-\boldsymbol{r}')[n(\boldsymbol{r}')-b]} \tag{5.41}$$

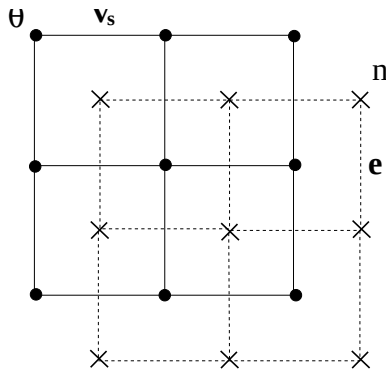

Figure 5.8: The phase variables θ_i are defined on the original lattice sites (denoted by closed circles), while $\nabla\theta$ and A_{ij}, the vector potential, are defined on the links (solid lines) of this lattice. In the dual 2D Coulomb gas model, the vortices and the static background charge density live on the dual lattice sites (marked by " $\times$"), whereas the electric fields live on the links (dashed lines) of the dual lattice. Vortices are associated with non-zero curls of the supercurrent and non-zero divergences of the dual electric fields.

Here, $V(r)$ is the inverse lattice propagator given in momentum space by

$$V(\boldsymbol{r}) = \rho_s \frac{2\pi}{L^2} \sum_{\boldsymbol{k}} \frac{e^{i\boldsymbol{k}\cdot\boldsymbol{r}}}{2\left(1 - \cos(k_x) - \cos(k_y)\right)}, \tag{5.42}$$

and at large distances, $V(\boldsymbol{r}) \sim \log(r)$. As shown in Appendix (B.1), b is the static background charge density on each dual lattice site and corresponds to the magnetic flux per plaquette of the XY model in the Villain approximation. The Villainized XY model is dual in this way to a 2D plasma of vortices + static background charge interacting logarithmically.

The equilibrium properties of the Coulomb gas model are well understood; at low temperatures, and zero applied fields (i.e. no background charge), the system is composed of tightly bound vortex-antivortex pairs forming a dielectric insulator and above the KT transition, free vortices begin to proliferate, converting the system to a mobile plasma of charges. The dynamics, and in particular, energy transport in this representation has proven to be more tricky. The reason for this is the decoupling of spin-waves and vortices in this Hamiltonian - precisely the same feature which makes static properties more tractable. The Coulomb gas Hamiltonian is purely electrostatic, and has no well-defined dynamics. We will see how to get over this issue later. As far as I know, there has not been any careful

treatment of thermal transport in this model.

A systematic treatment of the dynamics of the Coulomb gas was done in an influential paper by Ambegaokar, Halperin, Nelson, and Siggia (AHNS) [3]. We will now briefly review the essential points of this paper, using a somewhat more transparent approach.

AHNS were mainly interested in the electrical signatures of a mobile plasma of vortices in superfluid thin films. First, they considered the problem of driving the film substrate with a DC current. By computing the magnus force on a vortex due to its motion relative to the condensate and the drag force coming from the interactions of vortices with the underlying substrate, they were lead to a phenomenological Langevin equation for the motion of a vortex:

$$\dot{\boldsymbol{r}}_i = \Gamma n_i \boldsymbol{e}(\boldsymbol{r}_i) + \boldsymbol{\eta}_i, \tag{5.43}$$

where $\boldsymbol{r}_i$ are the coordinates of the vortices, $\boldsymbol{e}$ is the dual electric field, $\boldsymbol{\eta}$ a noise term coming from the interactions with the bath, and Γ is an effective diffusion constant. They showed that an externally applied DC electrical current is related to an *external* dual electric field acting on the vortices in the direction *perpendicular* to the applied electrical current (the supercurrent is given in terms of the *local* electric field - see Eq. 5.39 .

In addition to this, we have the Josephson relation, which connects a DC electric field to a current of vortices perpendicular to the electric field:

$$\boldsymbol{E} = \phi_0 \hat{z} \times \boldsymbol{j}_v, \tag{5.44}$$

where j_v is the vortex current density.

Taken together, the Josephson equation and the definition of the dual electric field state that electric(vortex) currents are related to dual(electrical) voltages in the *perpendicular* direction:

$$\begin{pmatrix} \mathbf{J} \\ \mathbf{E} \end{pmatrix} = \begin{pmatrix} 0 & \rho_s \epsilon \\ \phi_0 \epsilon & 0 \end{pmatrix} \begin{pmatrix} \mathbf{j} \\ \mathbf{e} \end{pmatrix} \tag{5.45}$$

where

$$\epsilon = \begin{pmatrix} 0 & -1 \\ 1 & 0 \end{pmatrix} \tag{5.46}$$

is the unit antisymmetric matrix in the xy plane and to avoid confusion, we have used upper and lower case letters to refer to the electrical and dual quantities, respectively .

Armed with this insight, we can relate transport coefficients in the phase representation considered above to those in the vortex model.

Just as we did with the XY model, we can write down linear response equations for the vortex transport coefficients:

$$\begin{pmatrix} \boldsymbol{j} \\ \boldsymbol{j}_Q \end{pmatrix} = \begin{pmatrix} \sigma^v & \alpha^v \\ T\alpha^v & \tilde{\kappa}^v \end{pmatrix} \begin{pmatrix} \boldsymbol{e} \\ -\nabla T \end{pmatrix} \tag{5.47}$$

Of course, the heat current remains invariant under the duality transformation, since the same quantity is expressed in terms of different variables (note also that in the 2D Coulomb gas model, the temperature is not inverted with respect to the original Villain model - see Appendix B.1). We will discuss the energy current shortly.

While it is interesting to consider all possible relationships between various transport coefficients, we shall focus on the vortex representation of σ and α_{xy}, which we have studied above using the XY model. We shall again use the approximation that the Hall angle is zero, which amounts to the condition that the only non-zero electrical transport coefficients are $\sigma_{xx} = \sigma_{yy} = \sigma$ and $\alpha_{xy} = -\alpha_{yx}$.

We consider a system in which, for simplicity, the temperature gradient is along the x-direction. In the electrical language,

$$J^x = \sigma E^x \tag{5.48}$$

and

$$J^y = \sigma E^y + \alpha_{yx}(-\nabla^x T) \tag{5.49}$$

In the vortex representation, this translates to

$$\rho_s e_y = \phi_0 \sigma j_y \tag{5.50}$$

$$\rho_s e_x = \phi_0 \sigma j_x - \alpha_{xy}(-\nabla_x T) \tag{5.51}$$

written in a more conventional way,

$$j_x = \frac{\rho_s}{\sigma\phi_0} e_x + \frac{\alpha_{xy}}{\phi_0\sigma}(-\nabla_x T) \tag{5.52}$$

$$j^y = \frac{\rho_s}{\sigma\phi_0} e^y \tag{5.53}$$

From this, we read off the transport coefficients:

$$\sigma^v = \frac{\rho_s}{\sigma\phi_0} \tag{5.54}$$

and

$$\alpha^v_{xx} = \frac{\alpha_{xy}}{\phi_0\sigma} \tag{5.55}$$

Therefore, the Nernst signal, defined in Eq. 5.1 has a particularly simple form in the vortex representation:

$$e_n = \phi_0 \alpha^v_{xx} \tag{5.56}$$

It is important to stress here that the Nernst signal written in this language involves diagonal parts of transport coefficients. In the following sections, we compute these conductivities in Monte Carlo simulations of the 2D coulomb gas model.

Next we consider the problem of formulating the energy current in the vortex model. Clearly, we cannot work with the Coulomb gas Hamiltonian written in terms of the logarithmic interaction between vortices. Since the spin waves have been integrated out in this model, energy moves instantaneously over large distances each time a vortex moves about. We shall instead use the local formulation of the Coulomb gas involving electric fields which are constrained to obey Gauss' Law.

In addition, we need some dynamical rules that govern these electric fields. The analogy between vortex dynamics and electrodynamics was also given in AHNS [3]. Motivated by third sound (i.e. spin wave) experiments, AHNS considered the case where the local superfluid density (integrated across the film thickness) was a dynamical variable (local deviations in film thickness) along with the phases. In this case, one arrives at the Hamiltonian version of the XY model

$$\mathcal{H} = \frac{1}{2C}\sum_r n_r^2 - J\sum_{ij}\cos(\Delta\theta), \tag{5.57}$$

where n_i is the local superfluid density, related to the local film thickness, and is conjugate to the phase variables ϕ. AKNS were then able to motivate phenomenologically the analogy with electrodynamics by viewing n_i as a magnetic field in the direction perpendicular to the film (a scalar in 2D), considered $\nabla\theta \times \hat{z}$ to be an electric field, while the vortices acted as ordinary charges [3].

In the Hamiltonian XY model, spin waves and vortices are no longer decoupled. Using this analogy with the Maxwell equations, it must follow that the energy current is simply the Poynting vector. To make contact with the Coulomb gas, we ought to consider the limit in which the speed of light is much larger than the characteristic diffusive vortex currents. We will now describe the local model with energy currents which will be used for the numerical simulations of the 2D Coulomb gas.

5.8 Model Hamiltonian, equilibrium and dynamics

As argued above, we will need to abandon the logarithmic electric potential of the 2D Coulomb gas in favor of local electric fields that are constrained by Gauss' law. Using Gauss' law, we write the partition function above in terms of the electric fields, namely

$$\mathcal{Z} = \int D\boldsymbol{e}_l D\boldsymbol{e}_t \prod_{\boldsymbol{r}} \delta(\Delta \cdot \boldsymbol{e} - 2\pi n(\boldsymbol{r})) e^{-\beta U} \tag{5.58}$$

where $\boldsymbol{e}_t$ and $\boldsymbol{e}_l$ are respectively, the transverse and longitudinal parts of the electric field, and

$$U = \sum_{i \in \text{ links}} e_i^2/(4\pi) \tag{5.59}$$

The Villain decoupling of spin waves and vortices is easily seen as well in the expression above. Writing $\mathbf{e} = \mathbf{e}_l + \mathbf{e}_t$, letting

$$\boldsymbol{e}_l = \nabla\phi \tag{5.60}$$

and

$$\boldsymbol{e}_t = \nabla \times \boldsymbol{a} \tag{5.61}$$

(where $\boldsymbol{a}$ is an analytic vector function, and ϕ is a scalar field obeying the 2D Poisson equation), we can immediately see that

$$\int d^2 r e^2 = \int d^2 r \left(e_l^2 + e_t^2 \right) \tag{5.62}$$

since the cross-term $\int d^2 r \mathbf{e}_l \cdot \mathbf{e}_t = 0$, which can be shown using an integration by parts. Written this way, the formulation is equivalent to a $U(1)$ non-compact lattice gauge theory, (the electric field link variables can take any real value consistent with Gauss' law) and we will use this representation in our numerical simulations.

We will now describe our method of sampling this partition function in Monte Carlo simulations. We consider a 2D square lattice whose sites contain charges corresponding to the superconductor vortices. The links of the lattice contain electric fields. Our Monte Carlo consists of two basic and simple moves. In the first move, a bond is chosen at random on the lattice, and a vortex/anti-vortex pair is placed on the link with some randomly chosen moment (a Z_2 choice for each bond). In order to satisfy Gauss' law, we insert an electric flux $e = 2\pi$ on the link directed from the vortex to the antivortex. The move is accepted or rejected based on the Metropolis criterion with the Hamiltonian

$$\mathcal{H} = \frac{1}{4\pi} \sum_i e_i^2 \tag{5.63}$$

In the second move, a plaquette is chosen at random, and a random electric curl is added to the plaquette. Similar simulations have been considered in a soft condensed matter context[37]; the authors of this work have established that these moves alone are sufficient to equilibrate the system and to yield the correct thermodynamic quantities. The simulation proceeds by randomly interpolating between these two moves, and a single Monte Carlo time step passes when each bond and plaquette has experienced a move. 10^6 time steps are used for equilibration and 10^7 steps for computing averages.

We start with simulations done on a torus for which the total charge must always remain at zero. We consider both the neutral plasma and the one-component plasma in which there are more vortices than there are anti-vortices, due to an applied magnetic field. In

the neutral case, the system is initialized to a vacuum containing neither fields nor charges, and the moves above are attempted. In the non-neutral case, we place a static background charge on each lattice site and work with a fixed net vorticity $n_+ - n_-$ given in terms of the magnetic induction (and must cancel the background density to maintain net neutrality)

$$n_+ - n_- = B/\phi_0. \tag{5.64}$$

The simulations of the one-component plasma, are initialized with a fixed number of vortices, a neutralizing background is added to the lattice, and the electric fields are initialized in a way such that Gauss' law is satisfied on each site. The simulation then proceeds identically to the case of the neutral plasma.

5.8.1 Helicity Modulus and the KT transition

We first consider the neutral case and measure the Kosterlitz-Thouless transition temperature. Since this has not been done using this approach in the past, we describe our method.

A rough estimate of the KT transition temperature is given as usual from free energy considerations. We use the superfluid hamiltonian (set $\hbar = m = 1$), and consider the free energy cost of introducing an isolated vortex (the energy associated with creating a vortex in 2D diverges logarithmically with system size, but the configurational entropy associated with placing the vortex somewhere on the lattice also diverges logarithmically): $F = (\pi\rho_s - 2T)\log(R)$, where R is the system size. Thus for $T > \pi\rho_s/2$, vortex proliferation is favored by the entropy term. This is a quick (yet reasonably accurate) estimate of the KT transition temperature. Comparing the electric field hamiltonian to the superfluid hamiltonian, we see that in the electric field language, $\rho_s = 1/2\pi$, and therefore, we expect to see the transition to occur near $T = 0.25$.

An important quantity in the study of the KT transition is the helicity modulus Υ, (which involves ρ_s^R, the *renormalized* spin wave stiffness), and which describes the rigidity of the XY model (or the equivalent superfluid film) to an externally imposed uniform twist in the system [18]. We have used the helicity modulus also for the XY model, but now, we reinterpret its physical meaning in terms of vortex parameters.

More specifically, considering for the moment the superfluid language, the helicity modulus is defined as the difference in free energy of a system with imposed twist (i.e. a uniform superfluid velocity) and one without the twist:

$$\mathcal{F}(\mathbf{v}) - \mathcal{F}(0) = \frac{1}{2}\rho_s^R v^2 \tag{5.65}$$

As vortices begin to proliferate, the system loses its rigidity to externally applied twists and the helicity modulus falls to zero; i.e. vortices reduce the effective superfluid stiffness. For the Villain model, the expression for the helicity modulus is

$$\Upsilon \equiv \frac{\rho_s^R}{\rho_s} = 1 - \lim_{q\to 0} \frac{\rho_s}{T} \frac{\langle m(\mathbf{q})m(-\mathbf{q})\rangle}{q^2} \tag{5.66}$$

Where the second term involves the vortex density correlation function. As we have done with the XY model, we look for the universal jump in the helicity modulus [44] from the value zero just above the transition temperature to the value $(2/\pi)T_c$ just below it. This is the primary diagnostic we use to detect the KT transition.

In the language of the 2D Coulomb gas, the helicity modulus is the zero wave-vector component of the inverse capacitance (or more precisely the inverse permittivity), which represents the system's rigidity against externally imposed electric fields. At low temperatures, the system behaves either as a vacuum or as an insulator containing tightly bound +/- pairs and the system has a large inverse capacitance. As the vortices become unbound and mobile, they screen externally applied voltage, and the system behaves as a metal with zero inverse capacitance. The expression for the inverse permittivity is exactly the one given above in eq. 16.

To compute the helicity modulus above, one needs to measure the vortex density, compute its Fourier transform, and extrapolate to $q = 0$, which is hardly accurate on smaller lattices. However, it is possible to measure this quantity entirely in real-space, as we now discuss.

The key quantity that renormalizes the inverse permittivity are zero wave vector voltage fluctuations which, on a torus, represent "winding number" excitations in which a +/- pair

created next to one another, migrate around the torus, and and annihilate, leaving behind a voltage $V = 2\pi$.

These winding number excitations are equivalent to long wavelength polarization modes which are most effective in screening externally applied voltage and gives the system its metallic character. The second term in eq. 16 can be recast in terms of the total winding number after expanding it in a multipole expansion (the leading term is the dipolar contribution).

$$\epsilon^{-1}(0) = 1 - \frac{\langle E_{\rm tot}^2 \rangle}{4\pi T L^2} \tag{5.67}$$

where

$$E_{tot}^a = \sum_{\mathbf{r}} E_{\mathbf{r}}^a \tag{5.68}$$

Figure 5.9 shows the measured values of the helicity modulus ϵ^{-1} for various system sizes.

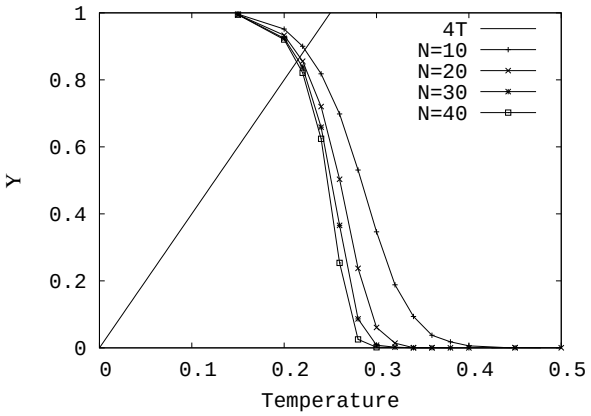

Figure 5.9: The helicity modulus, which marks the onset of the KT transition, is equivalent to the long wavelength part of the inverse dielectric tensor in the Coulomb gas representation of the XY model. Shown here are the helicity moduli measured using eq. 17 for four different sample sizes on a torus (N by N square lattices).

The drop in the helicity modulus at a temperature near 0.25 is consistent with the crude prediction made earlier. The curves clearly show the universal jump phenomenon and unmistakably identifies the KT transition.

To analyze further the static properties of the KT transition using the local MC algorithm, we have measured the specific heat. According to KT theory, there is an essential

singularity in the specific heat at the critical temperature which is followed by a large, non-universal peak above Tc, which occurs due to the entropy liberated by the mobile charges [9]. While the essential singularity is weak and cannot be seen in numerical simulations of finite size systems, we have observed the peak in the specific heat above Tc.

5.8.2 Cluster updates and the vortex depletion layer

As it stands, the simulations described above suffer from two difficulties. First, the MC move which involves creating a vortex-antivortex pair in conjunction with an electric flux update along a *single* link results in enormous string tensions. This dramatically suppresses vortex mobility and causes artificial pinning. This is especially a problem at temperatures near and below T_{KT}, which is also the regime of interest. Due to this artificial pinning, the dynamics are severely affected.

A second problem with this approach is that the vortices were never allowed to leave or enter the system. In retrospect, it seems quite clear that the magnetization described in the previous sections must be caused by an equilibrium vortex depletion near the boundary of the superconductor. The intuitive picture is as follows. First, there is the externally applied magnetic field, which, in the dual language translates to the gauge-invariant static background charge density. Second, there is a net repulsion between two vortices of like charge. As the magnetic flux density increases, the background charge more strongly attracts its mobile vortices, and the system approaches the state of net neutrality (vortex density + background density = 0) i.e. 0 magnetization. If the applied fields are low, however, there is a slight net vorticity, these charges feel each other (at low temperatures) via the logarithmic interaction, but they don't feel strongly attracted to the background. Thus, by leaving, the vortices can dramatically lower the free energy of the system. At higher temperatures, screening kills off this effect.

By looking into the XY model with Langevin dynamics, we have gained considerable insight into the problem. In particular, the compactness of the phases solve both problems above with ease - it is effortless for vortices (defined modulo 2π) to move about and to

exit/enter the system with open boundaries.

To obtain a similar situation in the dual system, we have implemented a more non-local cluster update instead of the single link update described above. We found that cluster updates on a 3x4 patch of the lattice enhance mobility down to $T = 0.5T_{KT}$, even at the lowest vortex densities.

The cluster updates dramatically suppresses string tension and enhances mobility. The MC move proceeds as follows: vortex-antivortex pairs are still placed at nearest neighbor sites of a lattice (we call the bond connecting these two sites the "principal bond" (see Fig. 5.8.2). First, we randomly pick a principal bond along which the charges are to be potentially placed. Next, we determine the appropriate 3×4 cluster associated with this bond, and consider placing a set of electric fields on this cluster which satisfy Gauss' law and have zero curl on each plaquette (as it turns out, this is a unique configuration which minimizes the energy). The move is accepted by the standard Metropolis criterion, and if accepted, the entire cluster is updated.

Next consider a system with finite boundaries. See Figure 5.10. We shall define the boundary between the superconductor and the vacuum to live along a bond: on the superconducting side, the bond terminates on a site which obeys Gauss' law, and on the opposite side, the bond ends in a site where charge is not defined, and Gauss' law makes no sense (see Fig. 5.10). To get the physics of charges leaving and entering the system, we again make use of cluster moves as described above. The only new feature now, is that if some part of the cluster happens to lie outside the system, the electric fields which would have been placed there are not taken into account in the Metropolis weighting, and if the move is accepted, only *internal* sites are updated. Clearly, such moves are enhanced near the boundary (in the physical system this is also true due to the reduction of the superfluid density along the boundary). If a charge is created outside the system, it is annihilated, and Gauss' law is neglected on the external sites (see Fig. 5.11).

To check whether the cluster updates are an improvement as far as pinning goes, over the local updates, we consider the (dual) voltage auto-correlation function in a system with

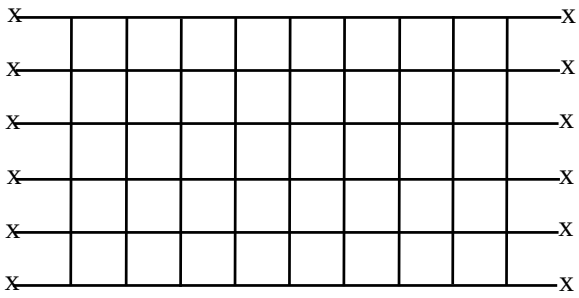

Figure 5.10: The geometry which permits vortices to enter and exit the system. The X's mark sites which are external to the system but are connected via a bond to the superconductor. If a charge happens to be generated on these sites, it is immediately annihilated.

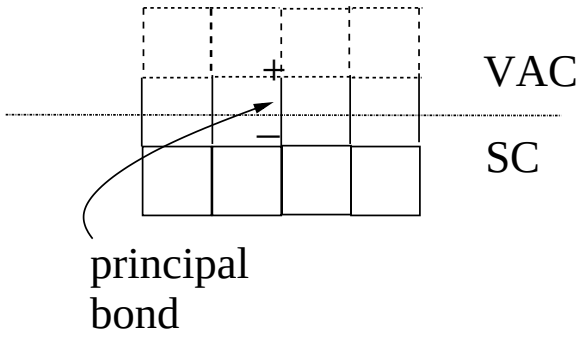

Figure 5.11: The cluster move near a boundary. Here, the dotted lines represent parts of the cluster which are in the vacuum, and these links are neither considered in the Metropolis function, nor are they updated if the move is accepted. in this case, if this move is accepted, the + charge will be destroyed before proceeding, leaving behind the - charge inside the system. This is the charge depletion layer and is the dual perspective of diamagnetism.

periodic b.c.

$$\langle V_x(0)V_x(t)\rangle = A\exp\left(-t/\tau\right) \tag{5.69}$$

In particular, we look at the autocorrelation time τ, which tells us how long (in units of MC time) it takes for two configurations to be completely uncorrelated. This is directly related to the mobility of vortices - the larger the autocorrelation time, the more sluggish the vortices move (if at all).

It is clear that string tension plays less important a role as the density of vortices increase: imagine pulling two vortices apart, and if a third one intercepts the string, the tension is immediately relieved.

We have studied the autocorrelation time at the lowest vortex densities (magnetic fields) as a function of temperature. We have found that by going from the link to the cluster, we have gained at least a factor of 2 in temperature. At such low magnetic fields, we can reasonably go down to as low as $T = 0.6T_{KT}$ using this method without any error. Below this, however, we again fall into trouble. This trouble quickly disappears when we increase the magnetic flux density.

Having set up this numerical apparatus, we now make use of it to determine the Magnetization of the superconductor. We consider the cylindrical geometry of Fig. 5.10. Deep inside the cylinder, beyond say a distance X_0 from the edge, the system is essentially neutral: the background charge density cancels the vortex density on average. The supercurrents also vanish deep inside the system at equilibrium. Recall from above that the magnetization can be obtained by looking at the edge supercurrents (take $x = 0$ to be the boundary):

$$M = \int_0^{X_0} dx\langle J^y(x,y)\rangle = \rho_s \int_0^{X_0} dx e_x \tag{5.70}$$

By Gauss' law,

$$M = 2\pi\rho_s \int_0^{X_0} dx x\left(\langle n(x) - b\right), \tag{5.71}$$

which means that the magnetization is really just the surface polarization density in the charge depletion region near the edge of the cylinder. This quantity is measured in equilibrium simulations and indeed, we see obtain the magnetization which resembles the results

obtained from the frustrated XY model. Figure 5.12 shows the magnetization for a 20×20 cylinder for temperatures $T = 0.9$, 1.0,1.25,1.5,1.75, 2.0 in units of T_{KT}. We see the separatrix near the transition temperature below which the magnetization diverges logarithmically at low fields, and above which it vanishes in that limit. Had we not permitted vortices

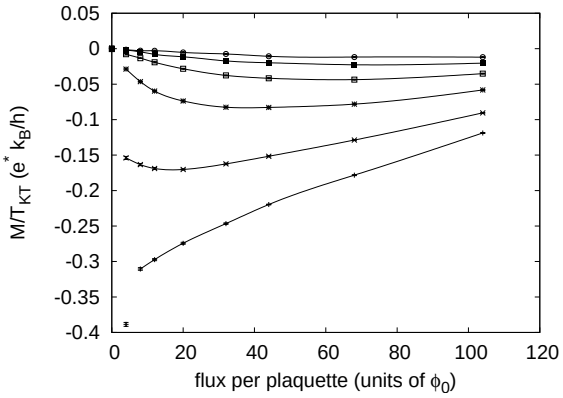

Figure 5.12: The magnetization determined by measuring the equilibrium surface polarization in the vortex model. We have permitted charges to escape, and have made use of cluster updates. Temperatures shown correspond to $T = 0.9, 1.0, 1.25, 1.5, 1.75, 2.0$ in units of T_{KT}. The measurements have been made on a 20×20 cylinder. Any discrepancies with the results from the XY model considered earlier are finite size effects.

to enter and exit the system, we would not have been successful in computing the magnetization. Having gained some confidence from the statics, we next turn to the problem of computing dynamics using this model.

5.8.3 Dynamics: preliminary results

The Monte Carlo metropolis dynamics will now be employed to compute α_{xy}. First, we define our currents. In this model, we have three types of currents: supercurrents, vortex currents, and the energy current. The supercurrents are defined in terms of the dual electric fields, as we have discussed. It is also straightforward to define a vortex current in our problem. Consider the MC move in which a vortex-antivortex pair is created at two nearest neighbor sites. This move is equivalent to one in which a single vortex moves along the link. Thus, each time we create a vortex anti-vortex pair, we generate a vortex current pulse in

the system. We must divide by the value of the time step (i.e. the conversion from MC time to real time) in order to have the proper dimensions.

To define the energy current, we recall our earlier discussion on the analogy with Maxwell equations. When a vortex moves, the spin waves will transmit its energy across the system, precisely the way the photon fields transmits energy and momentum along large distances of a charge in motion. With this in mind, we define a local heat bath, associated with each plaquette center. In Fig. 5.13, we label the 4 electric fields $e_1 \cdots e_4$, and change the circulation by an amount δ. Using the expression for the local energy density $u_i = 1/4\pi e_i^2$, we see that the energy change associated with each link are $\delta u_i = e_i \delta e/2\pi + O(\delta e^2)$, for $i = 1, 2$, and $\delta u_i = -e_i \delta e/2\pi + O(\delta e^2)$, for $i = 3, 4$. When this plaquette is updated,

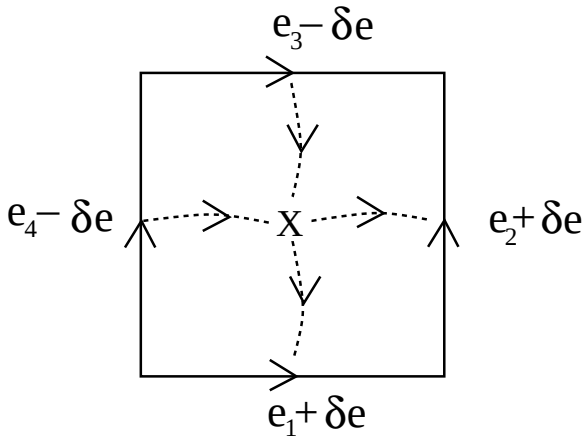

Figure 5.13: The local energy current used in our simulations. The arrows depict the flow of energy from the center of the plaquette (local heat bath) to the bonds. We have used a convention for the flows in which each of the electric fields are positive.

a pulse of energy $\delta e e_i/2\pi$ travels from the local bath to bond i. The signs of the energy current are shown in Fig. 5.13. The $O(\delta e^2)$ terms do not contribute to the current - they each travel away from the bath to the bonds and their sum cancels. If we did not associate the bath with the plaquette centers, these terms would not cancel - the statement of *linear* response, then, is to associate the baths with the plaquette centers. As we did for the vortex currents, we divide the energy pulses by the value of the time step to define the current properly. In both cases, the choice of the time step is made such that there is agreement in

the transport coefficients between the Kubo formulae and externally applied gradients in the linear response regime.

A more careful look at the expression for the energy current shows that it is closely related to the energy currents in the Langevin equation. The plaquette is the precise dual analog of updating an angle in the XY model: upon identifying $\delta e/\tau$ with $\dot{\theta}$ (τ is the value of the time step), and using the definition of e_i in terms of the gauge invariant phase angle differences, we see that this form of the energy current is the dual version of the expression used in the Langevin simulations of the XY model above. Using the definition of the currents above, we have verified the Onsager relations both for the supercurrents and for the vortex currents. We have also verified that the Kubo formulae and the direct external applied field methods produce the same transport coefficients to within statistical error.

There is a subtlety associated with the Onsager relations here that is worth mentioning. With this model, we can pass both steady state (dual) voltages and currents, and the results depend on which external perturbation is used. First we consider imposing a steady state vortex current in the system. Since Gauss' Law $\boldsymbol{\Delta} \cdot \boldsymbol{e}(\boldsymbol{r}) = 2\pi n(\boldsymbol{r})$ is strictly conserved in our simulations, we find by differentiating both sides with respect to the time step τ, and by using the equation of continuity for the vortex density (in the bulk of the system) that

$$\boldsymbol{j} = \frac{\delta \boldsymbol{e}}{\delta \tau} \tag{5.72}$$

Thus, to impose a steady-state vortex current, we increase the value of every electric field $\boldsymbol{e}$ by an amount $\boldsymbol{j}$ at each time step. Care must be made to ensure linear response. By doing this, we are actually applying a DC *electric field* $\boldsymbol{E}$ in the system. When we measure the steady-state energy current, we obtain α_{xy}.

We can also apply an external dual electric field $\boldsymbol{e}_{ext}$ to the system. We do this in the simulations by adding a term $\delta U = \boldsymbol{e}_{ext} \cdot \boldsymbol{P}$ to the moves which create a vortex anti-vortex pair, where $\boldsymbol{P}$ is the dipole moment associated with the created pair. By doing this we drive the vortices in the direction of $\boldsymbol{e}_{ext}$. When we measure the steady state energy current with this probe, we determine the *Nernst signal*, not α_{xy}. This can be seen from the phenomenological transport relations for the dual vortex currents. Notice here, that

the measurement of α_{xy} is independent of the choice of τ, as we found in the XY model: both the external probe, namely the electric field $\boldsymbol{E}_{ext}$, and the energy current are inversely proportional to τ, and α_{xy}, their ratio, is independent of it. However, if we applied an external dual electric field $\boldsymbol{e}_{ext}$, which is independent of τ, we measure the Nernst signal e_N, which is inversely proportional to τ (recall that the electrical conductivity $\sigma \propto \tau$). Therefore, there are two sets of Onsager relations:

$$\tilde{\alpha}_{xy} = T\alpha_{xy}, \tag{5.73}$$

and

$$\tilde{\alpha}^v = T\alpha^v, \tag{5.74}$$

where $\alpha^v = \alpha^v_{xx} = e_N/\phi_0$. The latter set of relations represent the correspondence between the Nernst and Ettinghausen effects.

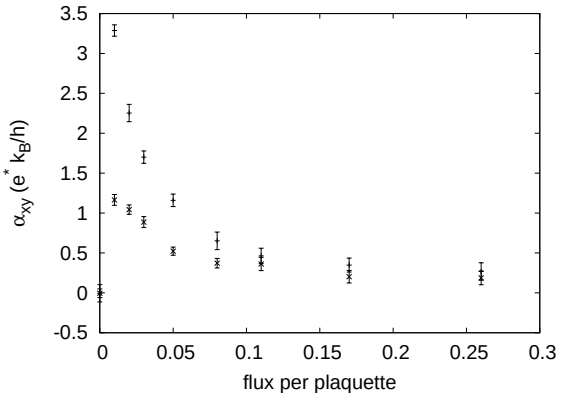

Figure 5.14: Measurements of α_{xy} made on a 20×20 cylinder at $T = 0.9, 1.0$ (in units of T_{KT}). We have applied an electric field $\boldsymbol{E}$ along the axis of the cylinder (or equivalently, we have driven a vortex current $\boldsymbol{j}$ in the azimuthal direction), and measured the heat current in the azimuthal direction. Results resemble those from the XY model simulations, except for finite size deviations, which are substantial.

To illustrate this, we have done simulations on small system sizes where we have measured the heat current in response to applied electric fields $\boldsymbol{E}_{ext}$ (Fig. 5.14), and dual electric fields $\boldsymbol{e}_{ext}$ (Fig. 5.15). Both simulations are done at the same temperatures ($T = 0.9, 1.0$, in units of T_{KT}. Indeed, we find that whereas the former experiment gives us α_{xy}, the latter

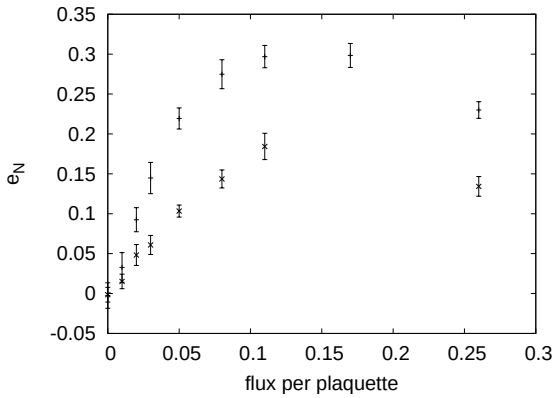

Figure 5.15: Using the same geometry as in Fig. , we apply an external dual electric field $\boldsymbol{e}_{ext}$, along the azimuthal direction which drives the vortices along this direction. We measure the heat current in the azimuthal direction in response to this perturbation, which yields α^v, a quantity that is proportional to the Nernst signal. The units are arbitrary, depending on the choice of time step. The temperatures are $T = 0.9, 1.0$ (units of T_{KT}).

generates e_N. We have thus established all the necessary features to determine α_{xy} more systematically. This shall be the task for the immediate future.

5.9 Future Work

Having established the fact that the frustrated XY model and the dual Coulomb gas system (with the appropriate background charge density) can be used to explain the large thermoelectric and diamagnetic response in an extreme type II superconductor, we now briefly mention work currently underway. First, with the 2D coulomb gas model, we shall generate results for α_{xy} using larger system sizes to compare with results from the TDGL simulations of the frustrated XY model. Having studied this correspondence, we plan on studying the effect of a vortex core energy, and the effects of internal vortex states (which is implemented by choosing a temperature dependent core energy) on α_{xy}. One of the important issues here that remains to be explored is the connection between α_{xy} and the entropy per vortex. With our simulations, we will be able to answer these questions.

Appendix A

Appendix to Chapter 3

A.1 Derivation of spinor Hamiltonians of Section 3.5: the standard approach

Here, we present a derivation of the results of Section 3.5 using a more standard approach, one which perhaps might be more familiar to the reader.

Analogous to the "nearly-free electron" approach to electronic band structures, a weak periodic perturbation in the dielectric properties of a medium is considered in the nearly-free photon approach, the Maxwell normal mode problem is solved for bloch state solutions in this medium, and corrections to the zeroth order, free photon dispersion relations are obtained in special regions of interest in the brillioun zone. Our attention shall be restricted to a case in which the weak periodic "potential" forms a two dimensional hexagonal lattice. In what follows, the lattice spacing shall be set to unity.

Fig. 3.15 depicts the hexagonal Brillouin zone. In the uniform case in which the constit utive relations are $\epsilon_{ab}^{-1} = \delta_{ab}\epsilon_0^{-1}$ and $\mu_a^{-1}{}_b = \delta_{ab}\mu_0^{-1}$, there is a 3-fold degeneracy at the zone corners.

We shall study the dispersion in the vicinity of these points when a weak periodic modulation is added to to the zeroth order constitutive relations above:

$$\epsilon_{ab}^{-1} = \epsilon_0^{-1}\delta_{ab} + \sum_{\mathbf{G_i}} \epsilon_{ab}^{-1}(\mathbf{G_i}) \tag{A.1}$$

The sum in the second term above is over the three reciprocal lattice vectors shown in Fig. 3.15. We will need to consider off-diagonal anisotropy in the permittivity tensor when we introduce the Faraday coupling to break T (this will be done in the follwing subsection). We will not need to modify the permeability.

We solve the Maxwell normal-mode problem, written in the very standard "Schrodinger" form,

$$\boldsymbol{\nabla} \times \left(\epsilon^{-1}(\boldsymbol{r})\boldsymbol{\nabla} \times \boldsymbol{H}(\boldsymbol{r})\right) = \omega^2 \boldsymbol{H}(\boldsymbol{r}), \tag{A.2}$$

for Bloch state normal modes.

We restric attention to 2D, and make use of the fact that in this case, the full 6×6 Maxwell eigenproblem decouples into two 3×3 ("TE" and "TM") problems. We focus on the TE modes, for which the set (E_x, E_y, H_z) are the degrees of freedom. We will consider the dispersion in the vicinity of the zone corners first for the case in which both T and I are present. Then, we will consider the effect of breaking T.

When time-reversal symmetry is present, the eigenproblem is (focusing on in plane propagation)

$$\epsilon_0^{-1}\left(|\boldsymbol{k}|^2 - \frac{\omega^2}{c_0^2}\right) H_z(\mathbf{k}) + \sum_{\mathbf{G}} \epsilon_{\mathbf{G}}^{-1}\mathbf{k}\cdot(\mathbf{k}-\mathbf{G})\,\mathbf{H_z}(\mathbf{k}-\mathbf{G}) = \mathbf{0} \tag{A.3}$$

Focusing on the vicinity of the zone corners, and defining $\delta\boldsymbol{k}_i = \boldsymbol{k} - \boldsymbol{K}_i$, we consider the degenerate perturbation theory problem where the three plane wave modes near the zone corners mix (i.e. a "nearly-free photon" approximation). Setting each Fourier modes of the inverse permittivity equal to one another, $\epsilon_{\boldsymbol{G}_i}^{-1} = \epsilon_1^{-1}$ (which is a real quantity, since time-reversal symmetry is not broken at this point), we obtain a 3 by 3 real- symmetric eigenvalue problem, which in the basis $\boldsymbol{x} = (H_z(\delta\boldsymbol{k}_1), H_z(\delta\boldsymbol{k}_2), H_z(\delta\boldsymbol{k}_3))$, is an equation

$A\boldsymbol{x} = \omega^2 \boldsymbol{x}$, where

$$A = \begin{pmatrix} k_1^2 & \lambda \boldsymbol{k}_1 \cdot \boldsymbol{k}_2 & \lambda \boldsymbol{k}_1 \cdot \boldsymbol{k}_3 \\ \lambda \boldsymbol{k}_2 \cdot \boldsymbol{k}_1 & k_2^2 & \lambda \boldsymbol{k}_2 \cdot \boldsymbol{k}_3 \\ \lambda \boldsymbol{k}_3 \cdot \boldsymbol{k}_1 & \lambda \boldsymbol{k}_3 \cdot \boldsymbol{k}_2 & k_3^2 \end{pmatrix}, \tag{A.4}$$

where $\lambda = \epsilon_0 \epsilon_1^{-1}$.

The solutions to this problem are easily obtained. Exactly at the zone corners, there is a non-degenerate state, corresponding to the uniform superposition of the three plane waves, having eigenfrequency $\omega_0 = c_0 |\boldsymbol{K}| (1 - \lambda/2)$. In addition, there are two degenerate states with frequency $\omega_D = c_0 |\boldsymbol{K}| (1 + \lambda/4)$. The states belonging to these eigenfrequencies correspond precisely to those in Eq. 3.82.

The nearby ($\delta \boldsymbol{k} \neq 0$) are also readily obtained. One finds that the non-degenerate mode is unaffected to leading order (it disperses quadratically), whereas the doublet states have linear dispersion

$$\omega_\pm = \omega_D \pm \boldsymbol{v}_D \cdot \delta \boldsymbol{k}, \tag{A.5}$$

where $v_D = c_0/2 + O(\lambda)$ is the Dirac velocity. This is our Dirac point.

Next, we break time-reversal symmetry by introducing imaginary off-diagonal elements (Faraday coupling) in the inverse permittivity tensor.

We shall keep the diagonal elements of the inverse permittivity the same as before, and we shall consider only purely imaginary off-diagonal elements. Namely, let $\epsilon'_{\mathbf{G}}$ correspond to the Fourier component of the Faraday coupling:

$$\epsilon_{xy}^{-1}(\boldsymbol{r}) = \left(\epsilon_{yx}^{-1}(\boldsymbol{r})\right)^* = i \sum_{\boldsymbol{G}} \epsilon'_{\boldsymbol{G}} e^{i \boldsymbol{G} \cdot \boldsymbol{r}} \tag{A.6}$$

Again, we set this Fourier component to a constant ϵ_2^{-1}. Repeating the same degenerate perturbation theory analysis above, we can show, after a little bit of algebra, that the effect of the Faraday coupling is to add an imaginary antisymmetric matrix B, where

$$B = i\epsilon_2^{-1} \begin{pmatrix} 0 & \boldsymbol{k}_1 \times \boldsymbol{k}_2 & \boldsymbol{k}_1 \times \boldsymbol{k}_3 \\ \boldsymbol{k}_2 \times \boldsymbol{k}_1 & 0 & \boldsymbol{k}_2 \times \boldsymbol{k}_3 \\ \boldsymbol{k}_3 \times \boldsymbol{k}_1 & \boldsymbol{k}_3 \times \boldsymbol{k}_2 & 0 \end{pmatrix} \tag{A.7}$$

Again, this term does not affect the non-degenerate mode which we ignore from this point onwards. Exactly at the zone corners, the extra term above opens up the gap at the Dirac point. The spectrum is

$$\omega = \omega_D \pm v_D \left(|\delta \boldsymbol{k}|^2 + \kappa^2 \right)^{1/2}, \tag{A.8}$$

with

$$\kappa = \frac{3}{2} \epsilon_0 \epsilon_2^{-1} |\boldsymbol{K}| \tag{A.9}$$

Putting it all together, we can derive the spinorial form of the Hamiltonian near the Dirac points. We use the states in Eq. 3.82. We write them as

$$u(\boldsymbol{r}) = (1, \eta^*, \eta) \tag{A.10}$$

$$v(\boldsymbol{r}) = (1, \eta, \eta^*), \tag{A.11}$$

where $\eta = \exp(2\pi i/3)$. These states refer to the scalar H_z fields, and the notation . We will not need the electric fields here. The effective Hamiltonian that governs the mixing of the states at finte $\delta \boldsymbol{k}$ will be obtained from

$$\mathcal{H}_{eff}(\delta \boldsymbol{k}) = \begin{pmatrix} u^\dagger (A+B) u & u^\dagger (A+B) v \\ v^\dagger (A+B) u & v^\dagger (A+B) v \end{pmatrix} \tag{A.12}$$

The strategy is to work out the A,B matrices, and the states u and v to leading order in $\delta \boldsymbol{k}$, using the definition

$$\mathcal{H}_{eff} \begin{pmatrix} u \\ v \end{pmatrix} = (\omega(\delta \boldsymbol{k}) - \omega_D) \begin{pmatrix} u \\ v \end{pmatrix}. \tag{A.13}$$

A detailed calculation shows that indeed,

$$\mathcal{H}_{eff}(\delta \boldsymbol{k}) = v_D \left(\delta k_x \sigma^x + \delta k_y \sigma^y \right) + \kappa \sigma^z, \tag{A.14}$$

which is the main result of this analysis.

Appendix B

Appendix to Chapter 5

B.1 Mapping the frustrated XY model onto a one-component Coulomb plasma

In this appendix, we map the XY model in the Villan representation onto the one component plasma with a static background charge density.

We start from the 2D XY model in an external magnetic field ("frustrated XY model"):

$$\mathcal{H} = -J \sum_{<ij>} \cos\left(\theta_j - \theta_i - A_{ij}\right), \tag{B.1}$$

where $A_{ij} = \int_{r_i}^{r_j} \boldsymbol{A} \cdot d\boldsymbol{r}$, and $\nabla \times \boldsymbol{A} = 2\pi b$. "Villainize" the action to get

$$Z_V = \int D\theta \prod_{<ij>} \sum_{l_{ij}=-\infty}^{\infty} e^{-{l_{ij}}^2/2\beta J} e^{i l_{ij}(\theta_j - \theta_i - A_{ij})}. \tag{B.2}$$

Tracing over the angles, we get the constraint that the link variables l_{ij} must be divergence-free, which in turn lets us express them as a curl of a scalar "height" field

$$l_x = \nabla^y h$$

$$l_y = -\nabla^x h,$$

which enables us to map the Villain model on to the "solid on solid" model

$$Z_{S.O.S} = \prod_r \sum_{h(r)=-\infty}^{\infty} e^{-\frac{1}{2\beta J}|\nabla h|^2} e^{-i\left(\vec{A}\times\nabla h\right)\cdot\hat{z}} \tag{B.3}$$

Here, the scalar field h is defined on the dual lattice sites. Next, apply the Poisson summation formula

$$\sum_{n=-\infty}^{\infty} S_n = \sum_{m=-\infty}^{\infty} \int_{-\infty}^{\infty} dx S(x) e^{-2\pi i m x} \tag{B.4}$$

to map the "height fields" in S.O.S to the spin wave field of 2D coulomb gas (the integer fields m above then are interpreted as integer vortex variables):

$$Z = \prod_r \sum_{m(r)} \int_{-\infty}^{\infty} d\phi(r) e^{-\frac{1}{2\beta J}|\nabla\phi|^2} e^{-i\left(\vec{A}\times\nabla\phi\right)\cdot\hat{z}} e^{-2\pi i m(r)\phi(r)} \tag{B.5}$$

Before integrating out the spin waves, we rearrange the term involving the gauge fields A as follows. Imagine taking a continuum limit of the lattice partition function above. The products over sites becomes a functional integral of the Action

$$\int d^2r \left(-\frac{1}{2\beta J} \vec{\nabla}\phi \cdot \vec{\nabla}\phi - i\hat{z}\left(\vec{A}\times\vec{\nabla}\phi\right) - 2\pi i m(r)\phi(r) \right) \tag{B.6}$$

Written this way, we may integrate the second (and first) term by parts and obtain the following gauge-invariant action involving b:

$$\int d^2r \left(-\frac{1}{2\beta J} \phi(r)\nabla^2\phi(r) + 2\pi i \phi(r)\left(b - m(r)\right) \right) \tag{B.7}$$

Finally, after reverting back to the lattice and doing the gaussian integral over the spin wave fields $\phi(x)$, we arrive at the coulomb gas representation of the frustrated 2D XY model:

$$Z_{CG} = Z_{SW} \sum_m \prod_{r,r'} e^{-2\pi^2\beta J(m(r)-b)V(r,r')(m(r')-b)} \tag{B.8}$$

Thus, the magnetic flux per plaquette in the starting XY model translates to a static background charge density.

References

[1] Aharonov, Y., and Bohm, D. *Phys. Rev.* ***115*** (1959), 485.

[2] Aji, V., and Goldenfeld, N. *Phys. Rev. Lett.* ***87*** (2001), 197003.

[3] Ambegaokar, V., Halperin, B., Nelson, D., and Siggia, E. *Phys. Rev. B* ***21*** (1980), 1806.

[4] Anderson, P. *Cond-mat/0603726*.

[5] Batrouni, G., Katz, G., Kronfeld, A., Lepage, G., Svetitsky, B., and Wilson, K. *Phys. Rev. D* ***32*** (1985), 2736.

[6] Berry, M. *Proc. Roy. Soc. London A* ***392*** (1984), 45.

[7] Booth, R. C., and White, E. A. D. *J. Phys. D: Appl. Phys.* ***17*** (1984), 579–587.

[8] Cardy, J. *Scaling and Renormalization in Statistical Physics*.

[9] Chaikin, P. M., and Lubensky, T. L. *Principles of Condensed Matter Physics*.

[10] Chang, M. C., and Niu, Q. *Phys. Rev. B* ***53*** (1996), 7010.

[11] Cooper, N., Halperin, B., and Ruzin, I. *Phys. Rev. B* ***55*** (1997), 2344.

[12] Corson, J., Mallozzi, R., Orenstein, J., Eckstein, J., and Bozovic, I. *Nature* ***398*** (1999), 221.

[13] Dasgupta, C., and Halperin, B. I. *Phys. Rev. Lett.* ***47*** (1981), 1556.

[14] Delfini, L., Lepri, S., and Livi, R. *J. Stat. Mech.* (2005), P05006.

[15] Emery, V. J., and Kivelson, S. A. *Nature* ***374*** (1995), 434.

[16] Fisher, D. *Phys. Rev. B* ***22*** (1980), 1190.

[17] Fisher, D., Fisher, M., and Huse, D. *Phys. Rev. B* ***43*** (1991), 130.

[18] Fisher, M., Barber, M., and Jasnow, D. *Phys. Rev. A.* ***8*** (1973), 1111.

[19] Haldane, F. D. M. *Phys. Rev. Lett.* ***61*** (1988), 2015.

[20] Haldane, F. D. M., and Raghu, S. *Cond-mat/0503588*.

[21] Hofstadter, D. R. *Phys. Rev. B* ***14*** (1976), 2239.

[22] Hohenberg, P. C., and Halperin, B. I. *Rev. Mod. Phys.* ***49*** (1977), 435.

[23] Jensen, L., Kim, B., and Minnhagen, P. *Phys. Rev. B* ***61*** (2000), 15412.

[24] Joannopoulos, J. D., Meade, R. D., and Winn, J. N. *Photonic Crystals: Molding the Flow of Light.* Princeton University Press, 1995.

[25] Kane, C., and Mele, E. *Phys. Rev. Lett.* ***95*** (2005), 146802.

[26] Kane, C. L., and Mele, E. J. *Phys. Rev. Lett.* ***95*** (2005), 226801.

[27] Karplus, R., and Luttinger, J. M. *Phys. Rev.* ***95*** (1954), 1154.

[28] Kohmoto, M. *Ann. Phys. (NY)* ***160*** (1985), 343.

[29] Kosterlitz, J. M., and Thouless, D. J. *J.Phys.C* ***6*** (1973), 1181.

[30] Landau, L. D., and Lifshitz, L. P. *Quantum Mechanics: Non-Relativistic Theory.*

[31] Laughlin, R. B. *Phys. Rev. Lett.* ***50*** (1983), 1395.

[32] Lee, W.-L., Watauchi, S., Miller, V. L., Cava, R. J., and Ong, N. *Science* ***303*** (2004), 1647.

[33] Levrel, L., and Maggs, A. C. *Phys. Rev. E* ***72*** (2005), 016715.

[34] Li, L., Wang, Y., Naughton, M., Ono, S., Ando, Y., and Ong, N. *Europhys. Lett.* ***72*** (2005), 451.

[35] Lidmar, J., and Wallin, M. *Phys. Rev. B* ***59*** (1999), 8451.

[36] Lin, S.-Y., Chow, E., Hietala, V., and Villeneuve, P. R. *Science* ***282*** (1998), 274.

[37] Maggs, A., and Rossetto, V. *Phys. Rev. Lett.* ***88*** (2002), 196402.

[38] Man, W., Megens, M., Steinhardt, P. J., and Chaikin, P. *Nature* ***436*** (2005), 993.

[39] Marques, R., Martel, J., Mesa, F., and Medina, F. *Phys. Rev. Lett.* ***89*** (2002), 183901.

[40] Martin, P., Siggia, E., and Rose, H. *Phys. Rev. A* ***8*** (1973), 423.

[41] Meade, R., Brommer, K., Rappe, A., and Joannopoulos, J. *Phys. Rev. B* ***48*** (1993), 8434.

[42] Mukerjee, S., and Huse, D. *Phys. Rev. B* ***70*** (2004), 014506.

[43] Nakahara, M. *Geometry, Topology, and Physics*. IOP Publishing, 1990.

[44] Nelson, D. R., and Kosterlitz, J. M. *Phys. Rev. Lett.* ***39*** (1977), 1201.

[45] Niu, Q., Thouless, D., and Wu, Y. *Phys. Rev. B* ***31*** (1985), 3372.

[46] Oji, H., and Streda, P. *Phys. Rev. B* ***31*** (1997), 7291.

[47] Olsson, P. *Phys. Rev. Lett.* ***75*** (1995), 2758.

[48] Onoda, M., Murakami, S., and Nagaosa, N. *Phys. Rev. Lett.* ***93*** (2004), 083901.

[49] Onoda, M., and Nagaosa, N. *Phys. Rev. Lett.* ***90*** (2003), 206601.

[50] Ota, S. *J. Phys. Condens. Matter* ***4***, 5411.

[51] Pendry, J., and MacKinnon, A. *Phys. Rev. Lett.* ***69*** (1992), 2772.

[52] Plihal, M., and Maradudin, A. A. *Phys. Rev. B* ***44*** (1991), 8565.

[53] Simon, B. *Phys. Rev. Lett.* ***51*** (1983), 2167.

[54] Sondheimer, E. H. *Proc. Roy. Soc. Lond. A Mat.* ***193*** (1948), 484.

[55] Středa, P. *J. Phys. C* ***15*** (1982), L717.

[56] Sundaram, and Niu, Q. *Phys. Rev. B*.

[57] Teitel, S., and Jayaprakash, C. *Phys. Rev. B* ***27*** (1983), 598.

[58] Thouless, D. *Topological Quantum Numbers in Nonrelativistic Physics*. World Scientific, 1998.

[59] Thouless, D., Kohmoto, M., Nightingale, M., and den Nijs, M. *Phys. Rev. Lett.* ***49*** (1982), 405.

[60] Ullah, S., and Dorsey, A. *Phys. Rev. B* ***44*** (1991), 262.

[61] Ussishkin, I., Sondhi, S., and Huse, D. *Phys. Rev. Lett.* ***89*** (2002), 287001.

[62] Villain, J. *J.Phys. (Paris)* ***36*** (1975), 581.

[63] von Klitzing, K., Dorda, G., and Pepper, M. *Phys. Rev. Lett.* ***45*** (1980), 494.

[64] Wang, Y., Li, L., Naughton, M., Gu, G., Uchida, S., and Ong, N. *Phys. Rev. Lett.* ***95*** (2005), 247002.

[65] Wang, Y., Ong, N., Xu, Z., Kakeshita, T., Uchida, S., Bonn, D., Liang, R., and Hardy, W. *Phys. Rev. Lett.* ***88*** (2002), 257003.

[66] Wang, Y., Ono, S., Onose, Y., Gu, G., Ando, Y., Tokura, Y., Uchida, S., and Ong, N. *Science* ***299*** (2003), 86.

[67] Wang, Y., Xu, Z., Kakeshita, T., Uchida, S., Ono, S., Ando, Y., and Ong, N. *Phys. Rev. B* ***64*** (2001), 224519.

[68] Weber, H., and Minnhagen, P. *Phys. Rev. B* ***37*** (1988), 5986.

[69] Xu, Z. A., Ong, N., Wang, Y., Takeshita, T., and Uchida, S. *Nature* ***406*** (2000), 486.

[70] Zinn-Justin, J. *Quantum Field Theory and Critical Phenomena*. Oxford Scientific Publications, 1996.